UFES

FEDERAL UNIVERSITY OF ESPIRITO SANTO

Technological Center

Post-Graduate Program in Electrical Engineering

Master's Dissertation

Simulating a Multi-Vehicle Traffic Sensing System Based on Radio Tomographic Imaging

Jarmo Theodore Wilkens

Vitória

2016

FEDERAL UNIVERSITY OF ESPIRITO SANTO

Master's Dissertation

Simulating a Multi-Vehicle Traffic Sensing System Based on Radio Tomographic Imaging

Author:
Jarmo T. Wilkens

Advisors:
Dr. Anilton S. Garcia
Dr. Jair A. L. Silva

Dissertation submitted in partial fulfillment of the requirements for the degree of

MASTER OF SCIENCE (M.Sc.)

in

TELECOMMUNICATIONS

Post-Graduate Program in Electrical Engineering

March 2016

Acknowledgments

First and foremost, I would like to offer my special thanks to my coordinator, Prof. Anilton Salles Garcia, for accepting my research proposal and coordinating me on the development of my dissertation.

I would also like to acknowledge the support provided by Prof. Jair Adriano Lima Silva, who advised me on the development of the simulation model.

Furthermore, I would like to thank my colleagues from LabTel (Laboratory of Telecommunications), especially Rodrigo Stange Tessinari and Marcia Helena Moreira Paiva, for giving me new insights and advice that were useful for the development of this dissertation.

Additionally, I would like to thank the Post-Graduate Program of Electrical Engineering of UFES for offering me the opportunity to study the Master's program of Telecommunications and offering me a motivating working space in LabTel.

Also, my grateful thanks go to FAPES who made it possible for me to study the Master's program by supporting me financially throughout the two-year period.

Last but not least, in no specific order, I would like to express my thanks to my friends, especially Wouter Langenkamp, and family, for supporting me throughout my Master's project.

Jarmo Theodore Wilkens

Abstract

With the increasing amount of vehicles on the road, traffic jams pose a growing global problem. Traffic surveillance is a crucial task into improving traffic flow. The core of this dissertation proposes a design and methodology for the real-time estimation of occupancy and velocity of one or two vehicles on a single lane road segment, traveling at speeds from 10 km/h up to 50 km/h, using a Radio Tomographic Imaging (RTI) network. RTI is an emerging technology and consists of a wireless sensor network that produces images of the change in the electromagnetic field of a monitored area using Received Signal Strength (RSS) measurements. This allows the tracking of device-free objects such as humans and cars. The proposal is the first to present an RTI network that is split into multiple sub-networks to achieve a network scan frequency fast enough to prevent blurring in the captured images of vehicles traveling at velocities higher than 50 km/h. This proposal suggests three newly implemented techniques, namely a new weight matrix calculation method, a new node spacing setup and a new vehicle detection method. The main contribution of this dissertation is to stimulate research of the possibility of using RTI networks as being part of an Intelligent Transport System (ITS) in a smart city environment. This dissertation also presents a new, relatively complete simulation model that simulates the proposed RTI system. It generates RSS measurements based on the IEEE 802.15.4 protocol for ZigBee communication, which are processed using RTI techniques commonly used in literature. The simulation model allows the specification of an RTI network from the ground up, including node positions, network size and geometry and RSS measurement processing using any available or newly developed techniques. The simulation results, obtained after implementing the proposed RTI system to the validated simulation model, indicate that it is possible to detect both one or two family sized cars simultaneously. Using techniques that reduce RSS variance due to multipath effects and the newly proposed methods, simulated vehicle detection performance is demonstrated to be between 95% and 100%.

Resumo

O aumento da quantidade de veículos nas estradas faz com que engarrafamentos representam um problema global crescente. Monitoramento do tráfego é tarefa crucial para o melhoramento do fluxo de tráfego. O foco desta dissertação de Mestrado está na proposta e no desenvolvimento de uma metodologia para a estimativa em tempo real de ocupação e velocidade de um ou dois veículos em um único segmento de pista, trafegando à velocidades que variam entre 10 km/h e 50 km/h, usando uma rede de tomografia de rádio por imagem RTI (*Radio Tomographic Imaging*). RTI é uma tecnologia emergente e consiste de uma rede de sensores sem fio que produz imagens da mudança no campo eletromagnético de uma área monitorada usando potência do sinal recebido RSS (*Received Signal Strength*). Isso permite o rastreamento de objetos tais como pessoas e carros que não contêm dispositivos de transcepção. A proposta é a primeira a apresentar uma rede RTI que é dividida em várias sub-redes para alcançar uma frequência de varredura de rede suficientemente rápida para evitar a desfocagem nas imagens capturadas por veículos que andam a velocidades acima dos 50 km/h. Sugere-se nesta proposta um novo método de cálculo da matriz de peso, uma nova configuração de espaçamento de nó e um novo método de detecção de veículos. A principal contribuição deste trabalho é estimular a pesquisa sobre a possibilidade de usar redes RTI como sendo parte de um sistema de transporte inteligente em um ambiente de cidades inteligentes. Esta dissertação apresenta também um novo modelo de simulação relativamente completo para o sistema RTI proposto. Este modelo gera medições RSS baseado no protocolo IEEE 802.15.4 para a comunicação ZigBee, que são processadas utilizando técnicas RTI comumente utilizadas na literatura. O modelo permite a especificação de uma rede RTI a partir do zero, incluindo posições de nó, tamanho e geometria da rede, sendo que o processamento de medição de RSS pode utilizar qualquer técnica desenvolvida. Os resultados das simulações, obtidos pós a aplicação do sistema RTI proposto para o modelo de simulação validado, indicam que é possível detectar um ou dois carros populares simultaneamente. Usando técnicas que reduzem a variância do RSS devido aos efeitos múltiplos percursos, o desempenho da detecção de veículos apresentou acurácia entre 95% e 100%.

Contents

List of Figures

List of Tables

List of abbreviations and acronyms

ITS *Intelligent Transport System* - a system that gathers and communicates road traffic information to various users with the goal to improve road safety and enable more coordinated and smarter use of the transport infrastructure.

RSS *Received Signal Strength* - signal power in dBm measured at the antenna of the receiver radio.

RTI *Radio Tomographic Imaging* - wireless communication technology that produces an image of the electromagnetic field of the measured area.

VANET *Vehicular Ad-Hoc Network* - a network that connects transceiver-equipped vehicles, which share data including location and speed information with each other when they are in range.

Voxel Volume of a 3-dimensional area in space represented by a pixel.

ZigBee Wireless communication protocol used for personal area networks with small, low-power transceivers. ZigBee is based on the IEEE 802.15.4 standard.

1 Introduction

In recent years, ubiquity of wireless technology has grown rapidly. One of the latest wireless technologies is Radio Tomographic Imaging (RTI). Radio Tomographic Imaging is a technology initially developed in 2008 by Patwari et al. [5], which generates an image that represents the electromagnetic field of a monitored area. The technology aims to localize and track stationary or moving device-free targets. RTI relies on a mesh network of simple and inexpensive stationary radio transceivers that are deployed on the border of the area of interest, where each radio is wirelessly connected in the 2.4 GHz Industrial, Scientific and Medical (ISM) band to all other radios. Radio signals pass through or diffract around objects present inside the Wireless Sensor Network (WSN), also known as shadowing [6]. By knowing the position of the radios and by obtaining the Received Signal Strength (RSS) of every link inside the network, the RTI system is able to image the location of a target in real-time due to signal shadowing.

The technology is analogous to Computed Tomography (CT) scans, in the sense that multiple narrow radio beams from different positions are directed through an area of interest, each producing a slice of the area [7]. In CT, however, each slice produces an image, whereas in RTI, all the combined slices generates one single image.

Figure 1 provides a top-view impression of an RTI network initially presented by Wilson et al. [1]. Recent papers have applied new techniques that led to improved RTI performance [8, 9, 10, 11].

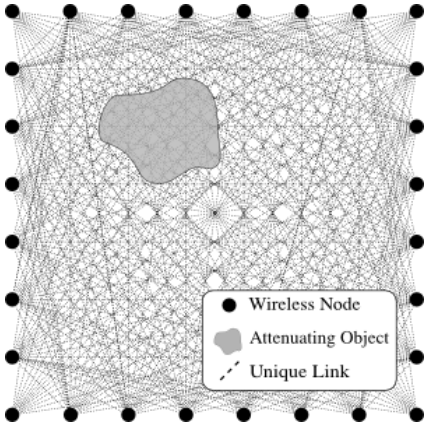

Figure 1 – RTI network in a square geometry with 28 nodes [1]

With such a novel and promising technology, a wide range of opportunities and applications yet to be discovered emerge. Wilson et al. [12] name a few of such applications:

- Track people and vehicles in next-generation security systems
- Locate victims in fire and rescue operations
- Locate and count people in the rooms of “smart homes”
- Measure accurate usage statistics in buildings and stores
- Automate control of other devices

Applying the RTI technology to a traffic environment is another possible application, which would open gates to yet another wide field of possibilities. Subsection 1.2.2 describes more possible applications.

1.1 Problem Contextualization

This section presents the current problem of global vehicle traffic and a possible solution to reduce this problem, which is the basis of this dissertation.

1.1.1 Vehicle traffic problem

Currently, inefficient vehicle traffic like traffic jams pose a global problem. They limit a city's efficiency and growth, as people waste time by waiting and may arrive late at work or meetings. Furthermore, it is difficult for emergency services to pass and costly for industries as transportation time and fuel consumption increases. Moreover, traffic jams pose a negative impact on air pollution. It is therefore essential for a city's efficiency to keep optimal traffic flow.

1.1.2 Solution

One way to solve the described problem is to measure vehicle occupancy and traffic flow along roads. These statistics may be made available online or directly relayed to navigation systems to inform people about traffic conditions and suggest a faster or alternative route. People may also decide to take public transport instead or wait to travel later if they are not in a hurry. Furthermore, traffic data can be used to more efficiently control traffic lights.

The proposed RTI system is intended to measure vehicle occupancy and traffic flow by deploying the sensors on the roadsides. The system would act as a smart city roadside surveillance application that could be integrated into an Intelligent Transport System (ITS).

1.2 Research Motivation

Even though there already exists vehicle surveillance technology implemented in traffic situations for traffic parameter sampling, the motivation of researching an RTI application is its cost-effectiveness, scalability and easily-configurable network. This section describes the state-of-the-art vehicle surveillance technology and possible radio tomographic imaging applications that stimulate the motivation of researching about RTI technology.

1.2.1 State-of-the-art vehicle traffic surveillance technology

Vehicle traffic surveillance technology currently implemented consists of ground-based systems including cameras, radars, lasers, induction loops and Vehicular Ad Hoc Networks (VANETs), and airborne platforms. The information gathered by some of these road sensors is currently used by software from companies such as Microsoft, who developed Bing Maps, which fairly accurately visualizes traffic conditions [13]. Google Maps, instead of using road sensors, takes cellular data from Android phones to determine vehicle traffic [14].

Induction loops embedded in the road surface are used to control traffic lights depending on traffic density to increase traffic flow. Several induction loops may be integrated on the same road to count vehicles and calculate vehicle velocity. This technology, however, carries relatively high costs due to adjusting the road's surface and implementation of a (wired) communications infrastructure. Also, coverage area is small [15].

Cameras are commonly positioned on top of a road. Additional to counting vehicles and calculating velocity, their advantage is that they can recognize each car by their license plate and have a relatively large coverage area. In situations where only vehicle count and velocity is required, however, complex camera applications would be redundant and costly due to implementation of a (wired) communications infrastructure and the cost of the camera itself. Also, foggy weather conditions could diminish performance (fusion with IR camera solves this problem, but increases costs further).

Radars and lasers [16] are usually positioned beside or on top of a road. They are also able to count vehicles and calculate velocity and in combination with a camera recognize license plates, but they cover a smaller area than cameras mounted on top of a road, only detect vehicles on one lane and they are also relatively expensive to implement.

An airborne traffic surveillance platform was proposed by Luo et al. [17] in 2011, with the advantage of flexibility, convenience and low cost relative to ground-based systems. The Unmanned Aerial Vehicle (UAV) carries a camera on-board for vehicle detection. The limitations of such system are that it requires periodic recharging or refueling and therefore has periodic down-time, is affected by extreme weather conditions, has a risk of crashing into the vehicles and can be distracting for drivers.

Vehicular Ad Hoc Networks (VANETs) are networks that connect transceiver-equipped vehicles, which share data including location and speed information with each other when they are in range. When vehicles are in range of a ground-based base-station, the gathered information is passed to a central server that processes the data to obtain metadata, such as traffic condition estimates [18]. The advantage of using VANETs is its relatively low cost as the system is expanded, since only a limited number of base-stations need to be installed while the cost of adding an extra vehicle node to the network is relatively low. The limitation is that the sensors are mobile and uncontrollable if VANETs are to be used by the public, meaning it is not possible to obtain accurate traffic condition information at one particular location at a specific point in time when necessary.

One of the possible solutions to improving traffic flow, so not just measuring traffic flow, is autonomous vehicles. These vehicles do not require a driver and are completely controlled by computer systems. The computer systems consist of communication between sensors and artificial intelligence software that measure and understand the vehicle's environment. Traffic flow may be improved by the sharing of location and speed data between autonomous vehicles, making it possible for the computer systems to calculate an optimal velocity that favors efficient traffic flow. Such technology, however, is a more long-term solution.

1.2.2 Possible Radio Tomographic Imaging applications

The possible applications arising from Radio Tomographic Imaging technology consist of locating and tracking people and vehicles. They are broken down into sub-applications, which describe the integration with a security system, safety system, commercial environment and home automation.

Locating and tracking of people

RTI technology may be applied to locate and track people in security and safety systems, or it may be used in commercial environments and home automation.
As a security system:

- An already existing commercially available Tomographic Motion Detection system provided by Xandem that is based on RTI technology serves as a security system that senses motion through walls, furniture

and obstructions. The radios are hidden behind the walls and in combination with an RF jamming detection system, it makes it a powerful unbeatable security system [19].

- Using RTI technology, people can be tracked and identified by their gait. By monitoring gait, suspicious behavior in public environments such as shops, banks or airports may be flagged and consequently activate the security system. In hospitals, they may be used to detect patients leaving a particular room while they are restricted to do so.

As a safety system:

- In a factory environment, workers that carry dangerous loads may be alerted by monitoring their gait.
- Though not yet researched, a 3D RTI system that may be envisioned as having multiple layers of nodes stacked on top of each other may be able to detect body movements in 3D. A RTI network operating in the 2.4 GHz frequency band, however, would be unsatisfactory, as this generates a resolution equal to the wavelength of 12.5 cm. A network operating in the 5 GHz band would be more appropriate. Caretakers could be alerted if children or elderly people fell down or leave particular environments.
- Localization of firemen or military by deploying an RTI network around a building, as proposed by Maas et al. [11].

In commercial environments:

- Intelligent retail system that monitors people traffic in or outside a store to determine the interest in particular products. This allows the store to gain costumer intelligence, which could be used to for example give promotions to returning customers.

In home automation:

- Locate people to control electrical appliances accordingly, including lights and air-conditioners.
- A RTI system deployed at the entrance of a building could identify a person by his or her gait and consequently lock or unlock doors. This has recently been demonstrated in a product video made by Xandem [19].
- Though not yet researched, a 3D RTI system might be used to identify pre-programmed body movements (gesture control) in home automation to control appliances. A list of appliances may include TV, computer, air-conditioner, temperature, light brightness, audio system volume, and so on.

Locating and tracking of vehicles

Vehicles may be located and tracked in a public (smart city) or private environment.
Public (smart city) environment:

- Measure vehicle occupancy and traffic flow on public roads with radios deployed on the roadside that form an RTI network.
- In a 3D RTI system, simple features describing a vehicle's class may be identified, including vehicle height, length and shape as was similarly being investigated by [20]. The quality of the feature identification would depend on the spatial resolution, where a higher number of radios in a larger amount of

layers would increase resolution. Such application may be used as a low-cost solution to remotely monitor a roadway at locations such as border crossings, and be combined with other sensors like cameras to obtain higher quality measurements.

Private environment:

- In a parking facility, vehicles may be located to give location-based directions to a nearby available parking space or to guide them to the exit.

Traffic flow monitoring possibilities

This subsection covers the possible uses of the vehicle traffic density and flow information generated from the RTI system proposed in this dissertation. These uses stimulate the motivation for researching the application of the proposed roadside surveillance RTI system.
Vehicle traffic data may be used to:

- Control traffic lights more efficiently.
- Detect traffic jams.
- Aid navigation systems that may use the information to suggest a faster or alternative route for emergency responders or regular people.
- Provide real-time data online to inform people about current traffic conditions. People may decide to take public transport instead or simply wait to travel later if they are not in a hurry.
- Identify and replay accidents or detect unlawful behavior of vehicles given that sensing area is sufficiently large.
- Be integrated into a Parking Management System (PMS) for parking guidance.
- Predict traffic behavior using Artificial Intelligence algorithms.

1.3 Justification of Chosen Theme

The advantage of the proposed roadside surveillance implementation using RTI technology over the already implemented technologies is an expected reduction in cost, its scalability, easily-configurable network and its possible secondary uses.

The radios communicate wirelessly to a base station, meaning infrastructural costs are relatively low compared to the wired communication infrastructure of induction loops, cameras, radars and lasers. Also, the radios themselves are relatively simple and low cost devices, so it is more attractive to consider system expansion as compared to a camera system. The infrastructural costs of conventional systems usually prevents the implementation of dense coverage areas [15].

Moreover, to increase sensing area or spatial resolution, the RTI network could relatively easy (compared to cameras, radars and induction loops) be expanded by adding wireless nodes that can easily be configured to the already existing mesh-network. Expanding the RTI network would generate additional traffic information and improve estimate accuracy [15], which would be interesting to, for example, identify or replay accidents or detect "odd" behaviour of cars. As Papageorgiou et al. [21] discuss, the sampling density (or spatial resolution) of conventional systems, which in best cases is every 0.5 - 1 km, is not sufficient for congestion

control and safety improvement in urban areas. The RTI network could be easily configured to have a sufficiently high sampling density.

The RTI system may be envisioned to work individually to generate traffic statistics or complementary to the aforementioned systems to provide additional or more reliable traffic statistics, to be used in traffic estimation algorithms like Clearflow of Bing Maps [13]. As a possible secondary use, the sensors may be configured to act as base stations for communication with VANETs. Furthermore, vehicles may be identified according to their size by using the reflected signals from the vehicles, similar to how radar works. The transmitters would need to be configured to be able to receive too. This may make it possible to distinguish between trucks, family cars or motorcycles, similar to what was researched by Anderson et al. [20]. Knowing the location of the vehicles, the RTI system will also be able to determine the distance between them to generate additional traffic statistics.

To summarize, using an RTI network deployed on road segments for traffic parameter sampling in an Intelligent Transport System (ITS) system seems to offer a wide scale of applications and solutions to existing problems, making it interesting to carry out research into its possibilities.

1.4 Proposal/Goal

A practical methodology will be proposed that estimates occupancy and velocity of two vehicles on a single lane road segment with radios deployed on the roadside that form an RTI network. Figure 2 provides a top view impression of the proposal, where the blue rectangles represent vehicles.

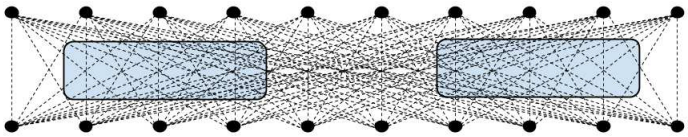

Figure 2 – Top view impression of project proposal. The black dots represent the radios, the dashed lines are the communication links between the radios and the blue rectangles represent vehicles.

The proposed RTI system should be able to measure occupancy of and velocity of multiple vehicles real-time, fast enough to track vehicles moving at 50 km/h. Moreover, the RTI system should be robust against RSS link variance and RSS time-variance. RSS link variance is caused by multipath effects, while RSS time-variance is dependent on changes in the environment that are non-related to the target, such as random objects being placed in the area or weather effects, such as wind that sways leaves, branches or the nodes themselves.

1.5 General Objectives

This section outlines the general (intangible) objectives.

- Propose the research, with focus on a conceptual and methodological approach, of the possible applications of Radio Tomographic Imaging, with a particular emphasis concerning a traffic environment as a smart city application.
- Make students and professors aware and bring knowledge about Radio Tomographic Imaging to LabTel.
- Provide incentives to continue the research on RTI for future master or PhD projects within LabTel.

1.6 Specific Objectives

Objectives that can be measured/verified are mentioned in this section.

- Demonstrate data acquisition, processing procedures and expected performance results using a newly proposed simulation model in MATLAB.
- Validate simulation model performance by comparing simulated to real RTI data that is published online in the same network configuration.
- A practical implementation is outside the scope of this thesis.

1.7 Research Methodology

In order to be able to achieve the research goal, the specific objectives must be met.

The most important method employed to meet the objectives was to fully understand the main principles behind Radio Tomographic Imaging, by studying the first papers about the technology that describe its theoretical fundamentals. A summary was made of one of the main articles, which was regularly consulted when studying more recent papers with new developments. All procedures from data acquisition to obtain the RTI image using different recent methods were studied.

Three articles were chosen to be evaluated, which were based on their diversity from each other and the potential of their proposed methods to be used to develop a new algorithm for this project. Once an algorithm and network setup configurations were proposed, a methodology to realize tests for vehicle traffic measurements was presented.

Raw RTI (experimental) data published online by Wilson et al. [1] was used together with RSS behavior described in literature to develop a new simulation model in MATLAB. Parameters for the path-loss model were calculated from the experimental data, which were used to generate path gains required for the simulation. To validate the simulation model, the RSS probability distribution from the tests carried out by Wilson et al. and the simulated measurements were compared. After validation, the simulation model was used to present expected performance of the data gathered from the proposed RTI set-up.

1.8 Main Results and Contributions

The main results and contributions covered in this dissertation are listed below:

- A new RTI system that meets the requirements described in the goal. This proposal includes a new voxel-specific threshold approach for the detection and localization of vehicles.
- Present a new validated simulation model that simulates the proposed RTI network and generates performance statistics
- A new weight matrix calculation method
- A new network node spacing setup

Another contribution of this dissertation is to stimulate research of the possibility of using RTI networks as being part of an Intelligent Transport System in a smart city environment.

1.9 Structure of Document

The rest of this document is organized as follows. Chapter 2 details the related work of RTI, RF-based roadside surveillance and RTI simulations. In chapter 3, the theory behind the Radio Tomographic Imaging model is explained together with various recently proposed techniques and network configurations. It also covers the analysis of three recent articles, of which some features are combined into one newly proposed RTI system as described in chapter 4. The newly presented simulation model complete with validation is outlined in chapter 5, which is used to simulate the proposed RTI system, as shown in the results in chapter 6. The conclusion of chapters 4 - 6 is presented in chapter 7, which also contains future work to be done.

2 Related Work

Radio Tomographic Imaging is a relatively new technology (2008) and relatively little research has been carried out in the area. The most recent and most relevant related work published concerning RTI and RF-based roadside surveillance is outlined in section 2.1 and 2.2 respectively. Section 2.3 presents RTI research that was carried out using simulations and the limitations of the described related work that will be treated and limitations that will not be treated are explained in section 2.4.

2.1 Related work about RTI

Zhao et al. [22] developed a Kernel (histogram-based) RTI network that tracks stationary and moving people real-time in both Line-of-Sight (LOS) and non-LOS environments. Location estimates are based on short and long term histograms of the single-channel RSS data on every link, where the long-term histogram can be seen as online calibration. This implementation shows a significant improvement over earlier variance-based systems that are only able to track moving people, not stationary people, as it is based on the variance of RSS data. The researchers achieve a distance precision in four different environments with twenty measured locations each a Root-Mean-Square-Error (RMSE) between 0.73 m and 0.81 m. However, they mention they did not optimize their parameters in each experiment on purpose to show the system's performance in different environments.

Bocca et al. [3] developed an attenuation-based RTI system intended for Ambient Assisted Living, which is able to localize stationary and moving people real-time in an indoor domestic environment. It is based on attenuation, meaning the location estimates depend on the difference between the current and average (reference) RSS measured during the system calibration. The system solves the online calibration problem by applying a novel spatial filter, which only calibrates RF links that are not attenuated by stationary people. Online calibration makes the system robust to environmental changes, such as extra or displaced furniture. In addition, they reduce multipath interference and improve location estimates significantly by combining RSS fade level data on multiple channels instead of using a single channel, but consequently increases computational cost. The results show that the researchers achieve an average location error of 0.23 m measured from 14 locations in a typical 58 m^2 single floor apartment with furniture. Their work was based on their previous research on RTI and channel diversity from 2012 [23], where in one of the experiments Bocca et al. set up an open environment to gather location estimates at ten positions and achieved an error of 0.10 m. They selected channels based on fade level to yield the highest accuracy.

Kaltiokallio et al. [10] developed an attenuation-based RTI system that localizes stationary and tracks moving people real-time. The authors reduce multipath interference and improve location estimates significantly by combining RSS fade level data on multiple channels. They also developed a model to determine link-channel specific parameters, thereby increasing localization accuracy further. An average tracking error of 0.17 m in an open environment was achieved, compared to 0.25 m in the same conditions for a similar state of the art system using channel diversity [23].

Alippi et al. [8] developed an outdoor RTI network method that detects and localizes multiple people real-time. Together with their proposed method, they combine several recent technologies with some adjustments, including measurements on multiple channels [10], spatial filtering for online calibration similar to [3], multi-target tracking [9] and background subtraction. They also develop an individual distance-RSS model for each

node, further increasing robustness. They compare their results to the previously described system [10] with an RTI network deployed in a forested area, where they achieve an average localization error of a stationary person of 3.2 m, as opposed to 4.1 m using the method of [10].

Wei et al. [24] examined the use of Electronically Switched Directional (ESD) antennas to improve RTI performance. ESD antennas focus radiated power in a selected direction to reduce multipath propagation and thereby reduce noise in links. Three methods were proposed to select the direction of each node, of which the fade level-based method yields highest performance. Compared to the multi-channel omni-directional RTI network in [23], their proposed system improves tracking performance by 42% in an open LOS-environment.

Adler et al. [25] proposed an RTI network, based on the method of Wilson et al. [1], which operates in the 800/900 MHz frequency band for improved energy efficiency purposes. In addition, they applied simple post-processed image filters to increase localization accuracy and used centroid methods to automatically detect the location of people in the produced images. In an open space measurement environment, they achieved a maximum error of under 0.78 m.

2.2 Related work about RF-based roadside surveillance

Kassem et al. [26] published an article titled "RF-based Vehicle Detection and Speed Estimation" that investigated the application of Device free Passive (DfP) localization, a technology similar to RTI, to detect and estimate vehicle presence and velocity. In DfP, only target location is extracted, while in RTI an image is produced that represents the electromagnetic field of the complete monitored area. The researchers set up a network of four radios at the sides of a single lane road (two equally spaced radios on each side) that produced four links. They show the feasibility of correctly differentiating between three states within the area covered by the four links: empty street, a stationary vehicle and moving vehicle. Statistical features including mean and variance of RSS data were integrated into a multi-class Support Vector Machine (SVM) for vehicle detection that showed a 100% accuracy, and a curve fitting approach was used to generate velocity estimates with a 90% accuracy. Kassem et al. [26] demonstrate that it is possible to detect vehicles within a WSN based on RSS measurements.

Anderson et al. published a paper titled "Radio Tomography for Roadside Surveillance"[20] that aimed to improve RTI modeling and algorithms in a roadside surveillance environment. Three improvements were proposed, which include an extra bias term to the existing image estimation solution [1], a way to remove negative observations and combining multiple frames to produce a more accurate final image. The latter improvement was used to generate velocity estimates. They compared their results to the first RTI network version by Wilson and Patwari [1], and show that their proposed approaches lead to greatly improved performance. The authors also set up a 3D RTI network operating on a single channel, where the z-component was established by placing radios on three heights spaced 0.5m, 1.0m and 1.5m from the ground. Anderson et al. have shown it is possible to track and recognize (using the 3rd dimension) a single vehicle passing through a single lane road and estimate its velocity using RTI.

2.3 Related work on simulating RTI networks

Simulating an RTI network has previously been proposed in the Master's dissertation of Cooke [27], who obtains reverse engineered RSS measurements using mathematical RTI models that consists of a simulated shadowing, path loss and noise vector. The shadowing vector depends on a semi-randomly generated image, which is based on a covariance matrix with a zero-mean Gaussian random vector. This method of simulating

RSS measurements is computationally efficient and is useful to test the effect of various parameters of different image regularization techniques (such as Tikhonov, truncated singular value decomposition and total variation). However, the simulated RSS data are dependent on two parameters required for the covariance matrix, which may cause a loss in how realistic the data is as these are not parameters that need to be set in a real-life measurement scenario.

A similar method has been applied by Milburn [28], who presented her approach in her Bachelor's dissertation. Milburn generated a high-resolution grayscale image that already contains obstacles, where the background and foreground (obstacles) are black and white respectively. Next, the author applied a blur filter and added some random Gaussian noise. RSS measurements for each link were obtained from applying the Bresenham's line algorithm to the previously generated grayscale image. Similarly, this approach is useful to evaluate image regularization techniques, but does not generate realistic RSS data due to the lack of implementation of wireless signal behavior.

2.4 Limitations to be treated

This section covers the limitations of the described related work to be overcome in this Master's project. It also describes which of the limitations will not be treated and instead left for future work to be done.

Kassem et al. [26] have shown that it is possible to detect vehicles within a WSN based on RSS data, but have only demonstrated this capability in a small network of four sensors. The WSN in this project uses more radio sensors over a longer road segment to not only detect, but also locate one or multiple vehicles over time simultaneously.

A limitation of the KRTI system of Zhao et al. [22] is that if a person is stationary for longer than the long term histogram period, the person would gradually disappear from the image. This is not desirable for a roadside surveillance application, as vehicles in a traffic jam may disappear from the image. The proposed RTI system uses online calibration to overcome this limitation.

The methods presented by Bocca et al. [3] and Kaltiokallio et al. [10] improve robustness against multipath interference significantly, but have not specifically designed their system to deal with time variance of RSS due to weather in outdoor environments. The proposed RTI system implements techniques to reduce time variance of RSS in outdoor conditions.

Anderson et al. [20] were able to detect, localize and identify vehicles in their RTI network, but did not publish quantitative results concerning localization accuracy and how it is affected by vehicle velocity, nor system performance for the tracking of multiple vehicles. This limitation is not treated in this dissertation, because a practical implementation is outside the scope of this project. However, expected quantitative results are presented using simulations only. Furthermore, the researchers made use of only one frequency channel, meaning negative effects of multipath interference were more prevalent than necessary. The RTI system in this project makes use of multiple channels, so this limitation is overcome.

A limitation of the work of Wei et al. [24] is that using ESD antennas significantly reduces network scan frequency, since only one direction can be activated per packet transmission as explained in section 3.6.2. This limitation is not treated in this project, because it was chosen to use multiple channels instead, which already reduced network scan frequency to the limit.

The limitation of an RTI network operating in the 800/900 MHz band proposed by Adler et al. [25] is that target resolution is diminished as a result of the use of larger wavelengths. This may not be beneficial in situations where relatively small targets need to be tracked smaller than one wavelength of 33 cm. This wavelength should be small enough to detect vehicles, including motorcycles. However, due to lack of sufficient

research performed of RTI operating in the 800/900 MHz band (this is the only research published), it was chosen to operate the proposed RTI system in the 2.4 GHz ISM band and leave 800/900 MHz RTI systems for future work.

Concerning related work on simulating RTI networks, one main limitation is overcome. The limitation of Milburn [28] and Cooke [27] is that they do not simulate RSS measurements in a completely realistic way. Their simulated RSS data is based on an initial semi-randomly generated image instead of a simulated communication channel. The main limitation of their simulation model is that they lose accuracy of the simulated RSS data during the process due to their approach of reverse engineering the RSS data. The proposed simulation model overcomes this limitation by simulating RSS data directly from a communication channel based on the ZigBee protocol. This makes it possible to include multipath components and a Rician channel, which both contribute to make the simulated RSS data more realistic and accurate. Furthermore, it implements the link-channel pair selection method [8] that reduces multipath effects, as well as it implements RSS behavioral characteristics described in literature. The latter helps to obtain a more realistic and accurate simulation model.

3 Radio Tomographic Imaging Techniques

This chapter describes the most common techniques and mathematical models used in recently proposed Radio Tomographic Imaging networks. First, a common communication protocol of RTI is explained. In subsequent sections, the theory and mathematics behind RTI and some recent techniques to improve performance are presented, including the use of multiple frequency channels and online calibration. Section 3.6 outlines the analysis of three chosen articles that is used to develop an algorithm for the proposed RTI system.

The first models were presented by Patwari et al. [5] and Wilson et al. [1]. The more recent models described in this section were proposed by Bocca et al. [3], Kaltiokallio et al. [10], Alippi et al. [8] and Anderson et al. [20].

3.1 Communication Protocol

One of the most common communication protocols employed for Radio Tomographic Imaging is the multi-Spin protocol (Sensor Protocol for Information via Negotiation), which is based on the Spin protocol that is provided by TinyOS [5, 29, 3]. The multi-Spin protocol is an autonomous communication protocol, which synchronizes and heals radios in the network.

The multi-Spin protocol controls the order of transmission using a multiple channel Time Division Multiple Access (TDMA) protocol. TDMA synchronizes the switching to a different frequency channel, as well as it controls the switching of slots, cycles and rounds. A slot is where one of the nodes transmits a packet to all other nodes that are in receiving mode, a cycle contains N slots, and a round contains $\mathcal{F}$ cycles. N and $\mathcal{F}$ are the number of nodes and used frequency channels respectively, which are both user-defined and stored in the memory of the radios. The Texas Instruments (TI) CC2531 radios used by Bocca et al. [3] have a 3 ms slot time (2.85 ms for a frame payload length of 62 bytes [24]). With their network of 33 radios that communicate on five frequency channels, a cycle lasts 100 ms and a round 500 ms. Each radio has a built-in identification (ID) number, which is used by TDMA to control the order of transmission.

During initialization, when two nodes or more are turned on, multi-Spin causes the radios to randomly send a packet on the backbone channel, which is the first frequency channel (cycle), until they receive a packet from the other node. Upon receiving this first packet, the radios synchronize themselves and start the communication procedure.

The payload of a transmitted packet consists of its ID number and the latest RSS measurements that the transmitter received from the other radios during the preceding slot. Another synchronized radio (sink node) that is connected to a laptop sends all received RSS data to the laptop, which may either store the raw data or process it directly.

A node may lose synchronization with the network if it does not receive packets for N consecutive slots, due to for example power loss. Such a node is healed by the network in that it will rejoin the network by switching to the backbone channel, where it will wait for the rest of the nodes when a new round is started.

3.2 Received Signal Strength Model

RTI can be attenuation- [8], kernel- [22] or variance-based [29]. Attenuation-based RTI means the change in RSS measurements $\mathbf{y}$ depends on the difference between the current and average (or reference) RSS measured during system calibration. During calibration, no targets are present inside the measurement area. Attenuation is the reduction in signal strength as it is transmitted through a communication channel. Kernel-based RTI calculates a $\mathbf{y}$ vector that depends on the kernel distance between a short-term and long-term histogram of recent RSS measurements [22]. A summary of this work is briefly covered in section 2.1. A RTI network that is variance-based generates a $\mathbf{y}$ vector that reflects the variance of RSS measurements over a particular time window. In the case of Zhao et al.[22], the last four measurements were used as the window size.

This dissertation covers attenuation-based RTI, as it is the most common in literature. Also, a big limitation of kernel- and variance-based systems is that they are not able to track targets that remain static for a longer period of time, as they will gradually fade away (see section 3.5 about online calibration).

The linear model that describes the change in RSS of each link, originating from the correlated shadowing models [5], is given by:

$$\mathbf{y} = \mathbf{W}\mathbf{x} + \mathbf{n} \tag{3.1}$$

where $\mathbf{y}_{L\times 1}$ and $\mathbf{n}_{L\times 1}$ are the change in RSS measurements and noise vectors respectively of the L links in the network, $\mathbf{x}_{V\times 1}$ is the RTI image to be estimated with V being the number of voxels in the image, and $\mathbf{W}_{L\times V}$ is the weight matrix. Vector $\mathbf{x}$ reflects the change of the discretized electromagnetic field of the measured area. The noise vector is assumed Additive White Gaussian Noise (AWGN) in [20] and is implemented in the simulation model. The number of image voxels is dependent on the voxel size, which is a user configurable parameter, and the size of measurement area. How image resolution affects accuracy is demonstrated by Martin et al. [30]. The weight matrix represents a spatial impact model, which relates the effect each link has on each voxel (explained further in subsection 3.2.2). After vector $\mathbf{x}$ is calculated, it is mapped into a two-dimensional matrix that is referred to as the RTI image. Subsection 3.2.1 presents a didactic numeric example of the linear model.

3.2.1 Didactic numeric example of the linear model

An example of an RTI network that contains 8 nodes with an image dimension of 4x4 voxels and a simulated object on voxel 6 is given, as can be seen in Figure 3.

The links that experience signal attenuation due to the simulated object are 4, 12 and 18, as illustrated in the figure by the red dashed lines. As can be observed, the voxels that experience signal attenuation due to the links that pass through the simulated object are brighter than the other voxels.

The numeric representation of the simulated RTI image is given by vector $\mathbf{x}$ that has 16 elements, as shown in Figure 4. Elements 1-16 correspond to the voxel numbers in Figure 3 respectively. It can be observed that element 6 corresponding to the simulated object has a voxel intensity of 21.08, significantly higher than the rest of the voxels. To obtain the change in RSS vector $\mathbf{y}$, the weight matrix $\mathbf{W}$ is multiplied by RTI vector $\mathbf{x}$ and summed with the noise vector $\mathbf{n}$. The columns and rows in the weight matrix correspond to the voxels and links respectively. All the links with nonzero elements in this matrix provide information for the respective voxel. It can be seen from this matrix that the information provided for voxel 6 is given by links 4, 12 and 18. This can also be observed in vector $\mathbf{y}$, where elements 4, 12 and 18 have a higher change in RSS value than the other elements.

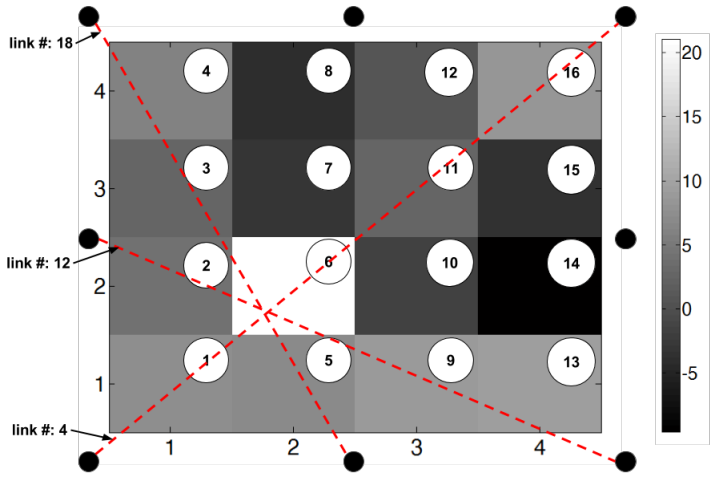

Figure 3 – An example of a 4x4 RTI image with a simulated object on coordinate (2,2). The voxel numbers are given in the top-right corner of each voxel and the links chosen by the weight matrix for voxel (2,2) are shown by the red dashed lines. Their respective link numbers are also given in the figure.

y

	1
1	-1.2411
2	0.4569
3	0.5586
4	23.5573
5	1.1016
6	-0.1495
7	0.6898
8	2.8161
9	1.1144
10	-4.7513
11	2.3095
12	20.2901
13	0.0636
14	0.0201
15	3.1108
16	-1.5957
17	0.8394
18	21.0111
19	-2.9366
20	0.9469
21	-0.2049
22	0.2695
23	1.3099
24	-0.4906
25	1.8634
26	-0.1060
27	-0.6646
28	2.7704

= **W** * **x**

	1
1	11.8470
2	4.6734
3	3.7083
4	5.1604
5	7.7208
6	21.0789
7	-4.2028
8	-2.9432
9	6.9379
10	-0.2797
11	3.2545
12	-0.4904
13	7.7142
14	-9.5875
15	-2.2479
16	4.1639

+ **n**

	1
1	-1.2411
2	0.4569
3	-3.0608
4	9.7074
5	-2.6437
6	-0.1495
7	0.6898
8	2.8161
9	0.7429
10	-5.9787
11	2.3095
12	4.6901
13	-5.9537
14	0.0201
15	3.1108
16	-2.8404
17	-2.0415
18	6.4675
19	-2.9366
20	2.2763
21	-0.5488
22	0.2695
23	1.3099
24	-0.4906
25	-1.4471
26	-0.1060
27	0.6217
28	2.7704

Figure 4 – Numeric example of the linear model y = Wx + n

where the weight matrix **W** is given in Figure 5.

	1	2	3	4	5	6	7	8	9	10	11	12	13	14	15	16
1	0	0	0	0	0	0	0	0	0	0	0	0	0	0	0	0
2	0	0	0	0	0	0	0	0	0	0	0	0	0	0	0	0
3	0.3861	0.3861	0	0	0	0	0.3861	0.3861	0	0	0	0	0	0	0	0
4	0.3433	0	0	0	0	0.3433	0	0	0	0	0.3433	0	0	0	0	0.3433
5	0.3861	0	0	0	0.3861	0	0	0	0	0.3861	0	0	0	0.3861	0	0
6	0	0	0	0	0	0	0	0	0	0	0	0	0	0	0	0
7	0	0	0	0	0	0	0	0	0	0	0	0	0	0	0	0
8	0	0	0	0	0	0	0	0	0	0	0	0	0	0	0	0
9	0	0	0.4855	0	0	0	0	0.4855	0	0	0	0	0	0	0	0
10	0	0	0.3861	0	0	0	0.3861	0	0	0	0	0.3861	0	0	0	0.3861
11	0	0	0	0	0	0	0	0	0	0	0	0	0	0	0	0
12	0	0.3861	0	0	0	0.3861	0	0	0.3861	0	0	0	0.3861	0	0	0
13	0	0.4855	0	0	0.4855	0	0	0	0	0	0	0	0	0	0	0
14	0	0	0	0	0	0	0	0	0	0	0	0	0	0	0	0
15	0	0	0	0	0	0	0	0	0	0	0	0	0	0	0	0
16	0	0	0	0.3861	0	0	0	0.3861	0	0	0.3861	0	0	0	0.3861	0
17	0	0	0	0.3433	0	0	0.3433	0	0	0.3433	0	0	0.3433	0	0	0
18	0	0	0.3861	0.3861	0.3861	0.3861	0	0	0	0	0	0	0	0	0	0
19	0	0	0	0	0	0	0	0	0	0	0	0	0	0	0	0
20	0	0	0	0	0	0	0	0	0	0	0	0.4855	0	0	0.4855	0
21	0	0	0	0	0	0	0	0	0	0	0.3861	0.3861	0.3861	0.3861	0	0
22	0	0	0	0	0	0	0	0	0	0	0	0	0	0	0	0
23	0	0	0	0	0	0	0	0	0	0	0	0	0	0	0	0
24	0	0	0	0	0	0	0	0	0	0	0	0	0	0	0	0
25	0	0	0	0	0	0	0	0	0.3861	0.3861	0	0	0	0	0.3861	0.3861
26	0	0	0	0	0	0	0	0	0	0	0	0	0	0	0	0
27	0	0	0	0	0	0	0	0	0.4855	0	0	0	0	0.4855	0	0
28	0	0	0	0	0	0	0	0	0	0	0	0	0	0	0	0

Figure 5 – Weight matrix corresponding to given example

This numeric example was generated by using the simulation model that computes a vector **y**, the weight matrix and correspondingly the RTI image vector **x** using the procedure described in chapter 5. Therefore, vector **n** was found by $n = y - Wx$.

3.2.2 RSS model based on physical parameters

Originally, an RTI system was designed to work on a single frequency channel [5]. Later, the use of multiple channels was introduced by Bocca et al. [3], with the intention to reduce multipath interference from reflections off objects in the environment and thereby improve location estimates significantly. How the use of multiple channels improves system performance is explained in subsection 3.4.3. The RSS measured on channel c of link l at time instant k, $r_{l,c}(k)$ in dBm, was modeled by Bocca et al. [3] as:

$$r_{l,c}(k) = P_c - L_{l,c} - S_l(k) + F_{l,c}(k) - n_{l,c}(k), c \in \mathcal{F} \tag{3.2}$$

where P_c (dBm) is the node transmit power, $L_{l,c}$ (dB) is the large scale path loss (due to distance, antenna patterns, etc.), S_l (dB) the shadowing loss of attenuating objects, $F_{l,c}$ the fade level (dBm) (from multipath effects), $n_{l,c}$ the measurement noise and $\mathcal{F} = \{1, ..., C\}$ is the set of measured radio frequencies. Measurement noise, as stated by Anderson et al. [20] is assumed AWGN. The set of measured frequencies is user-selectable, where the amount of channels used is a trade-off between reducing the effects of multipath fading and network

scan frequency, as explained in subsection 3.4.3 and 4.1 respectively. Each of the remaining parameters in Equation (3.2) are further discussed throughout this subsection.

The transmit power P_c of all channels is mentioned to be set to the maximum transmit power of the Texas Instruments (TI) CC2531 nodes used by Bocca et al. [3], which is 4.5 dBm.

Large-scale propagation models are those that predict the mean RSS (slow signal variations) over relatively large distances between transmitter and receiver. *Small-scale* propagation models, on the other hand, simulate the fast variations of the signal strength measured by the receiver at relatively short link lengths. The large-scale path loss is given by the ratio (in dB) between the effective radiated power (ERP) P_T (W) and received power P_R (W). The large-scale path loss with the effect of the antenna gains [31] is given by:

$$L_{l,c}(\text{dB}) = 10\log_{10}\left(\frac{P_T}{P_R}\right) = 10\log_{10}\left(\frac{G_T G_T \lambda_c^2}{(4\pi)^2 d_l^2}\right)^{-1} \tag{3.3}$$

$$\lambda_c = \frac{v}{f_c} \tag{3.4}$$

where, in Equation (3.3), G_T and G_T are the antenna gains of the transmitter and receiver respectively, λ_c is the wavelength (m) of channel c and d_l is the distance (m) between transmitter and receiver (T-R) of link l. In Equation (3.4), v is the speed of light (m/s) and f_c is the frequency of channel c (Hz). When antenna gains are $G_T = G_R = 1$, the large-scale path loss is given by:

$$L_{l,c}(\text{dBm}) = 10\log_{10}\left(\frac{\lambda_c}{4d_l\pi}\right)^{-2} + 30 = -20\log_{10}\left(\frac{\lambda_c}{4d_l\pi}\right) + 30 \tag{3.5}$$

The path loss model shows that when keeping channel frequency (thus wavelength) constant, increasing T-R distance will increase the path loss (decrease P_R and thus increase ratio between P_T and P_R) as a result of signal attenuation. In the path loss model, an increase in distance by a factor 2 will lead to a linear increase of path loss of 6 dBm. One of the channels used by Bocca et al. [3] is ZigBee channel 15, which corresponds to 2425 MHz, or a wavelength of 0.124 m. At a T-R distance of 1.5 m, the theoretical path loss is 73.7 dBm.

The shadowing loss $S_l(k)$ of link l is modeled as [1]:

$$S_l(k) = \sum_{j=1}^{V} w_{l,j} x_j(k) \tag{3.6}$$

The shadowing loss at time instant k is therefore a sum of products between the weights of weight matrix $\mathbf{W}$ and voxel j, which ranges from 1 to total number of voxels V.

The weight matrix $\mathbf{W}$ is governed by a spatial impact model, which determines the weight elements by the size of the ellipse that represents the area measured by each link, where the foci of the ellipse are the transmitter and receiver radios. All the voxels contained within the ellipse are dependent on the link that belongs to that ellipse, as demonstrated in Figure 6. The blue voxels together form the weighted region selected by the ellipse and therefore represent the measured area of the dashed radio link. Consequently, the larger the width λ of the ellipse, the larger the area that the link will cover, thus the more voxels that will be selected. This also means the detail of where attenuation occurs may be reduced. Information may be lost if the ellipse width is too small, effectively eliminating voxels that do represent the attenuation of the respective link. Wilson et al. [1] demonstrate the effect of ellipse width on localization error. Bocca et al. [3] have set λ to 0.02 m. The spatial impact model causes the weight to be zero where link l does not affect voxel j, and non-zero if the area of the ellipse of link l covers the center of voxel j. The presence of a an object on voxel j causes signal attenuation (shadowing) on the links that cover voxel j. The weights are calculated as follows [3]:

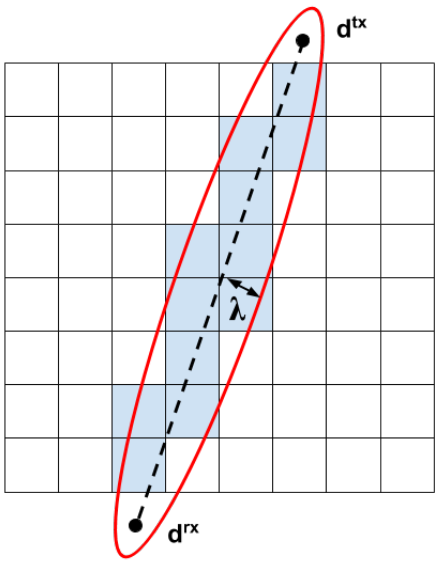

Figure 6 – Ellipse (in red) of an arbitrary radio link (dashed line) whose area selects the voxels (in blue) that it affects. A black dot represents a radio.

$$w_{l,j} = \begin{cases} \frac{1}{d_l} & \text{if } d_{l,j}^{tx} + d_{l,j}^{rx} < d_l + \lambda \\ 0 & \text{otherwise} \end{cases} \tag{3.7}$$

where $d_{l,j}^{tx}$ and $d_{l,j}^{rx}$ are the Euclidian distances between the center of voxel j and the transmitter and receiver of link l respectively, and d_l is the length of link l. Therefore, the shorter and more reliable links are weighted more than the longer, less reliable links. To calculate the weight matrix, therefore, the number and position of the nodes and voxels needs to be known a priori.

The fading gain is calculated differently in various works [8] [3] [23] that each are used for a different link selection method, but Alippi et al. [8] demonstrate that their method outperforms the rest. Therefore, the fading gain of [8] will be presented. The fading gain $F_{l,c}$ of link l on channel c is estimated as:

$$F_{l,c} = \bar{r}_{l,c} - P(d_l) \tag{3.8}$$

where

$$P(d_l) = P_0 - 10\eta \log_{10}\left(\frac{d_l}{d_0}\right) \tag{3.9}$$

where $\bar{r}_{l,c}$ is the average RSS of link l on channel c measured during the initial calibration period (no person present inside monitored area), $P(d_l)$ is the *log-distance path loss model*, P_0 is the transmit power reference loss at reference distance d_0, η is the path loss exponent and d_l is the length of link l. $P(d_l)$ is therefore dependent on the logarithm of the distance between communicating nodes, which can be observed in Figure 7a. Parameter η indicates the rate at which the path loss increases with distance, which is affected by the propagation environment (see subsection 3.4.1 for propagation mechanisms). A typical path loss exponent value in a line-of-sight (LOS) set-up is between 1.6 and 1.8, whereas in shadowed urban areas it can be between 3 and 5 [31].

Experimental raw RSS data published online by Wilson et al. [2] for academic purposes was used to generate Figures 7a and 7b in MATLAB. Figure 7a displays averaged experimental data from an empty area

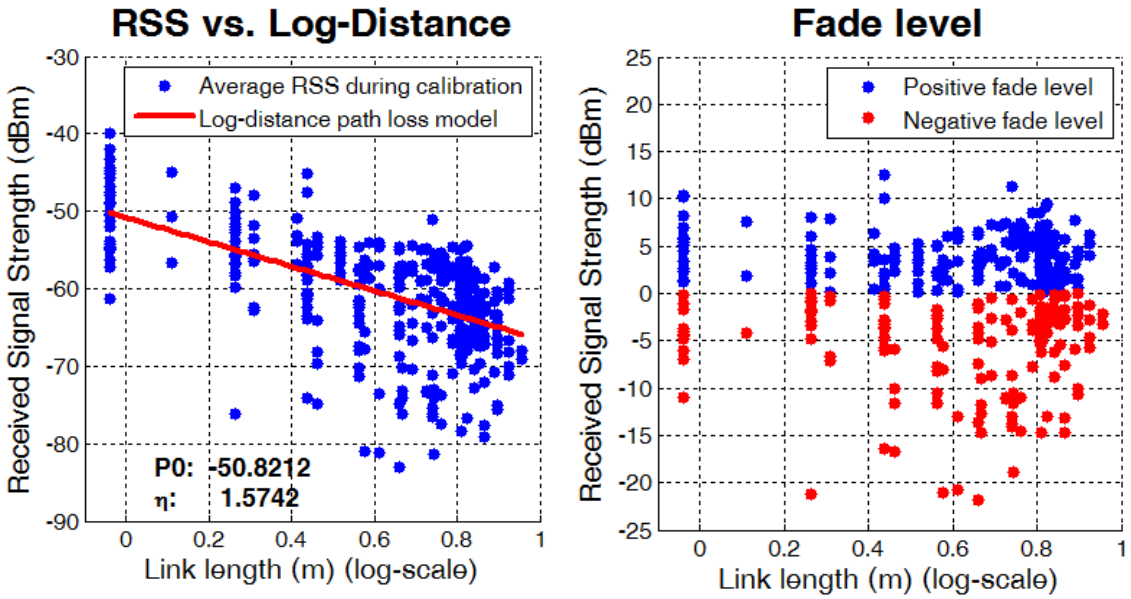

(a) (b)

Figure 7 – Experimental Received Signal Strength data published by Wilson et al. [2] processed into displaying (a) average RSS (dBm) during calibration period versus log-distance (m) and its corresponding log-distance path-loss model with corresponding parameters P_0 and η displayed in the graph. Figure (b) shows the fade level as calculated using Equation (3.8), where the blue and red data points are the positive and negative fade levels respectively, shown to more easily distinguish between the two levels. Both graphs were produced in MATLAB.

(with no people) being plotted against log-distance with its corresponding log-distance path loss model. The parameters for the path loss model are also shown, which are $P_0 = -50.8$ dBm and $\eta = 1.6$ respectively. The calculated path-loss exponent of 1.6 confirms what is stated as being an expected path loss exponent by Rappaport [31], as most of the links were in LOS, whereas some links were obstructed by two trees inside the measured area. Figure 7b shows the fade level calculated using Equation (3.8). To facilitate distinguishing between the polarity of the fade levels, the positive and negative fade levels are marked as blue and red respectively. As can be seen, positive fade levels seem to be more constant and stay under 15 dBm, whereas negative fade levels indicate larger variance with an RSS range of up to -25 dBm. This behavior is further explained in section 3.4.2.

The relationship between measured RSS $r_{l,c}(k)$ of Equation (3.2) and change in RSS $y_{l,c}(k)$ of Equation (3.1) at time k is given by [8]:

$$y_{l,c}(k) = \bar{r}_{l,c}(k) - r_{l,c}(k) \tag{3.10}$$

Reference RSS $\bar{r}_{l,c}(k)$ is dependent on time k, as it is updated after each iteration in a process called online calibration that reduces the effect of time variance. The links and channels in Equation (3.10) are preselected in a method that selects only the most reliable channel of links in a positive fade level, which is further detailed in subsection 3.4.3. All the elements in $y_{l,c}(k)$ that do not belong to the selected link-channel pairs are set to zero.

3.3 Generating a Radio Tomographic Image

To obtain an RTI image $\hat{\mathbf{x}}_{MAP}$, a Maximum A Posteriori (MAP) estimator was used by Anderson et al. [20]. An estimate for the RTI image $\mathbf{x}$, given the RSS observations $\mathbf{y}$, is found that maximizes:

$$\begin{aligned}\hat{\mathbf{x}}_{MAP} &= \arg\max_x f(\mathbf{x}|\mathbf{y}) \\ &= \arg\max_x \frac{f(\mathbf{y}|\mathbf{x})f(\mathbf{x})}{f(\mathbf{y})} \\ &= \arg\max_x f(\mathbf{y}|\mathbf{x})f(\mathbf{x})\end{aligned} \tag{3.11}$$

The second equality in Equation (3.11) comes from Bayes' theorem. In the third equality, the *a priori* probability $f(\mathbf{y})$ in the denominator is removed, as it does not influence in finding the optimum $\hat{\mathbf{x}}_{MAP}$. Anderson et al. [20] assume that *a posteriori* probability $f_{\text{awgn}}(\mathbf{y}|\mathbf{x})$ in Equation (3.12) follows an AWGN fading model with mean $\mathbf{W}\mathbf{x}$ and noise variance $\sigma_n^2\mathbf{I}_L$, where $\mathbf{I}_L$ is the $L \times L$ identity matrix. The mean and variance of the AWGN fading model are directly related to the linear model described by Equation (3.1). Furthermore, the authors consider a Gaussian Bayesian prior on $\mathbf{x}$ in Equation (3.13) with covariance matrix C_x, since the elements in the image vector $\mathbf{x}$ are correlated to each other and the authors mention this assumption is equivalent to using regularization. The regularization term $\sigma_n^2\mathbf{C}_x^{-1}$ in Equation (3.19) is required to solve the ill-posed inverse problem, since the matrix $\mathbf{W}^T\mathbf{W}$ is typically not full rank, which occurs in situations where the number of links is significantly smaller than the number of voxels. Regularization is also used to reduce noise and effectively smoothen the estimated image, meaning the higher the noise variance σ_n^2, the more the image is smoothened. The Gaussian prior has mean $m\mathbf{1}_{V\times 1}$ (which is typically zero), where $\mathbf{1}$ is a vector of ones of size $V \times 1$ and covariance matrix $\mathbf{C}_x$ of size $V \times V$. The covariance matrix is given by Equation (3.14). The Gaussian models for the MAP estimator are shown below:

$$f_{\text{awgn}}(\mathbf{y}|\mathbf{x}) \sim \mathcal{N}(\mathbf{W}\mathbf{x}, \sigma_n^2\mathbf{I}_L) = \frac{1}{\sqrt{2\pi}\sigma} e^{\frac{-||\mathbf{y}\text{ - }\mathbf{W}\mathbf{x}||^2}{2\sigma_n^2\mathbf{I}}} \tag{3.12}$$

$$f_{\text{gauss}}(\mathbf{x}) \sim \mathcal{N}(m\mathbf{1}_{V\times 1}, \mathbf{C}_x) = \frac{1}{\sqrt{2\pi}\sigma} e^{\frac{-||\mathbf{x}-m\mathbf{1}||^2}{2\mathbf{C}_x}} \tag{3.13}$$

$$[C_x]_{j,i} = \sigma_x^2 e^{-d_{j,i}/\delta_c} \tag{3.14}$$

where σ_x^2 is the variance of voxel intensities, $d_{i,j}$ is the distance between the centers of voxels i and j, and δ_c is the voxels' correlation parameter (see section 4.3 for an example regarding this parameter). The covariance matrix is an exponential function, which has been shown to be useful in approximating the spatial covariance of an attenuating field [6, 32]. Moreover, Wilson et al. [1] mention the covariance matrix C_x can be closely approximated to the covariance that results from modeling the spatial attenuation as a Poisson process, which is frequently assumed for random positioning of objects in an arbitrary space.

Since the objective of the MAP estimator is to optimize $\mathbf{x}$, only the argument of the exponent of Equations (3.12) and (3.13) is required. The MAP estimator then becomes:

$$\begin{aligned}\hat{\mathbf{x}}_{MAP} = \arg\max_x \Big(&-\frac{1}{2}||\mathbf{y}\text{ - }\mathbf{W}\mathbf{x}||^2(\sigma_n^2\mathbf{I})^{-1} - \frac{1}{2}||\mathbf{x}-m\mathbf{1}||^2(\mathbf{C}_x)^{-1}\Big) \\ &= \arg\min_x \Big(||\mathbf{y}\text{ - }\mathbf{W}\mathbf{x}||^2 + \sigma_n^2\mathbf{C}_x^{-1}||\mathbf{x}-m\mathbf{1}||^2\Big)\end{aligned} \tag{3.15}$$

$$\hat{\mathbf{x}}_{MAP} = (\mathbf{W}^T\mathbf{W} + \sigma_n^2\mathbf{C}_x^{-1})^{-1}(\mathbf{W}^T\mathbf{y} + m\sigma_n^2\mathbf{C}_x^{-1}\mathbf{1}) \tag{3.16}$$

In Equation (3.15), the argument has been multiplied by $-2\sigma_n^2$, thereby turning the objective of the MAP estimator to minimize the objective function. Equation (3.16) is a regularized least-squares solution. To see the see full working of this result, see Appendix A. Anderson et al. simplify Equation (3.16) by substituting $m\sigma_n^2\mathbf{C}_x^{-1}$ with a bias term β, meaning their final generic form of the MAP estimator of the Radio Tomographic Image becomes:

$$\hat{\mathbf{x}}_{MAP} = (\mathbf{W}^T\mathbf{W} + \sigma_n^2\mathbf{C}_x^{-1})^{-1}(\mathbf{W}^T\mathbf{y} + \beta\mathbf{1}) \tag{3.17}$$

This may be simplified to:

$$\hat{\mathbf{x}}_{MAP} = \Pi(\mathbf{W}^T\mathbf{y} + \beta\mathbf{1}) \tag{3.18}$$

where

$$\Pi = (\mathbf{W}^T\mathbf{W} + \sigma_n^2\mathbf{C}_x^{-1})^{-1} \tag{3.19}$$

Regularization matrix (3.19) only needs to be computed during initialization (once before real-time operation) and remains constant until the nodes are displaced or image dimensions are modified, because of the required adjustment of the weight matrix. This reduces computational cost while the system is running. Anderson et al. show that the regularization term in Equation (3.19) can be replaced by the Tikhonov matrix $\mathbf{Q}$, as given by:

$$\Pi = (\mathbf{W}^T\mathbf{W} + \alpha\mathbf{Q})^{-1} \tag{3.20}$$

$$\Pi = (\mathbf{W}^T\mathbf{W} + \alpha(\mathbf{D}_X^T\mathbf{D}_X + \mathbf{D}_Y^T\mathbf{D}_Y))^{-1} \tag{3.21}$$

where $\mathbf{Q}$ is replaced by a difference matrix that approximates the derivative of the image, also known as H1 regularization [1]. The difference matrices $\mathbf{D}_X$ and $\mathbf{D}_Y$ are the difference operators for the horizontal and vertical directions of a 2D image respectively (see [27] for a detailed example). Anderson et al. show that smoothing parameter α can be set to $\alpha \approx 0.3$ for weak smoothing and $\alpha \approx 30$ for strong smoothing. The higher the smoothing parameter, the more emphasis is placed on the regularization term and the less the effect of noise. By using Tikhonov regularization, Anderson et al. show that voxels close to the center of the measured area are given more bias than those closer to the border of the network. The advantage of using Tikhonov regularization is reduced computational cost and it does not require parameters σ_n^2 and δ_c to be determined, making it a more generalized solution. The advantage of the more specific solution offered by the covariance matrix is that the RTI image can be "taylored" to obtain a result that is more optimized than the Tikhonov solution. Tikhonov regularization is also used by [1, 24, 25, 30, 33], who arrive at the same result, without the bias term β, by obtaining the least-squares solution to the objective function:

$$f(\mathbf{x}) = \frac{1}{2}||\mathbf{Wx - y}||^2 + \alpha||\mathbf{Qx}||^2 \tag{3.22}$$

$$f(\mathbf{x}) = \frac{1}{2}||\mathbf{Wx - y}||^2 + \alpha(||\mathbf{D}_X^T\mathbf{x}||^2 + ||\mathbf{D}_Y^T\mathbf{x}||^2)^2 \tag{3.23}$$

By taking the derivative of Equation (3.23) with respect to $\mathbf{x}$ and setting the result to zero (similar to what is shown in Appendix A), the following Tikhonov solution is obtained:

$$\hat{\mathbf{x}} = (\mathbf{W}^T\mathbf{W} + \alpha(\mathbf{D}_X^T\mathbf{D}_X + \mathbf{D}_Y^T\mathbf{D}_Y))^{-1}\mathbf{W}^T\mathbf{y} \tag{3.24}$$

3.4 Multipath Fading: Problems and Solutions

In a radio propagation environment with surfaces, radio waves are reflected, diffracted, shadowed and scattered, which all have an effect on multipath fading. These propagation mechanisms and multipath fading are explained in subsection 3.4.1. The RSS dynamics of different frequency channels is illustrated in subsection 3.4.2, and how the link-channel selection method with multiple channels reduces the negative effects of multipath fading is outlined in 3.4.3.

3.4.1 Multipath Fading

Reflection is where a radio wave collides and bounces off an object with dimensions relatively large with respect to the wavelength of the propagating radio wave. Examples of such objects include buildings, walls and the surface of the earth. A radio wave is *diffracted* if it is obstructed by a surface with sharp edges or irregularities, causing multiple waves to be bounced off into different directions, including waves that bend (propagate) around the obstacle. *Shadowing*, or medium-scale fading, is closely related to diffraction, and occurs when a signal is attenuated as it passes through or diffracts around objects in the signal path [6]. This is what RTI is primarily based on. *Scattering* is where the radio waves are spread out (diffused) in all directions after colliding with an irregular surface that is relatively small compared to the wavelength of the incident radio wave. It is similar to diffraction in that it spreads out multiple radio waves, but differs in that the waves do not propagate around the obstacle. Examples of objects that cause scattering are street signs, lamp posts and trees [31].

Reflection, diffraction, shadowing and scattering cause multiple versions of the same transmitted signal to arrive with a different phase and gain at the receiver. The RSS at the receiver reflects the phasor sum of the radio waves that arrive at the receiver's antenna. The intensity of the phasor sum is dependent on the receiver's position and the center frequency of the radio signal. A constructive phasor sum (constructive interference) is the result of waves that arrive with the same phase, which is referred to as *anti-fade*. Waves with opposite phase cause a destructive phasor sum (destructive interference) and are referred to as *deep fade*. These interference phenomena are described as *multipath fading* [3, 8, 10, 11].

3.4.2 RSS Dynamics

Bocca et al. [3] demonstrate that every frequency channel of each link has different RSS dynamics when a person crosses the link line, which was modeled in [34] and referred to as *fade level*. This causes a specific RSS variance for each link. RSS dynamics is also dependent on link length: the larger the distance between the radios, the less the signal strength is affected when the link is blocked. A link in anti-fade has a positive $F_{l,c}$ as shown in Figure 7b, which causes the average RSS to decrease when the link is blocked. A link in deep fade has the opposite effect of a link in anti-fade and shows much larger variations independent of it being blocked. This is an undesirable and unreliable behavior, as it may cause false positives when a target is not blocking the link.

All these behaviors are illustrated in Figures 8 and 9, which were initially presented by Bocca et al. [3]. The figures show the behavior of three ZigBee channels A, B and C operating on the same link, which refer to channels 15 (2425 MHz), 22 (2460 MHz) and 26 (2480 MHz) respectively. The communication link is crossed by a person two times. The figures differ from each other in the link length: Figure 8 has radios positioned 1.5 m from each other, whereas Figure 9 has a distance of 5 m between the T-R radios. These figures illustrate how link length affects RSS dynamics.

In the unblocked steady-state, channel A behaves relatively constant and is clearly in anti-fade, only experiencing RSS variations of 2 to 3 dB. When it is blocked, the signal clearly drops with around 8 dB and 5 dB in the first and second figures respectively. This difference in signal drop is due to link length, where a smaller drop is experienced at larger link lengths, thereby making it more difficult to detect a target as node-node distance increases. The signal quickly recovers to its steady-state after the person crossed the link. The steady-state RSS level in this test is about 6 dB lower in channel A at a link length of 5 m than 1.5 m, which is another effect of link length. In Figure 8, channel B behaves similar to channel A, though in Figure 9 channel B is more comparable to channel C. Channel C in both figures is clearly in deep fade, as it behaves unpredictably due to its large RSS variance throughout the measurement period. These are unreliable channels that reduce RTI performance, and which should preferably be filtered out. This is why several researchers [8, 3, 23] have proposed a selection method that only allows the most reliable channels of anti-fade links to be used.

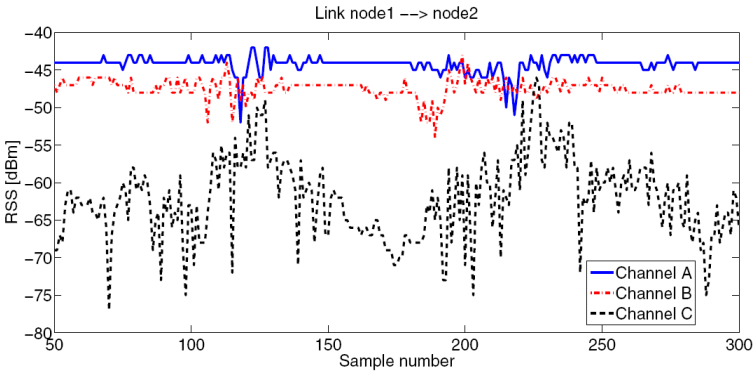

Figure 8 – RSS measurements of three different channels operating on the same link, where the nodes are separated by 1.5 m and installed 1 m from the floor. The link is blocked by a person two times during the measuring period. Channels A, B and C refer to ZigBee channels 15 (2425 MHz), 22 (2460 MHz) and 26 (2480 MHz) respectively [3].

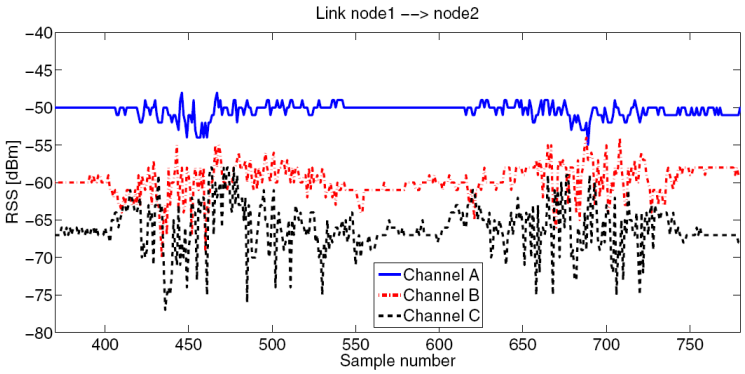

Figure 9 – RSS measurements of three different channels operating on the same link, where the nodes are separated by 5 m and installed 1 m from the floor. The link is blocked by a person two times during the measuring period [3]. The channels are equal to the channels shown in Figure 8.

3.4.3 Link-Channel Selection Method

Several works employ a different method to make use of information from multiple channels to improve RTI performance [8, 3, 23]. Alippi et al. [8] proved, by comparing their method to the others, that their link-channel selection method is most effective in using multiple frequency channels, and will therefore be discussed in this subsection.

Alippi et al. mention their method has two advantages. The first being increased robustness against RSS link variance and environmental noise as the chosen link-channel pairs filter out noisy links, and the second is increased energy efficiency. Since some links may not be selected, it means the receiving radios belonging to those links may be switched off during a TDMA slot (see 3.1 about TDMA slot).

In the first stage of link-channel pair selection, a set of link-channel pairs in anti-fade $\mathcal{L}_p$ is chosen:

$$\mathcal{L}_p = \{(l, c) : F_{l,c} > 0\} \tag{3.25}$$

where l and c are the link and frequency channel respectively, and $F_{l,c}$ is the fade level as calculated by Equation (3.8) and demonstrated in Figure 7b. Anderson et al. update the fade level and thus the selected link-channel pairs every two hours, over a reference RSS collection time window of five minutes. A more dynamic environment will require a faster update frequency, at the expense of energy consumption.

The second stage is selecting only link-channel pairs with an average RSS (measured during initial calibration) higher than the grey region, which is a region where the RSS is close to the receiver's sensitivity threshold. Links in the grey region may be long in length or experience a lot of obstructions, causing them to be unpredictable. The researchers, who used the TI CC2531 radios, set a grey region threshold of $\Upsilon_r = -90$ dBm, resulting in the following set of link-channel pairs with average RSS higher than Υ_r:

$$\mathcal{L}_r = \{(l, c) : \bar{r}_{l,c} > \Upsilon_r\} \tag{3.26}$$

Thirdly, the intersection between the previously found sets is obtained and defined as:

$$\mathcal{L}_s = (\mathcal{L}_p \bigcap \mathcal{L}_r) \tag{3.27}$$

Although it may be close to guaranteed that the grey region links have already been filtered out in $\mathcal{L}_p$, Alippi et al. still include this step in the selection procedure to make sure of this.

In the fourth and final stage, the set of selected link-channel pairs $\mathcal{L}$ is defined as the set in which, for each link in $\mathcal{L}_s$, only the frequency channel in $\mathcal{C}$ (set of measured channels) with largest weight $\rho_{l,c}$ is chosen, as given by:

$$\mathcal{L} = \left((l, c) : (l, c) \in \mathcal{L}_s \wedge c = \max_{j \in \mathcal{C}} \rho_{l,j}\right) \tag{3.28}$$

where

$$\rho_{l,c} = \begin{cases} F_{l,c}/\sigma^2_{l,c} & \text{if } (l, c) \in \mathcal{L}_s \\ 0 & \text{otherwise} \end{cases} \tag{3.29}$$

where $\sigma^2_{l,c}$ is the RSS variance measured during initial calibration. The weight of a link-channel pair is therefore higher with lower, and hence more reliable, variance link-channel pairs. All the elements in $y_{l,c}(k)$ in Equation (3.10) that do not belong to the selected link-channel pairs are set to zero.

3.5 Online calibration

Calibration is required to obtain a reference RSS to compare the current RSS with an empty (default) area. In static time invariant environments, such as inside buildings or other indoor environments where relatively little movement occurs other than targets, one offline calibration during initialization is usually sufficient for long-term operation. However, in dynamic time variant environments where objects inside the measurement area are added or moved, or where wind-drive foliage and weather changes like rain occur (although Anderson et al. [20] mention rain has negligible impact on signal attenuation), the reference RSS changes over time. This effect is illustrated in Figure 10 taken from [3], where a chair is placed between samples 200 and 350. As can be observed, the RSS measured on all three channels drop significantly, from 5 dB on channel B to 10 dB on channel C.

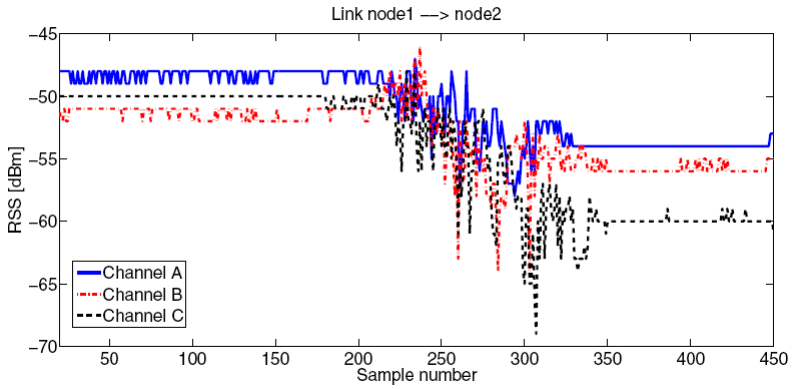

Figure 10 – The effect on RSS attenuation when a chair is placed on a radio link between samples 200 and 350. The radios are spaced 4 m apart and 1 m elevated from the floor [3]. Channels A, B and C operate in the same frequencies as in Figures 8 and 9.

Several works [22, 35] have proposed an online calibration method, which rely on the difference between a short- and long-term RSS histogram and a moving average respectively. These methods, however, are not effective when the target remains stationary for a longer period of time, as they will gradually fade out from the images. A method that calibrates online that is effective in both short- and long-term measuring periods is presented by [3] and later also employed by [8].

The online calibration method acts like a spatial filter, which only calibrates selected link-channel pairs that are not attenuated by targets. The system thus requires that initially the monitored area does not have any targets. Once the initial reference RSS is obtained, the online calibration method uses the estimate of the target's position calculated from the previous iteration and averages elements of links in a first in, first out (FIFO) buffer, which contains RSS measurements of all selected link-channel pairs collected over a pre-determined time window length, that do not intersect the target. The reference RSS vector is then updated with the new averages.

Figure 11 is an RTI image with a person located at the red blob. The links intersecting the area enclosed by the white dashed circle, referred to as the grating area, are to be filtered out and be excluded from online calibration. The grating area is centered at the position estimate and has a user settable radius.

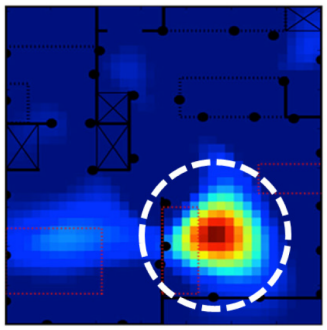

Figure 11 – An RTI image with a red blob that indicates the location estimate of a person and a white dashed circle, which is the grating area that is filtered for online calibration [3].

3.6 Article Analysis

In this section, the RTI implementation presented in three selected articles are analyzed with respect to their computational cost, localization accuracy and robustness. The proposed vehicle tracking algorithm, which is described in chapter 4, is based on some of the methods proposed by the selected articles, as well as newly proposed methods. The methods to be implemented should allow the proposed RTI system to be able to meet the requirements described in section 1.4. The requirements state that the RTI system should be able to measure occupancy and velocity of multiple vehicles real-time, fast enough to track vehicles moving at 50 km/h, and be robust against RSS link variance and RSS time-variance. RSS link variance is caused by multipath effects, while RSS time-variance is dependent on changes in the environment that are non-related to the target, such as random objects being placed in the area or weather effects, such as wind that sways leaves, branches or the nodes themselves. Performance is greatly influenced if the receiver node is moved only by a fraction of its wavelength [22], [24]. The techniques described in this section are covered in various sections of chapter 3.

The three analyzed articles are "RTI Goes Wild: Radio Tomographic Imaging for Outdoor People Detection and Localization" by Alippi et al. [8], "dRTI: Directional Radio Tomographic Imaging" by Wei et al. [24] and "Radio Tomography for Roadside Surveillance" by Anderson et al. [20].

3.6.1 "RTI Goes Wild: Radio Tomographic Imaging for Outdoor People Detection and Localization"

As briefly described in section 2.1, Alippi et al. [8] from the Polytechnic University of Milan and University of Utah developed a state of the art outdoor attenuation-based RTI network enhanced by using multiple channels, background subtraction and online calibration, which is able to track multiple stationary and moving people real-time.

Computational Cost

Each estimated radio tomographic image $\hat{\mathbf{x}}_{V\times 1}$ in Equation (3.30) depends on the regularized least-squares solution $\Pi_{V\times L}$ [5, 9, 23, 29, 35] and the change in RSS attenuation vector $\mathbf{y}_{L\times 1}$. The number of links, nodes and voxels are given by L, N and V respectively. Vector $\mathbf{y}$ consists of the RSS attenuation change measured from all fade-level based selected link-channels and is assumed to be a spatial integral of the propagation field of the monitored area. For all non-selected link-channels, the RSS change is set to zero. Matrix Π is only required to be computed once before operation, which ensured real-time estimation of the image $\hat{\mathbf{x}}$. Π

consists of a simple weight matrix $\mathbf{W}_{L\times V}$, regularization parameter σ_n^2 and *a priori* covariance matrix C_x:

$$\hat{\mathbf{x}} = \Pi\mathbf{y} \tag{3.30}$$

$$\Pi = (\mathbf{W}^T\mathbf{W} + \sigma_n^2 C_x^{-1})^{-1}\mathbf{W}^T \tag{3.31}$$

The difference between Equations (3.30) and (3.18) is that the latter employs a bias term and requires more computations, as demonstrated in subsection 5.2.5.

For the localization and tracking of multiple targets, the method of [9] was used. Image $\hat{\mathbf{x}}$ requires VL multiplications while the system is operating in real-time, meaning computational cost increases with amount of voxels and links. The number of links L is given by:

$$L = \frac{K(K-1)}{2} \tag{3.32}$$

where K is the number of radio nodes.

RSS data from the complete network consisting of 20 Texas Instruments CC2531 nodes was collected every 340 ms, which they mention is sufficiently fast to track moving people. Computation time for an RTI estimate was not mentioned, but is assumed to be less than one network scan of 340 ms as was simulated and shown in Figure 18.

Localization Accuracy

The results show that the researchers achieve an average location Root Mean Square Error (RMSE) of 3.2 m (Euclidian distance) in an RTI network deployed in a densely forested environment with radios attached to trees. They compared their results in the same measurement environment to the state of the art fade level-based model introduced by Kaltiokallio et al. [10] obtaining a higher location error of 4.3 m. The authors mention that the main reason for the improved accuracy of their method, is due to the use of their node-specific path loss model (see *Robustness* in the next subsection). Although not mentioned in their paper, it is assumed that Alippi et al. optimized all parameters when using the method of [10] to allow a fair comparison.

Robustness

Alippi et al. have four methods to increase robustness against intrinsic motion. They achieve a 0.04% false alarm rate, where a person was falsely detected for a total of 12 s in the monitored area during an eight hour measurement period with wind of varying intensity. This is a significant improvement compared to the state of the art [10], where they obtained a 0.74% false alarm rate, during which there were 12 false alarms that lasted a total of three minutes.

One of the methods is to select which links and which one of their channels are most reliable to use for image estimation. After pre-determined fixed time intervals, only link-channel pairs are selected that are in anti-fade and have an average RSS higher than the receiver sensitivity threshold. From these selected link-channels, only the channel that has the lowest variance of each link is selected. Intrinsic noise has high variance, which is filtered out this way.

The second method is an online calibration technique, which applies a spatial filter that only updates the reference RSS of selected link-channel pairs not attenuated by stationary targets. The online calibration method uses a FIFO buffer that gathers RSS data in a time window of five seconds.

The third method is a node-specific path loss model that is used to calculate fade level for each node. In other words, each node n is modeled to have its own path loss exponent η_n and transmit reference power P_0^n (see 3.2.2 about the log-distance path loss model). The authors mention that using a node-specific path loss model, the system is more robust against hardware variability factors (including relative antenna orientation between communicating radios) and local environmental differences (like proximity of nodes to dense foliage). Fade levels are updated after each pre-determined fixed long-term time interval.

The fourth method is background subtraction, which is a technique to better distinguish the blobs in the generated image corresponding to real targets from the blobs caused by environmental noise. The method is widely used in machine vision for the detection and tracking of moving targets, which can be applied to RTI in the sense that frames are generated after every network scan, creating the effect of being a video. In a Cumulative Distribution Function (CDF) comparing the system performance with and without background subtraction, the authors demonstrate that the system is overall more accurate with background subtraction, but makes a minimal difference.

3.6.2 "dRTI: Directional Radio Tomographic Imaging"

As briefly discussed in section 2.1, Wei et al. [24] propose the use of ESD antennas to improve RTI network performance. ESD antennas focus the radiated power in selected directions to reduce multipath effects and thereby reduce noise in communication links. The authors used ESD antennas that have six directions, meaning 36 possible transmit-receive antenna direction pairs are possible, which they refer to as *Pattern Pairs*. Communication in both directions leads to a maximum number of Pattern Pairs of 72 for each link.

Computational Cost

Using the proposed directional antennas comes at a cost of network scan time as each direction is sequentially switched, making the dRTI system difficult to scale to larger network sizes.

The authors proposed three methods to select the Pattern Pairs of each link, of which the fade level-based method yields highest performance. This method selects the top k Pattern Pairs with highest fade level. The change in RSS vector $\mathbf{y}$ is calculated as the sum of the absolute difference between the current $R_{i,j}(t)$ and reference RSS $\bar{R}_{i,j}$ for each selected Pattern Pair $j \in F_i$ of link i, as given by:

$$y_i(t) = \sum_{j \in F_i} |R_{i,j}(t) - \bar{R}_{i,j}| \tag{3.33}$$

where F_i contains the fade level of the k selected Pattern Pairs of link i. Computational complexity hence increases with parameter k.

The RTI model used by Wei et al. is the same as in [1], which is a least-squares solution with Tikhonov regularization as shown by Equations (3.30) and (3.31). In the work of Wei et al., however, only 21 links (7 nodes) and 700 voxels were used instead of 378 links (28 nodes) and 1764 voxels in [1]. This reduces the number of multiplications by approximately a factor 45, since image estimation requires VL multiplications (see section 3.6.1). This provides strong evidence that images were generated real-time, but image generation time remains unknown.

Localization Accuracy

Wei et al. compared their system to the multi-channel omni-directional RTI network in [23], showing that their proposed system has a tracking performance improvement of 42% in an open LOS-environment at the

90th percentile of the CDF representing tracking error. The authors, however, have not compared their results to the latest high performance multi-channel RTI network [8], which might have produced similar or even better results.

Robustness

The authors have not tested their proposed RTI system outdoors nor have they mentioned any effects of intrinsic motion. However, the authors do present system performance results with False Positive (FP) and False Negative (FN) figures, which is a way to measure system robustness. They show that their proposed dRTI method yields significantly lower FP and FN results compared to mean- and variance-based RTI, as well as multi-channel RTI.

3.6.3 "Radio Tomography for Roadside Surveillance"

As briefly discussed in section 2.1, Anderson et al. [20], four members of the Institute of Electrical and Electronics Engineers (IEEE), published a paper that aimed to improve RTI modeling and algorithms in a roadside surveillance environment.

Computational Cost

Three improvements were proposed that all add to computational cost compared to the initial RTI approach proposed by Wilson et al. [1]. The solutions include an extra bias term to the commonly used regularized least squares solution of Equation (3.24), a way to deal with negative data in the observations as a result of bad calibration or noise, and combining multiple frames to produce a more accurate final image.

To generate an image estimate, Anderson et al. obtained a least-squares solution $\Pi_{V\times V}$ with *H1 regularization* given by Equation (3.20), which is a form of Tikhonov regularization. Additional to this expression and using the Maximum A Posteriori (MAP) estimator, they obtained Equation (3.18), where the bias term β is empirically determined.

Computation of Equation (3.18) requires $V^2L + VL = (V+1)(VL)$ multiplications after each real-time iteration, thereby increasing the number of multiplications by a factor $V+1$ relative to Equation (3.30). The addition of the bias term β does not increase computational cost notably, as the operations consist of summations only.

Anderson et al. mention that negative elements in $\mathbf{y}$ may occur as a result of inadequate initial calibration or significant amount of noise. To deal with negative data in the observations, the researchers iterate their proposed simple three-step method three times. The method is based on removing negative elements of $\hat{\mathbf{x}}_{MAP}$ and exclude the respective columns of $\mathbf{W}$ and $\mathbf{D}$, after which $\hat{\mathbf{x}}_{MAP}$ is recomputed until it does not contain any more negative entries. This method produces results similar to background subtraction, thereby denoising the image. Computation time increases proportional to the number of iterations, where the authors mention that three iterations were sufficient.

The authors combine three frames into a final, more accurate, image. Instead of $\mathbf{W}$ and $\mathbf{y}$ in Equations (3.20) and (3.18) respectively, they propose:

$$\mathbf{W}_{\text{stack}} = \begin{bmatrix} \mathbf{W}\mathbf{J}^{-v} \\ \mathbf{W} \\ \mathbf{W}\mathbf{J}^{v} \end{bmatrix}, \quad \mathbf{y}_{\text{stack}} = \begin{bmatrix} \mathbf{y}^1 \\ \mathbf{y}^2 \\ \mathbf{y}^3 \end{bmatrix} \tag{3.34}$$

where **J** is a shifting matrix that shifts a frame left or right, v is the vehicle velocity that should be constant, expressed as units of voxels per image, and the sign of v indicates the shifting direction. When positive, the scene is shifted left along the road and vice versa when negative. To generate the optimal final image that contains least noise, the authors propose a model to estimate vehicle velocity, which minimizes noise for a range of tentative values of v, as given by:

$$\hat{v}_{ML} = \arg\min_{v} ||\mathbf{W}_{\text{stack}}\hat{\mathbf{x}}(v) - \mathbf{y}_{\text{stack}}||^2 \tag{3.35}$$

Computational cost increases with the number of iterations required to find v and the number of frames used to estimate the final image. Although the authors demonstrate that this method improves image accuracy, it is not known how this model performs when multiple vehicles are in the monitored area.

The authors mention they record RSS data real-time, but they do not mention if the image was computed real-time, nor do they mention the computation time with their proposed approaches. It is also unknown what their network scan time is.

Localization accuracy

Using the method of removing the negative observations together with the optimized bias parameter β, the authors almost halved the RMSE from 0.385 using the approach in [1] to 0.204. By also integrating their multiple frame combination method, they show, in a series of image estimates, performance is greatly enhanced compared to [1].

The paper does not mention any effect on localization accuracy with regard to vehicle velocity. Furthermore, the researchers have not tested system performance for multiple vehicles to be tracked simultaneously. Since this paper presents the only research so far with regard to roadside surveillance using RTI, the previously mentioned problems are not yet discussed in literature.

Robustness

Anderson et al. mention that weather and atmospheric effects had only a small impact on their RSS measurements at 2.4 GHz. This might be a biased observation, because their tests were conducted under favorable weather and environmental conditions. They do, however, mention that radio signal attenuation at 2.4 GHz is only 0.03 dB/km with a rain rate of 100 mm/hr and less than 0.05 dB/km in fog [20, 36]. With these properties, the authors mention that in their network configuration, the excess attenuation is well within the error bounds in RSS measurement allowed by the ZigBee specification.

Although they do not present any impacts of intrinsic motion on their system, they do show that robustness is increased compared to [1] as demonstrated using Receiver Operating Characteristic (ROC) curves.

4 Proposed RTI System

This dissertation proposes a pragmatic methodology and set-up of an RTI network deployed on a roadside segment that determines occupancy and velocity of multiple family cars in real-time. The research presented in this dissertation is intended to potentially start a bigger research project into reducing the traffic problem described in section 1.1 using Radio Tomographic Imaging technology. The RTI system proposed in this chapter is implemented in the simulation model detailed in chapter 5, of which the results are presented in chapter 6.

The proposed RTI system introduces three new methods, which include a new node spacing approach, a new weight matrix calculation method and a voxel-specific threshold calculation technique. The former two methods have shown to achieve higher system performance than original methods, as demonstrated in chapter 6.

Section 4.1 describes the experimental design of the proposal supported with illustrations and section 4.2 provides a description of the proposed algorithm and methods. The algorithm presents a vehicle detection method using newly proposed voxel-specific threshold calculation. The rest of the algorithm is mainly based on the combination of methods presented in section 3.6. Section 4.3 contains expected system performance and system limitations are described in section 4.4.

4.1 Experimental Design

To measure two cars in the same network traveling at 14 m/s ($\approx$ 50 km/h), maintaining a safe distance of two seconds means the distance between the cars should be 28 m. Taking the length of a car to be 4 m and assuming the cars are at least 14 m (1 second) from the entrance/exit of the network, the network length should span 64 m. As explained later, the total length is rounded off to 66 m. This will require 72 radios, which are 36 nodes on each side, spaced non-linearly along and 3 meters across the road at a height of 0.5 m from the ground. Non-linear node spacing instead of evenly spaced nodes like in previous works was chosen to increase link density at the sub-network edges. Figures 12 and 13 illustrate the proposed design as a top view and front view respectively, where the blue circles represent the nodes. Figure 12 displays three sub-networks which are justified later in this section.

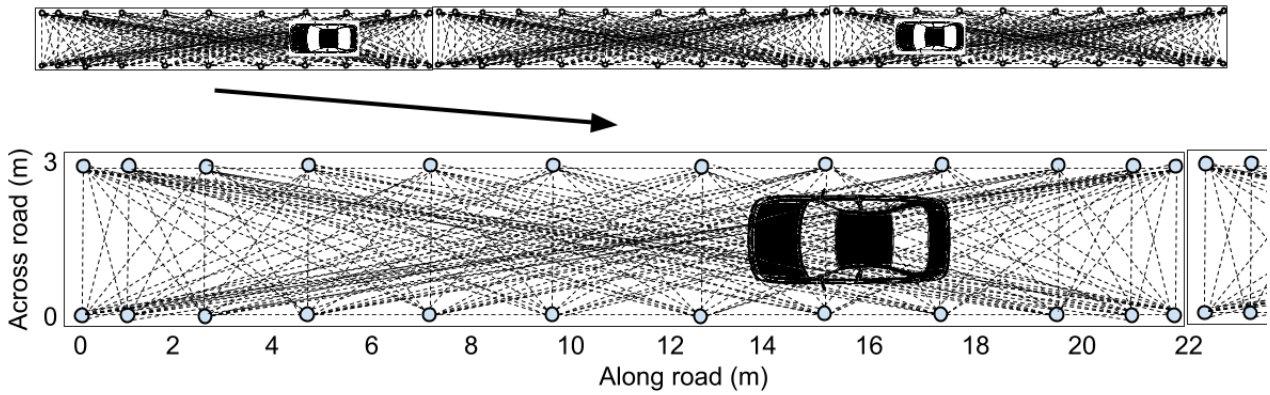

Figure 12 – Top view of roadside surveillance proposal

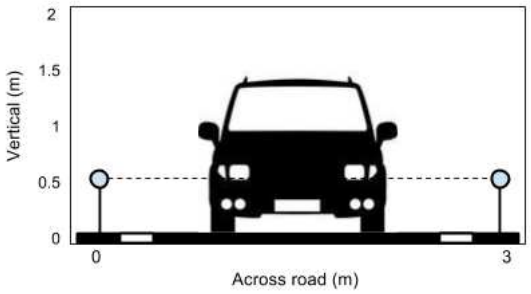

Figure 13 – Front view of roadside surveillance proposal

Network scan frequency should be significantly higher than conventional RTI applications, since vehicles can move considerably faster than people. The best case is where vehicle blurring does not occur, which is when the vehicle does not cross a voxel boundary during one network scan. The relationship between maximum allowable velocity v_{max}, voxel width r_{dist} and network scan frequency f_{scan} is given by [20]:

$$v_{max} = r_{dist} \times f_{scan} \tag{4.1}$$

Network scan frequency is dependent on node transmission time and number of channels used. A trade-off exists between system performance and maximum detectable velocity, where improving localization accuracy would require using a higher amount of frequency channels due to more reliable link-channel pairs being selected, which comes at the cost of network scan frequency and thus maximum detectable velocity.

The average time of a transmission slot (period) per TI CC2531 node is around 3 ms [23], meaning for a WSN with 72 nodes operating on, for instance, four frequency channels, the maximum scan frequency will be ∼1.15 Hz. For a scan frequency of 1.15 Hz and a vehicle that moves 14 m/s (≈ 50 km/h), a voxel width of ∼12 m would be required. Such voxel width would be problematic to estimate velocities each second of vehicles moving slower than 12 m/s. To estimate velocities each second of vehicles moving at, for instance, a minimum of 2.5 m/s (9 km/h), a minimum voxel width of 2.5 m is required. Estimating velocities of up to 14 m/s with a voxel size of 2.5 m, a network scan frequency of at least 6 Hz is necessary. To achieve a 6 Hz scan frequency using 72 nodes operating on four frequency channels, the RTI network may be split up into six sub-networks of 12 nodes each. The use of sub-networks, which was first described in [20], allows each sub-network to be scanned simultaneously. Splitting up into sub-networks, however, comes at a cost of accuracy at the boundary areas, where link density is lower, as can be seen in Figure 12.

To maintain a fairly high accuracy and still making use of multiple channels, the proposed RTI network design contains three simultaneously scanning sub-networks operating on two frequency channels. In this case, each sub-network will contain 24 nodes, meaning a scan frequency of 7 Hz may be achieved, reducing the voxel width to 2 m and thereby making it possible to estimate a minimum velocity of 7.2 km/h. A voxel width of 2 m means only a one-dimensional image can be generated, since the network width is 3 m, which is acceptable for the proposed application, because the vehicle location only needs to be measured on one axis. Using a one-dimensional image also simplifies the tracking problem. With a voxel width of 2 m, the one-dimensional image has a total of 11 voxels per sub-network. Figure 32(b) visualizes the location of the voxels as blue squares in an arbitrary sub-network.

Alippi et al. [8] did not mention the computation time to produce an image estimate. However, Kaltiokallio et al. [10], a slightly less accurate but simpler method than Alippi et al., require an average computation time of 3.4 ms per image estimation based on the method of [23] using a laptop equipped with a 2.67 GHz Intel Core i7-M620 processor and 8.0 GB of RAM memory. The real-time computation consists of

several processes, of which the most intensive is the image estimation of VL multiplications. In the network of Kaltiokallio et al. [23], a total of $L = 435$ links and $V = 3,025$ voxels were used, resulting in 1,315,875 multiplications for the generation of an RTI image during real-time operation.

The number of links for 24 nodes amounts to $L = (N(N-1)/2)^2 = 276$ links with $V = 11$ voxels (voxel width of 2 m for a sub-network length of 22 m) per sub-network, the required number of multiplications per image per sub-network is *only* 3,036 assuming the method of Alippi et al. [8] is used. The total number of multiplications for the image of the complete road segment is therefore 9,108. Using a laptop with similar performance as the one used by Kaltiokallio et al. [23], knowing that the method described in section 4.2 is more complex and assuming the aforementioned network configurations with a network scan time of 144 ms (7 Hz), it is expected that the laptop used for the proposed experiment should be able to estimate images real-time. Figure 18 shows the mean computation time (s) of the simulated RTI image of 11 voxels with and without bias term.

The network design proposes to use the same network hardware with similar configurations as Alippi et al. [8], the only difference being the use of two unique channels per sub-network: $\mathcal{C}_1 = \{11, 20\}$, $\mathcal{C}_2 = \{23, 14\}$, $\mathcal{C}_3 = \{17, 26\}$. Using different frequency channels prevents co-channel interference within the RTI network. The hardware consists of TI CC2531 transceivers equipped with a SWRU120b antenna that operate in the 2.4 GHz ISM band, which are set to transmit at maximum power of 4.5 dBm. The protocol to be used for the RF sensors is the multi-Spin communication protocol, as outlined in section 3.1. Each sub-network has one sink node that receives and transmits real-time RSS data to a receiver radio connected to the laptop, which stores the data of the transmitting nodes in a buffer with all the link measurements.

For this proposal, it is chosen not to use directional antennas, because they increase network scan time considerably. Data transmission and switching direction take 3 ms and 1 ms respectively. Switching and transmitting from six directions will take 23 ms and repeating this for two channels will take 46 ms per node. This is more than seven times longer than using omni-directional antennas, making it unfeasible to use directional antennas for this proposal if image blurring is to be prevented for vehicles traveling at 50 km/h.

The proposed methodology of data acquisition is as follows. Drive one family car at a constant speed of 10 km/h on the RTI covered road segment and use the proposed method outlined in algorithm 1 to estimate occupancy and speed real-time. Repeat this for speeds of 20 km/h, 30 km/h, 40 km/h and 50 km/h. Reiterate the aforementioned procedure with two family cars, always driving at a safe distance of two seconds from each other. All recorded data should be saved to compare system performance for varying vehicle speeds and different amount of measured vehicles. Repeat all tests ten times and calculate an average of the system performance to obtain a more generalized and less noise-corrupted result.

4.2 Radio Tomographic Imaging Algorithm

The roadside surveillance method proposed to be used is outlined in algorithm 1. It is mainly a combination of the outdoor method of Alippi et al. [8] and the improvements from Anderson et al. [20]. A more detailed description of each operation can be found in their respective subsections of section 3.6. A new weight matrix calculation method is introduced, as well as a new voxel-specific threshold calculation technique used for car detection and localization.

The system inputs are obtained during initialization. In this phase, the node and voxel locations need to be obtained in order to calculate the weight matrix $\mathbf{W}$. Node locations are as shown in Figure 12. The new weight matrix calculation method is based on placing a circle with radius 0.7 m at the center of each voxel, which is illustrated in Figure 29. All links that pass through the circle are selected. For the specific

Algorithm 1: Pseudocode for proposed roadside surveillance method

Input: Node and voxel locations
Weight matrix
Reference RSS vector
Fade level
Selected link-channel pairs

Output: Number of cars
Car location
Speed

```
Determine threshold T_v for each voxel
Calculate Tikhonov regularization matrix Π
while (1) do
    At the completion of each network scan:
    Apply online calibration to update reference RSS vector
    Update vector y
    Compute RTI image x̂
    while x̂ has negative observations do
        Set negative voxels of x̂ to zero
        Exclude respective columns of W and D and update Π
        Recompute image x̂
    end
    Apply car detection and speed estimation methods
end
```

network setup proposed in this dissertation, this method selects more useful links for each voxel and thereby leads to improved system performance, as demonstrated in subsection 6.2.1. The reference RSS vector is obtained during offline calibration, which is where the system records data without people or vehicles inside the network. The fade level is dependent on the path loss model and reference RSS vector. To increase accuracy of the fade level, the path loss model parameters are node specific, as presented by Anderson et al. [20]. In other words, each node n is modeled to have its own path loss exponent η_n and transmit reference power P_0^n. Anderson et al. mention that using a node-specific path loss model, the system is more robust against hardware variability factors (including relative antenna orientation between communicating radios) and local environmental differences (like proximity of nodes to dense foliage). The link-channel pair selection method explained in subsection 3.4.3 will select the highest quality anti-fade link-channel pairs that experience least RSS link variance. This filters out unreliable link-channel pairs that experience deep fading, as well as it filters out the longer distance links that have an average RSS close to the sensitivity threshold. Multipath fading is expected to occur due to signal scattering from the road surface and shadowing from vehicles.

The system outputs are the number of detected cars, car location and speed. The former two are related to the number and location of voxels with an intensity larger than a voxel-specific threshold $\mathcal{T}_v$, where $\mathcal{T}_v$ is a newly proposed threshold given by:

$$\mathcal{T}_v = \rho\Big(\sum_{k \in \mathcal{A}_v} F_k\Big)^{\frac{1}{n}} \tag{4.2}$$

where ρ and n are empirically determined parameters, $\mathcal{A}_v$ is the set of selected link-channel pairs k covering voxel v and F_k is the fade level. The basis of this threshold depends on the fact that voxel intensities in general are lower on network edges than in the network center, due to differences in link densities respectively, where more (less) RSS information is available in regions with higher (lower) link densities. Differences in link density along the RTI network can be observed in Figure 12. Therefore, the threshold is dependent on

amount of selected link-channel pairs given by $\mathcal{A}_v$. A lower threshold is thus assigned to the border voxels, whereas the center voxels will be given a higher threshold. Furthermore, the threshold is dependent on fade level, because links with a higher (lower) fade level lead to a higher (lower) voxel intensity, because they experience more (less) signal attenuation. Parameters ρ and n shape the threshold curve and are optimized to obtain optimized system performance. If there are multiple neighboring voxels detected as a car, only the voxel representing the front part of the car is chosen. Vehicle speed is estimated as the number of voxels displaced per second, multiplied by the voxel width.

Parameters α (regularization parameter), ρ and n are found empirically. Since the amount of links is significantly higher than the number of voxels, regularization is theoretically not necessary, but is still included to smoothen the image. Tikhonov regularization is chosen, as it is a more general solution with only one parameter to be optimized, as well as it is shown in Appendix C that it does not differ in system performance compared to regularization with covariance matrix.

The proposed algorithm includes online calibration at the start of each network scan, which helps reduce RSS time-variance due to for example random objects being placed inside the network that should not be detected, or weather effects. This increases the system's robustness, thereby fulfilling one of the requirements mentioned in the goal of this dissertation. Vector $\mathbf{y}$ is updated as described in subsection 3.2.2 and RTI image $\hat{\mathbf{x}}$ is computed using Equation 3.24.

Negative observations are removed from the RTI image using the method detailed in subsection 3.6.3. This method obtains a cleaner image with less visible noise in voxels located around the vehicle, as explained in subsection 6.2.4.

For this proposal, it is chosen not to use the frame combination method from [20], because the method is computationally expensive. Additionally, it is not known whether image accuracy will improve when multiple vehicles are present within the network, as the frame combination method was tested for a single vehicle at a time only.

Furthermore, if the system is used for longer than two hours, the link-channel selection method should be re-applied when no vehicles are detected inside the network as was done by Alippi et al. [8]. This re-calibration procedure allows the system to adjust to any changes in link RSS variance that may have occurred due to time-variant environmental factors, such as weather changes.

4.3 Expected Results

Results from the proposed method are likely to be completely different from the results of papers previously discussed in this dissertation. Not only does the design provide half as many links as in other networks, but the targets to be tracked are vehicles instead of humans, traveling at significantly higher velocities. The only work similar to this proposal is from Anderson et al. [20], who did not publish quantitative results concerning localization accuracy and how it is affected by vehicle velocity, nor system performance for the tracking of multiple vehicles.

Using the proposed simulation model, it is possible to generate some expected results. Figure 14 shows a simulated RTI image of an arbitrary sub-network with a simulated car on voxels 6 and 7, which show to be brighter than the rest of the voxels. The links that pass through the neighboring voxels are also blocked by the vehicle, thereby lowering their RSS, leading to an increased voxel intensity. Neighboring voxels therefore experience correlation between them, which is exactly the voxels' correlation parameter used for the covariance matrix.

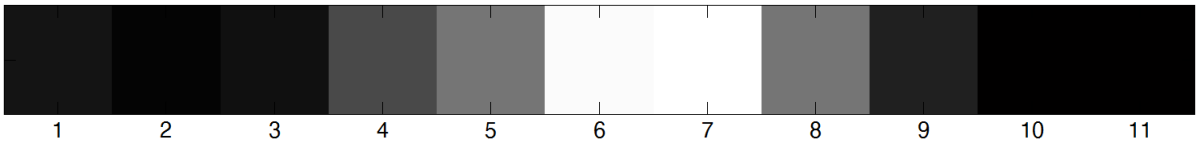

Figure 14 – RTI image with a simulated car on voxels 6 and 7.

The proposed system is expected to be robust against RSS link variance and RSS time-variance, as it makes use of the link-channel selection and online calibration methods [8]. The image is also significantly denoised by the removal of negative observations. Localization accuracy is expected to decrease with increasing targets to be tracked, as investigated by [9] and [37]. This is due to the fact that some links may be attenuated by more than one object. Also, the number of multipath components and attenuation is expected to be larger than in previous studies, due to the increased reflectiveness of metallic objects and size of targets, thereby making multipath interference a bigger problem.

As Martin et al. [30] investigated, there is a trade-off between image resolution and accuracy. They show that the larger the voxel width, the higher the accuracy, due to a larger amount of links covering the pixel. In this proposal, a voxel width of 2 m is used, which is half the size of a vehicle. Alippi et al. [8] uses a voxel width of 0.65 m in a network of 190 links. A voxel width of 2 m for the proposed design should therefore lead to relatively high accuracy, given the 276 links to be used per sub-network.

4.4 Limitations

As opposed to conventional square geometry RTI networks where monitored targets are completely surrounded by radios, the proposed front-back geometry only has radios deployed on two sides. To keep the number of links equal in both geometries, the node density at the border of the front-back geometry will be twice as high as in the square geometry. This leads to a more uneven link density between the network center and edges, which reduces system accuracy at the edges and increases accuracy at the network center. The proposed non-linear node spacing approach is meant to reduce the uneven link densities.

A limitation of using an RTI system with omni-directional antennas operating in cities is co-channel interference with other 2.4 GHz ISM band networks. These networks include public Wi-Fi hotspots, 4G LTE, wireless cameras and Bluetooth devices in vehicles. One method to reduce co-channel interference is using BPSK modulation, but the IEEE 802.15.4 standard only permits frequency bands 800/900 MHz utilizing this scheme, which comes at a cost of localization resolution due to increased wavelength. The performance of an RTI network as a roadside application operating in the 800/900 MHz band will still need to be investigated and is left as a future work. An alternative band could be the relatively interference-free 5 GHz ISM band, which, however, would increase multipath effects as the RSS will experience an increased number of fades. A fade occurs during destructive interference of received multipath components, which happens more often with increased signal frequency. Increased frequency causes more sine wave repetitions within a given path difference, where path difference refers to the difference in path distance between two received multipath signals [38].

5 Simulation Model

Simulating RSS measurements for each link in an RTI system has an important benefit, as it allows an arbitrary network geometry and size to be evaluated before buying and installing components. It also allows network configurations such as multiple frequency channels to be tested, as well as the implementation of techniques that reduce multipath interference and that adapt to dynamic time variant environments.

This Master's dissertation is the first to propose an arbitrary RTI network to be simulated based on a simulated communication channel. The results can also be used for a simple two-node network. The simulation model is implemented in MATLAB and is based on experimental (raw) data that Wilson and Patwari published online to be used by anyone for academic purposes [2]. The researchers used the Texas Instruments (TI) CC2531 transceiver that communicates through the ZigBee protocol [39] in the 2.4 GHz ISM band, so the simulation model is based on the ZigBee protocol and the transceiver's properties. The simulation model is also based on the RSS dynamics outlined in subsection 3.4.2. Furthermore, this chapter shows how the simulated RTI network can be utilized to evaluate the performance of the proposed RTI system, of which the results are shown in chapter 6.

The initialization of the simulation model consists of setting node and voxel locations, calculating link distances, the weight matrix and regularization matrix. Since the initialization procedure does not form the integral part of the simulation model, it is explained in Appendix B. The simulation model is divided in two sections: section 5.1 covers the procedure to obtain RSS data, whereas section 5.2 outlines how RSS data is processed and used to generate new information until a Radio Tomographic Image estimate is generated. The procedures detailed in section 5.1 and subsections 5.2.1 - 5.2.3 only need to be computed once, while subsections 5.2.4 - 5.2.6 are repeated for every network scan. The latter subsections change the originally obtained RSS data in every iteration according to the RSS dynamics, obtain a new RTI image after each RSS vector update and apply the vehicle detection method. The rest of this chapter demonstrates the simulation model validation in section 5.3 and simulation model limitations in section 5.4.

5.1 Obtaining RSS data

The procedure of obtaining RSS data is mainly based on the convolution between a communication channel, which is modeled as a Rician channel, and a transmitted data signal generated by a simulated ZigBee protocol for the 2.4 GHZ ISM band defined by the IEEE 802.15.4 standard [40]. The output of the convolution between the transmitted signal and the Rician channel with AWGN is used to obtain the RSS measurements for each link.

The procedures detailed in this section are repeated for each used frequency channel. In the simulation model, only the number of frequency channels to be used is specified, rather than the defining the specific frequency channel. Although Bocca et al. [3] mention that lower frequency channels measure lower RSS than the higher channels due to varying antenna impedance matching, the difference is negligible and is hence not taken into account in the simulation model.

5.1.1 Transmitted signal

Generating a transmitted data signal consists of several stages. The first is to obtain a data frame that contains the preamble (4 bytes), start frame delimiter (SFD) (1 byte), frame length field and a reserved bit (1 byte) and the variable length data unit [40]. The data unit contains 2 bytes for the node ID and 1 byte per RSS measured from each node (so $N-1$ bytes, where N is number of nodes). Therefore, to represent a frame in the simulation model, a random (uniformly distributed) binary data sequence of length $4+1+1+2+N-1=7+N$ bytes is generated, which is in total $(7+N)\times 8$ bits.

As defined by the IEEE 802.15.4 standard, the ZigBee protocol designed for 2.4 GHz transmissions employs the Direct Sequence Spread Spectrum (DSSS) modulation technique [41] [40]. This method improves receiver sensitivity level and reduces multipath effects. The DSSS technique maps each symbol to a coded pseudorandom (PN) sequence, also referred to as a chip sequence. The concerning ZigBee protocol employs a 16-ary quasi-orthogonal modulation technique (meaning there are 16 PN sequences) with a PN sequence size of 32 chips.

Therefore, the second stage of generating a transmitted data signal consists of converting the bits of stage 1 to 4-bit symbols, after which the symbols are mapped into a 32-chip pseudorandom (PN) sequence using a look-up table defined by the IEEE 802.15.4 standard [40]. Hence a 4-bit input sequence is converted to a 32-bit chip sequence, thus increasing the bit rate by a factor of eight. As the data rate of the original signal is defined to be 250 kb/s [40], the over-the-air bandwidth after spreading becomes 2 MHz.

The third stage modulates the chip sequence with the Offset Quadrature Phase Shift Keying (OQPSK) modulation scheme. In MATLAB, the chip sequence was modulated with a "comm.OQPSKModulator" object using the "step" function. The resulting complex sequence was separated into the In-Phase (real) and Quadrature-Phase (imaginary) chip sequences, after which they were upsampled with a factor 8 (blue line in Figures 15 (a) and (b)) to apply the Half Sine Pulse Shaping Filter described in the fourth stage. Half a chip period was added to the begin and end of the Q- and I-Phase signals respectively to limit the maximum instantaneous phase shift to 90 degrees as required by OQPSK [40] [41].

The fourth and final stage consists of filtering the Q- and I-Phase signals to shape the power spectral density (PSD) from having infinite signal bandwidth (due to high frequency components generated from the sharp transitions) to a finite signal bandwidth. Limiting and minimizing the signal bandwidth allows a given frequency spectrum to be shared among multiple users, it reduces inter symbol interference (ISI) from multipath fading and reduces transmission power [31] [41] [42]. The IEEE 802.15.4 standard employs the Half-Sine pulse shaping filter to shape the signal PSD, as defined by the following equation:

$$p(t)=\begin{cases}\sin(\pi\frac{t}{2T_c}) & 0\le t\le 2T_c\\ 0 & \text{otherwise}\end{cases} \tag{5.1}$$

Where $2T_c$ is the chip period. Since the signal was upsampled with factor 8, each chip period now lasts 8 samples. Therefore, in MATLAB, the Half-Sine filter was defined as:

$$\text{p = sin(pi*t/t(end));} \tag{5.2}$$

$$\text{t = 0:nsamp;} \tag{5.3}$$

where nsamp is the upsampling factor of 8. The Q- and I-phase chip sequences of the third stage are then individually shaped to a half-sine using the "conv" MATLAB function, which convolves the two vectors. The outputs of the convolution are then combined into a complex signal that is transmitted onto the communication channel. The half-sine shaped signals are combined by multiplying the Q-Phase half-sine signal with "i"

and adding it to the I-Phase half-sine signal. Figures 15 (a) and (b) show the In-Phase and Quadrature-Phase half-sine filtered chip sequences respectively. Figures 15 (c) and (d) show the PSD of the upsampled and half-sine filtered chip sequences respectively. As can be observed in (d), the bandwidth is shaped in the sense that more power is present in the frequency band -1 to 1 MHz (hence a 2 MHz signal bandwidth) as compared to the PSD in (c).

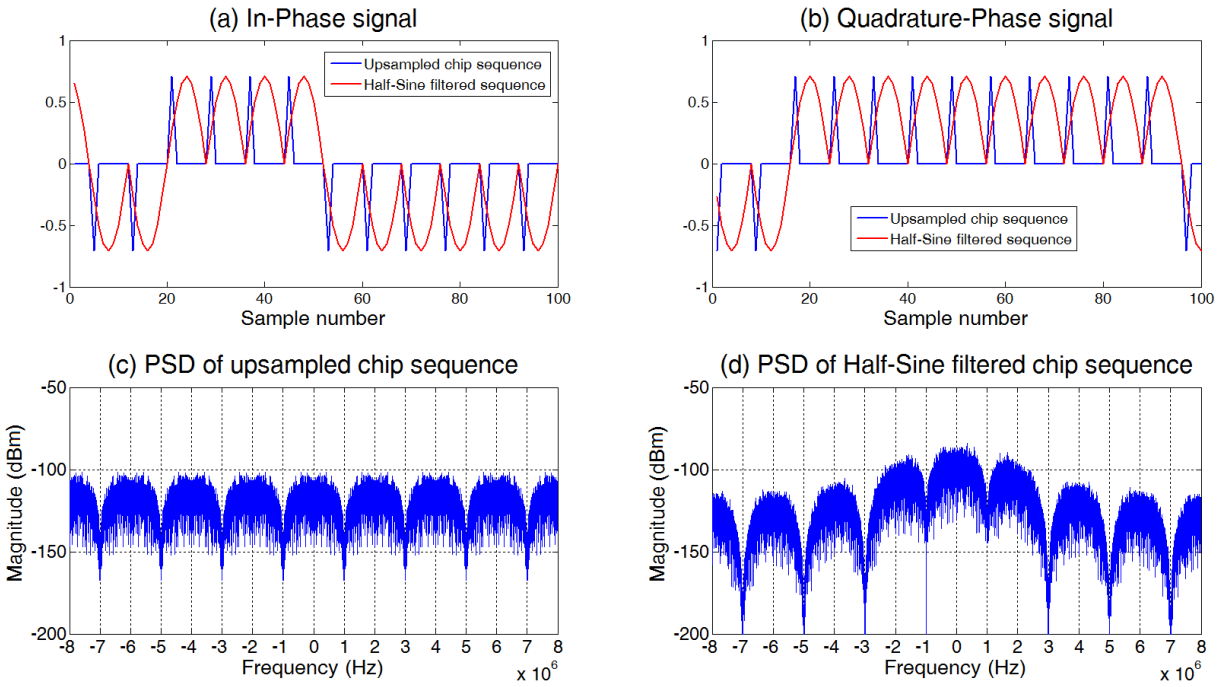

Figure 15 – Graphs generated in MATLAB comparing 100 samples of upsampled chip sequence to half-sine filtered signal of the (a) In-Phase and (b) Quadrature-Phase signals. Figures (c) and (d) show the Power Spectral Density (PSD) of the upsampled chip sequence and half-sine filtered signal respectively.

5.1.2 Communication Channel

To model the communication channel, a Rician channel was used, because most of the communication links are assumed to be LOS, whereas a Rayleigh channel would be used for non-LOS cases [31]. The Rician channel was set-up using the "ricianchan" function of MATLAB. This function requires five parameters, which are the input signal sample time (s), maximum Doppler shift (Hz), Rician K-factor, path delays (s) and average path gains (dB). Since the radios are not moving with respect to each other, there is no Doppler shift. The Rician K-factor determines the shape of the Rician distribution. The smaller the value K, which means the dominant path decreases in amplitude, the more the distribution is positively (right) skewed, resulting in a distribution more similar to Rayleigh [31]. It was observed, however, that factor K did not influence in the results for the implemented simulation model, so it was left as an arbitrary value (K = 1). The other three parameters are discussed below.

The signal sample time is dependent on the chip rate and upsampling factor. Since the chip rate is 2MHz, the chip period becomes 500 ns. With an upsampling factor of 8, the signal sample time is 62.5 ns.

The number of multipaths is related to the signal bandwidth and coherence bandwidth. Since the coherence bandwidth is not known a priori, the number of received paths per signal for this simulation model was

chosen to be 3. Therefore, the vectors representing path delays and path gains have three elements. The first path delay refers to the first arriving path and is set to zero [43]. The subsequent path delays were set to be random (uniformly distributed) multiples of the sample time of 62.5e-9 s, where the second path always arrives earlier than the third path.

The path gains are related to the log-distance path loss model parameters found for the "empty area" data published by Wilson et al. The parameters found were $P_0 = -50.82$ dBm at $d_0 = 1$ m and $\eta = 1.57$ as can be observed in Figure 7a. However, for reasons as explained in section 5.3, η was set to 1.37 instead of 1.57. Before path gains were calculated, a random (uniformly distributed) set of links from the total set of links were chosen to be reliable, whereas the rest was regarded unreliable. The percentage of reliable links (with positive fade level) was found to be around 55% from the data of Wilson et al., so this same percentage was used in the simulation model. For every link, an initial path gain for the first path was calculated using the log-distance path-loss model. If that link was detected to be reliable, a gain offset of 5 dB was added to the initial path gain to give it positive fade level (anti-fade), whereas for unreliable links 5 dB was subtracted from the initial path gain to make sure it experiences negative fade level (deep fade). See section 5.3 about why a 5 dB gain offset was chosen. For the subsequent path gains, 2 dB was subtracted from the preceding path gain and a random (uniformly distributed) decimal value in the interval [-1,1] was added to it. In the end, a path gain matrix was obtained with three path gains per link in the network.

After the "ricianchan" object had been assigned its required parameters, it was filtered with the transmitted signal using the "filter" function. Additive White Gaussian Noise was then added to the resulting signal with a Signal to Noise Ratio (SNR) of 20 dB. It was not known what the most appropriate value of SNR is, but it was observed that the value of the SNR did not make a significant impact on the calculated RSS.

Figure 25a shows the simulated RSS vs. log-distance and its log-distance path loss model with the same network setup as Wilson et al. [1].

5.1.3 Received Signal Strength Measurements

The technique employed to calculate the Received Signal Strength Intensity (RSSI) in the TI CC2531 is detailed in a User's Guide published by Texas Instruments that describes the modules and peripherals of the TI CC253x transceiver [44]. As outlined in the referred document and described by the IEEE 802.15.4 standard [40], the RSSI value is obtained by averaging the received power over the first eight symbols following the SFD directly after the demodulator. The demodulator retrieves the over-the-air data from the received signal. The block diagram of a demodulator of a IEEE 802.15.4 2.4 GHz transceiver [4] is shown in Figure 16.

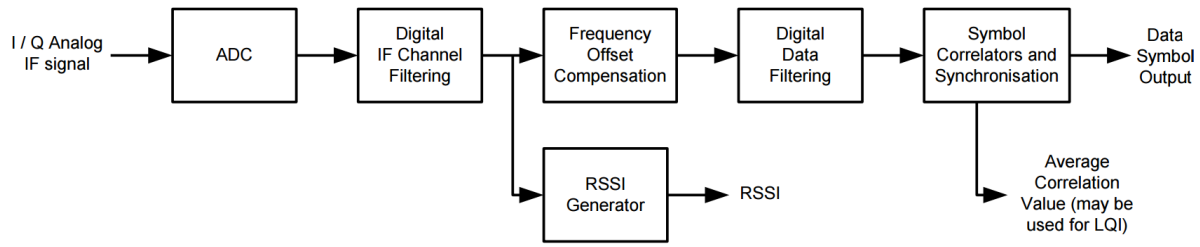

Figure 16 – Block diagram of a IEEE 802.15.4 2.4 GHz transceiver [4].

As can be observed, first the analog received signal is converted to a digital signal, after which it is shifted to an intermediate frequency for further processing. After this stage, the RSSI is calculated according to Equation (5.4). Since in the simulation model the received signal is discrete and shifting from an intermediate to a baseband frequency is not applicable, the RSSI was calculated directly from the received signal without pre-processing.

Therefore, to calculate the simulated RSS (dBm) data in MATLAB, the dBm value of the mean of the absolute value of the received signal was computed, where the latter two were calculated using the functions "mean" and "abs" respectively. The RSS value $r_{l,c}$ for link l and channel c in Equation (5.4) will return the value in dBm, because the input path gains to the rician channel were also in dBm scale.

$$r_{l,c}(\text{dBm}) = 10\log_{10}\left(\frac{\frac{1}{S}\sum_{s=1}^{S}|\text{rx}(s)|^2}{1\text{ mW}}\right) = 20\log_{10}\left(\frac{\frac{1}{S}\sum_{s=1}^{S}|\text{rx}(s)|}{1\text{ mV}}\right) \tag{5.4}$$

where S is the length of the received signal, which is $(7 + N) \times 8$ bits, and rx is the received signal. The first equality of Equation (5.4) assumes received power inside the brackets by squaring the received signal, whereas the second equality assumes voltage inside the brackets. The second equality is implemented in the simulation model.

This procedure is repeated for every link in the network. Note that in the simulation model the RSS is calculated for the complete received frame, hence not the first eight symbols following the SFD, as it is expected not to make a difference in the obtained RSS.

5.2 Processing RSS data

After obtaining the vectors and matrices during initialization (see Appendix B) and the simulated RSS data, it was processed and used to obtain new information until a Radio Tomographic Image estimate was generated. The subsequent steps include computing fade level, selecting link-channel pairs, calculating thresholds and simulating a vehicle.

5.2.1 Fade level

After RSS data had been simulated and obtained, it was used to calculate the fade level of all links of each channel. Path loss parameters η and P_0 were calculated using all simulated RSS data and were used to obtain the log-distance path loss model, which also required the link length vector obtained during initialization. Subsequently, fade level of all links on all channels were computed using Equation (3.8).

Figure 25b shows the fade level of the simulated RSS with the same network setup as Wilson et al. [1].

5.2.2 Link-channel pair selection

The link-channel pair selection method was implemented as described in section 3.4.3. First, the set of link-channel pairs with positive fade level was obtained. A second set of link-channel pairs was retrieved that contained RSS measurements higher than the grey region. Thirdly, the intersection between the previously found sets was obtained.

The fourth stage was more challenging to compute in the simulation model. As the fourth stage is dependent on RSS variance $\sigma^2_{l,c}$ of link l on channel c, many realizations would have to be computed to calculate such variance. As each realization takes about 23 seconds to compute, a different solution was found to obtain RSS variance to reduce simulation time. The experimental data of Wilson et al. [2] was used to find a relationship between fade level and variance. This relationship is displayed in Figure 17.

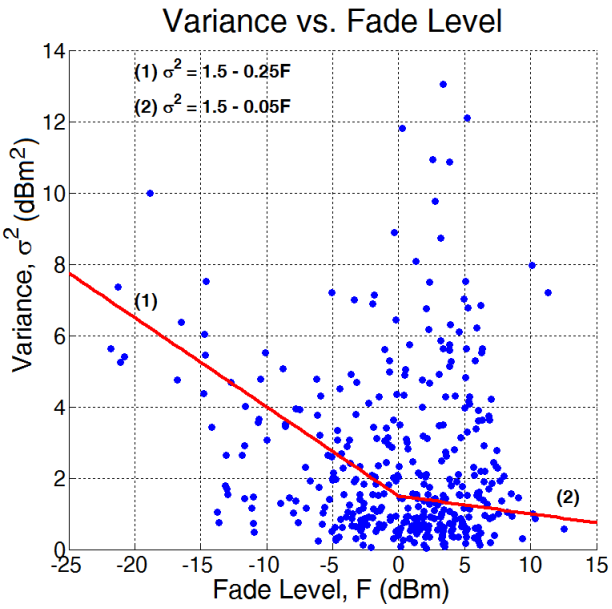

Figure 17 – RSS variance as a function of fade level. The displayed data was processed from experimental data of Wilson et al. in the empty area. Curves (1) and (2) in the negative and positive fade level sections correspond to the formulae displayed in the top left side of the graph.

As can be observed, two curves were found as a best fit that describe the relationship between variance of links and channels experiencing negative and positive fade levels. These curves were found by ignoring some of the data in the higher variance levels on the positive fade level side. This data was regarded as outliers, because they do not explain the behavior as described in section 3.4.2. Curve (1) in the negative fade level section corresponds to $\sigma^2_{l,c}(\text{dBm}^2) = 1.5 - 0.25F_{l,c}$ and curve (2) describes variance of links and channels in positive fade level by $\sigma^2_{l,c}(\text{dBm}^2) = 1.5 - 0.05F_{l,c}$.

These functions were used to calculate the final stage of the link-channel selection method, as given by Equations (3.28) and (3.29). Equation (3.29) obtains the weights that are used to select the most reliable channel of previously selected link-channel pairs to obtain set $\mathcal{L}$ using Equation (3.28).

5.2.3 Threshold

The threshold $\mathcal{T}_v$ was calculated as given by Equation (4.2) and is voxel-specific, where the threshold for each voxel v is dependent on fade level of selected link-channels that represent the concerning voxel. Parameters ρ and n were found empirically to yield the best performance and are given in subsection 6.2.4.

5.2.4 Vehicle simulation

The procedure described in this subsection was repeated for every network scan, as it changes the RSS data according to the behavior described in subsection 3.4.2. Therefore, the simulation model only needs to compute RSS data as outlined in section 5.1 once.

In the simulation model, a vehicle is assumed to be four meters in length, which corresponds to the length of two voxels that are a size 2x2 m^2 each. Therefore, a vehicle is simulated to occupy two neighboring voxels. In the first stage, all the links chosen during the weight matrix calculation that represent the voxels occupied by a vehicle are found.

In the second stage, all the links in the network are assigned a RSS variance according to the Equations presented in 5.2.2. The link-channel pairs that experience positive fade level are assigned a variance according to formula (2) given in Figure 17, whereas the rest of the link-channel pairs (in negative fade level) experience a RSS variance according to formula (1). A new RSS measurement $r_{l,c}$ is calculated for each link on each channel by inserting the square root of the previously determined RSS variance (giving standard deviation) into the following line of MATLAB code:

$$r_{l,c} = \bar{r}_{l,c} + \sigma_{l,c} \times \text{randn} \tag{5.5}$$

where $\bar{r}_{l,c}$ is the RSS data calculated in 5.1.3 and randn is a MATLAB function that generates a zero mean, unit variance random Gaussian variable. This represents the RSS noise, which is assumed AWGN by Anderson et al. [20] and is represented by $\mathbf{n}$ in Equation (3.1). Although Alippi et al. [8] do not mention specifically that the RSS variance refers to the noise variance, it is assumed in this dissertation to be the noise variance.

The third stage is where the vehicle is simulated. As shown in subsection 3.4.2, when a target is present on the RSS link in anti-fade, the RSS drops with around 5 dB, while RSS links in deep fade do not tend to be affected by it due to their high RSS variance. Unfortunately, this is the only link blocking behavior knowledge available, meaning it was not possible to develop or use an already existing model to determine the signal attenuation of an arbitrary object size that blocks links of arbitrary length and fade level. Therefore, a fixed signal attenuation value was used to subtract from $r_{l,c}$ for every anti-fade link-channel pair that is part of the set found in the first stage of the described vehicle simulation procedure. The fixed signal attenuation value is set to 8 dB, as it is assumed that vehicles attenuate signals more than humans do (around 5 dB), but not significantly more.

5.2.5 Obtaining a Radio Tomographic Image estimate

After the RSS vector is updated $r_{l,c}$, the change in RSS vector $y_{l,c}$ is calculated using Equation (3.10). As also noted with the concerning Equation, all the elements that do not belong to the set of selected link-channel pairs are set to zero. The radio tomographic imaging procedure described in this subsection was tested using the available experimental data of Wilson et al. [2], and the same RTI image was obtained as they demonstrated in their paper [1]. Therefore, the imaging generation part of the simulation model was validated, but was not included in this dissertation as it would not create additional value of showing the same image.

The radio tomographic image vector $\mathbf{x}$ may be generated in two ways as is explained in Appendix B. If the user desires a more generalized solution, Tikhonov regularization as in Equation (3.20) is employed, whereas a more specific image result is estimated using regularization with a covariance matrix C_x as given by Equation (3.31). Tikhonov regularization requires less computational cost and less parameters than using a covariance matrix, but may generate a less optimal solution than using a covariance matrix. For the simulation of the proposed RTI system, it was chosen to employ general regularization for reasons explained in subsection 6.2.4.

Depending on the computational resources and necessities of the user, a bias term may or may not be added to generate the RTI image estimate. The former is computed by Equation (3.17) and the latter by Equation (3.30). As can be observed in Figure 18, the average time to compute an RTI image with and without bias term is 2.9 μs and 1.8 μs respectively, meaning the latter method is approximately a factor 1.6 faster. The computations were performed on a laptop with an Intel Core i7-4500U CPU @ 1.80 GHz (4 CPUs) and 12 GB RAM.

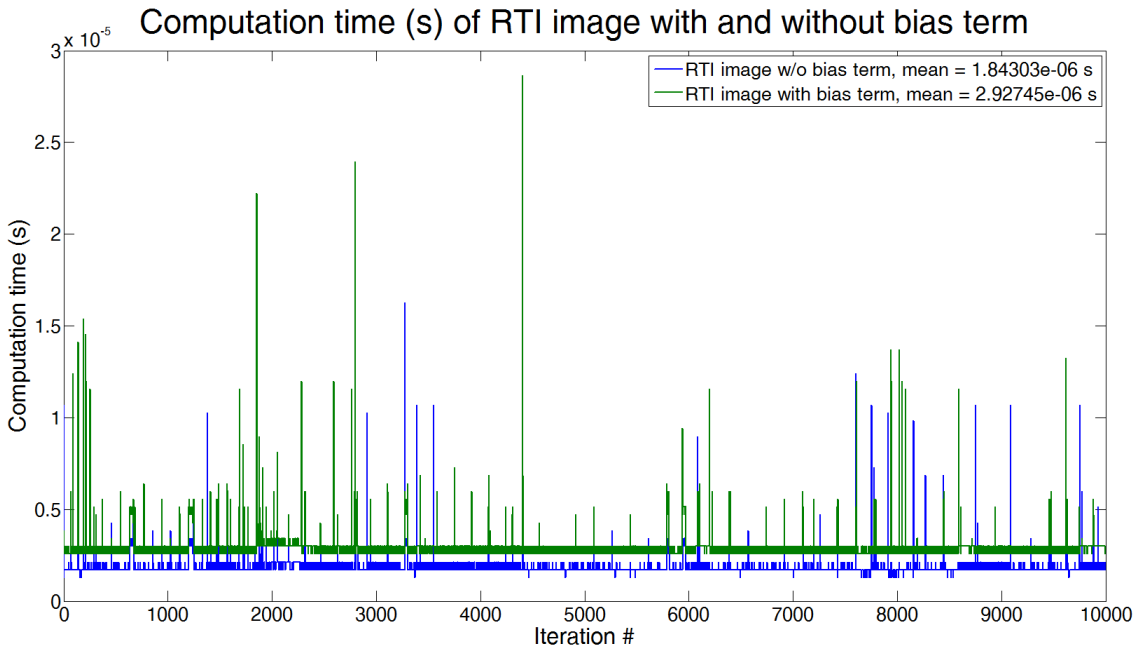

Figure 18 – Graph that compares the computation time (s) between the generation of an RTI image with and without bias term of 10,000 iterations.

The effect of the bias term is to shift the voxel intensities to a higher or lower level. For the simulation of the proposed RTI system, it was found that using a bias term was not necessary to optimize performance, so it was decided to omit the bias term and thereby keep image computation simpler.

Removing negative observations in RTI image $\mathbf{x}$ as proposed by Anderson et al. [20] was implemented in the following way. Any negative voxel intensities in $\mathbf{x}$ were set to zero and the columns of $\mathbf{W}$ corresponding to the negative voxel intensities were omitted. When general regularization is used, the corresponding columns of $\mathbf{D}_X$ and $\mathbf{D}_Y$ (in a 2D image) were omitted, whereas in specific regularization, both corresponding rows and columns of C_x were removed. The matrices used for regularization are now reduced in dimensions that update only the positive voxel intensities. The image $\mathbf{x}$ was therefore recomputed, updating only the positive voxel intensities. This procedure was iterated until the RTI image did not contain negative voxel intensities anymore, which was never more than one or two iterations during the simulation of the proposed RTI system.

If the RTI image is two-dimensional, the image vector $\mathbf{x}$ is converted to a two-dimensional matrix, where it is important to specify the image dimensions to identify which vector elements belong to which position in the image.

5.2.6 Vehicle detection and speed estimation

The vehicle detection method mainly consists of comparing the voxel intensities to the pre-calculated voxel-specific threshold $\mathcal{T}_v$. Every voxel that has an intensity higher than the threshold is considered to be occupied by a vehicle. If two neighboring voxels are detected as a vehicle, only the voxel representing the front part of the vehicle is considered, so the direction of traffic will need to be known a priori.

Speed estimation cannot be fairly implemented in the simulation model, as it depends on the delay being chosen between consecutive iterations. In real life scenarios, vehicle speed would be calculated as the number of voxels displaced by the vehicle per second, multiplied by voxel size.

5.3 Simulation Validation

To validate the simulation model, the simulated RSS data is compared to the experimental data published by Wilson et al. [1], using the same network setup and configurations. The experimental data was recorded with no targets in the measurement area (empty area).

The network of Wilson et al. [1] consists of 28 nodes, hence the frame length to simulate the network of Wilson et al. [1] is $(7 + 28) \times 8 = 280$ bits (see section 5.1 about frame length calculation).

In the ideal case, the probability distribution of the received signal amplitude voltage of every link length is compared to each other, which, in a LOS environment, follows a Rician distribution [31]. To obtain the amplitude voltages, the RSS data in dBm is converted to voltage using the following conversion:

$$r_{l,c}(\mathrm{V}) = 10^{\frac{r_{l,c}(\mathrm{dBm})-30}{20}} \tag{5.6}$$

The experimental data consists of 378 links (28 nodes), where each communication link contains about 270 measurements. The most common link length is 6.5 m (21.2 feet), of which there are 20 LOS links as displayed in Figure 19a. The 20 LOS links (red lines) are shown on top of the RTI network setup deployed by Wilson et al., which contains 28 nodes and two trees inside the measurement environment. Four links that originally crossed through the trees have been left out to leave only LOS links. The RSS data gathered on the 20 LOS links was combined in one vector to obtain a probability distribution. This gave 8,431 measurements to be exact and its histogram with 100 bins is shown in Figure 19b.

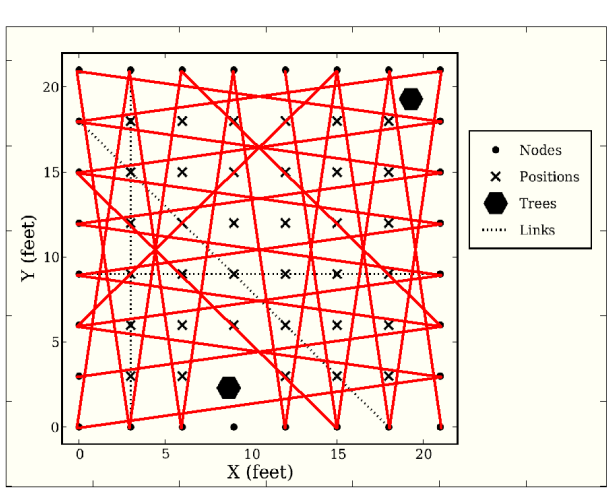

(a)

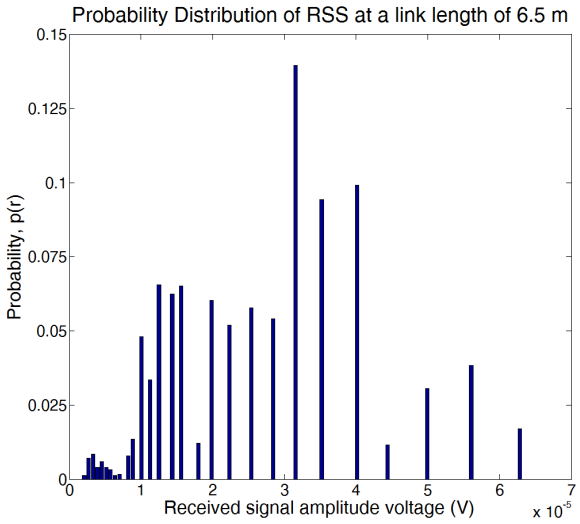

(b)

Figure 19 – Probability distribution of RSS at link length 6.5 m.

As can be observed, it is difficult to associate this histogram with a Rician distribution. The most probable cause is the lack of sufficient measurements for this particular link length. This means that comparing RSS data for each link length will not offer a reliable validation metric.

Therefore, to validate the simulation model, all of the data of all 378 links of the experimental RSS data was combined giving 100,992 measurements. These 378 links also include the links that pass through the trees, as it is a relatively cumbersome and manual task to find and remove them. In addition, as explained later, the histogram is approximated by a distribution, and because it is an approximation, it is expected that excluding the several blocked links will have a negligible effect on the approximated distribution.

All the RSS data was converted from dBm to voltage and shown in one probability distribution. The distribution will not be Rician anymore, because data from different link lengths is combined. The application "dfittool" in MATLAB was used to find a distribution that most closely fits the histogram generated from the RSS data, where the number of bins used was 32. The application supports 20 distributions, ranging from Beta to Rician to Weibull. Choosing a distribution was done manually and the distribution with highest log likelihood value (calculated by the application) representing the histogram of the experimental RSS data was chosen to represent the histogram of both experimental and simulated RSS data. It was found that the Burr Type XII probability distribution most closely fits the histogram of the experimental RSS data, which are both shown in Figure 20.

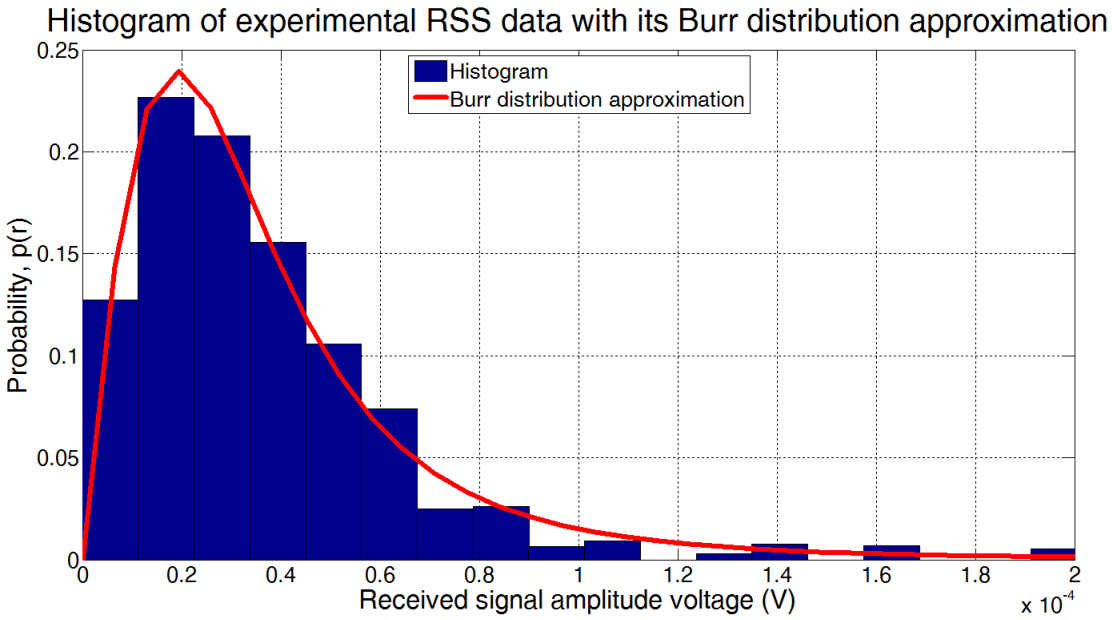

Figure 20 – Histogram of experimental RSS data with its Burr distribution approximation.

The formula of the Burr Type XII probability density function is given by

$$f(x|\alpha,c,k) = \frac{\frac{kc}{\alpha}\left(\frac{x}{\alpha}\right)^{c-1}}{\left(1+\left(\frac{x}{\alpha}\right)^{c}\right)^{k+1}}, x>0, \alpha>0, c>0, k>0. \tag{5.7}$$

where c and k are the shaping parameters and α is the scale parameter that is related to the voltage level at the maximum probability [45].

The next stage in validation was to generate 20 realizations of simulated RSS data, where each realization contained 100,926 RSS elements, similar to the amount of experimental data available (100,992 measurements). One realization consisted of obtaining one RSS measurement for each of the 378 links using the method described in section 5.1. The rest of the measurements were simulated by repeating the procedure of the second stage of subsection 5.2.4. All RSS data was converted from dBm to voltage and for each realization, a respective Burr probability distribution was calculated, which were then averaged to obtain a more generalized result that is less prone to variations caused by the Rician channel object. The resulting distribution was validated to the probability distribution of the experimental RSS data according to the Mean Square Error (MSE) metric of the probability values, which is a commonly used performance evaluation metric to obtain distance between measurements.

This validation procedure was repeated for four different values of three simulation parameters to optimize the fit of the simulation distribution to the experimental distribution. The parameters that were optimized were the path-loss model parameters P_0, η and the gain offset, which all affect the simulated path gains described and hence the shape of the respective RSS probability distribution. Figure 21 presents the optimized simulation distribution with a MSE of 0.17×10^{-4} using parameter values $P_0 = -50.82$ dBm, $\eta = 1.37$ and gain offset = 5 dB. Observe that parameter P_0 is the same as the experimental data shown in Figure 7a, but parameter η was reduced from 1.57 to 1.37. Figures 22 - 24 demonstrate the effect of parameters η, P_0 and gain offset respectively on the Burr distributions representing the histogram of the averaged (over 20 realizations) simulated RSS data and Table 1 contains the MSE of the demonstrated distributions with respect to the reference (experimental) distribution. Note that the optimized result presented in this dissertation is likely not the best possible result, since only the described parameter values were evaluated. As it takes around 23 seconds to compute one realization, and therefore around 30 minutes to generate one graph, it was left outside the scope of this research to find the best possible result.

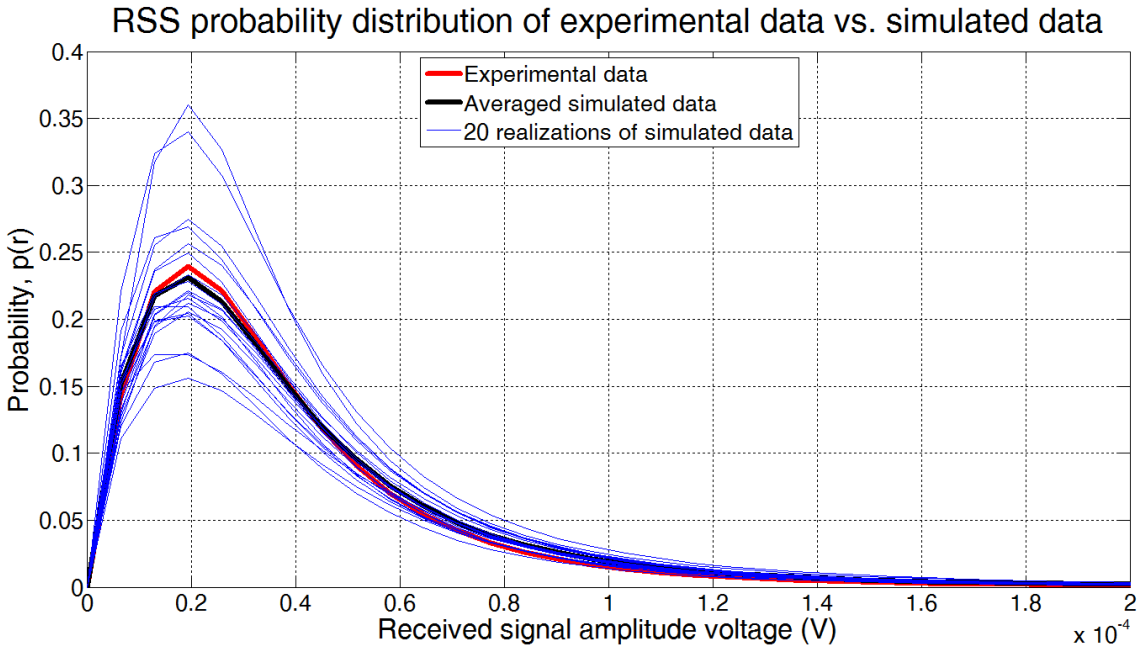

Figure 21 – Burr probability distribution approximation of histogram of experimental RSS data (red line) from Wilson et al. [2] and simulated data, with path-loss parameters $P_0 = -50.82$, $\eta = 1.37$ and gain offset = 5 dB. MSE = 0.17×10^{-4}.

Table 1 – Table comparing MSE between Burr probability distribution approximation of histogram of experimental RSS data and averaged simulated RSS data with different values for P_0, η and gain offset

η	MSE ($\times 10^{-4}$)		P_0 (dBm)	MSE ($\times 10^{-4}$)		Gain offset (dB)	MSE ($\times 10^{-4}$)
1.17	5.65		-48.82	5.18		1	7.07
1.37	1.85		-49.82	2.46		3	1.82
1.57	4.01		-50.82	1.27		5	0.32
1.77	11.00		-51.82	4.36		7	5.48

As can be observed in Figure 22, the amplitude, width and α (scale parameter of the Burr distribution that is related to the voltage level at the maximum probability [45]) of the distribution are proportional to path loss exponent η. The values of η were chosen according to the path loss exponent obtained from the experimental data, which was $\eta = 1.57$. Parameters P_0 and gain offset were fixed at -50.82 dBm (same as experimental data) and 3 dB respectively. Changing the parameter η affects the inclination of RSS versus log-distance, or the rate at which path loss increases with distance, as explained in subsection 3.2.2. The higher the value of η, the more the links are attenuated, thus the lower the α, the higher the amplitude and the smaller the width of the distribution. Table 1 shows that the lowest MSE value of MSE $= 1.85 \times 10^{-4}$ belongs to the distribution of $\eta = 1.37$, and consequently this value was chosen to keep fixed when comparing the effect of parameter P_0 in Figure 23.

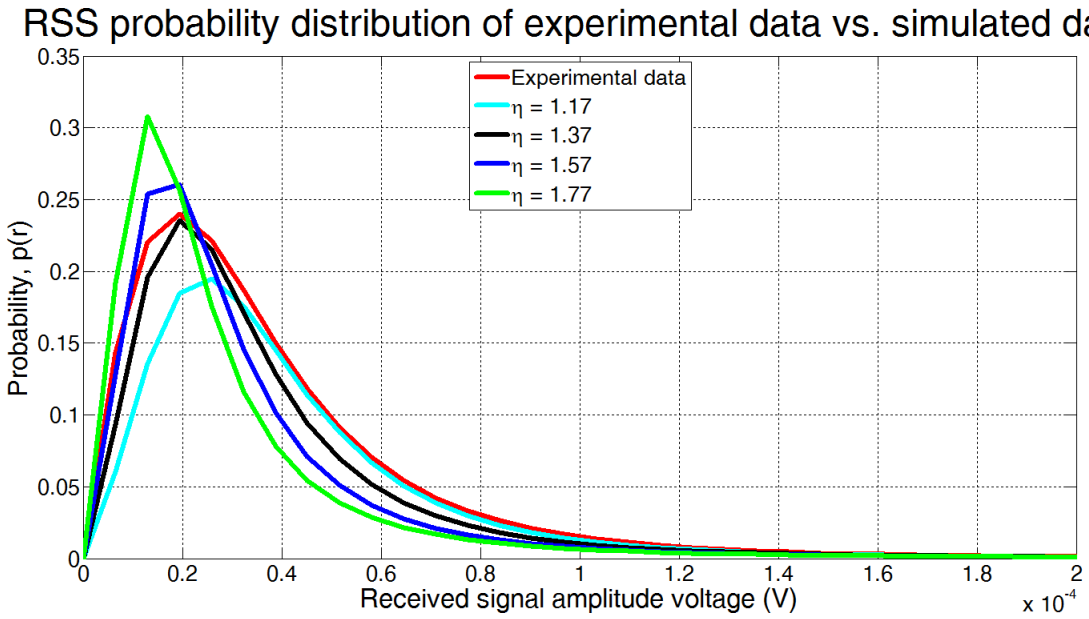

Figure 22 – Burr probability distribution approximation of histogram of experimental RSS data (red line) and averaged simulated data with $\eta = 1.17$, $\eta = 1.37$, $\eta = 1.57$, $\eta = 1.77$, $P_0 = -50.82$ dBm and gain offset = 3 dB. The averaged simulated data was the result of the average of the burr distributions generated by 20 realizations.

Figure 23 demonstrates the effect of parameter P_0 on the shape of the distribution curve. The values of the fixed parameters are $\eta = 1.37$ and gain offset = 3 dB. Changing parameter P_0 dislocates the RSS versus log-distance graph in the vertical direction. Thus the lower the P_0, the more the attenuation of each link, therefore the lower the value of α and the smaller the curve width. The curve that generated the lowest MSE of 1.27×10^{-4} is at $P_0 = -50.82$ dBm. Theoretically, this MSE value should be the same as the lowest MSE value of Figure 22, because the same parameters were used, but is instead slightly different due to the partially random Rician channel called in every realization. The comparison made with respect to variable P_0 thus concludes that $P_0 = -50.82$ dBm yields the best fit, which is the same as the experimental P_0.

The third and last parameter that was optimized was the gain offset, as can be observed in Figure 24, where fixed parameters were $\eta = 1.37$ and $P_0 = -50.82$ dBm. Changing the gain offset affects the spread of RSS with respect to the path loss model: the higher the gain offset the larger the spread of RSS. The main effect the gain offset has on the distribution is the curve width, where increasing the gain offset results in a larger curve width, due to RSS data points being more spread out. Table 1 indicates that a gain offset of 5

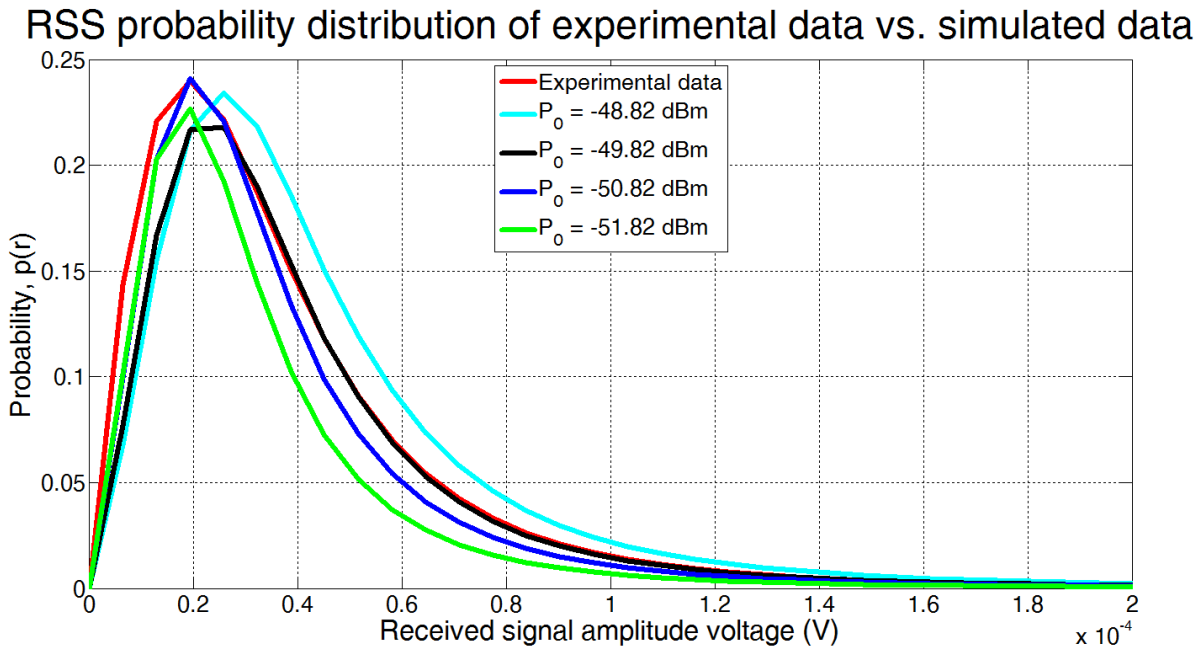

Figure 23 – Burr probability distribution approximation of histogram of experimental RSS data (red line) and averaged simulated data with $P_0 = -48.82$ dBm, $P_0 = -49.82$ dBm, $P_0 = -50.82$ dBm, $P_0 = -51.82$ dBm, $\eta = 1.37$ and gain offset = 3 dB. The averaged simulated data was the result of the average of the burr distributions generated by 20 realizations.

dB yields the lowest MSE value of 0.32×10^{-4}. This gain offset makes sense, because when observing Figure 7b that illustrates the fade level of experimental data, the average of the positive and negative fade levels is approximately 5 dB from the path loss model.

Therefore, the optimized parameters are $\eta = 1.37$, $P_0 = -50.82$ dBm and gain offset = 5 dB. Note that only a rough optimization was made. It was decided not to make a more fine-tuned optimization due to the long computation time per 20 realizations of roughly 8 minutes. The optimized parameter values were chosen to simulate the proposed RTI system.

Figures 25a and 25b show the simulated RSS vs. log-distance and fade level respectively with the optimized parameters representing the same network setup as Wilson et al. [1]. As can be observed, parameters P_0 and η are not exactly the same as the optimized parameters, due to the partial randomness of the Rician channel. Furthermore, the maximum and minimum fade levels approximately correspond to the experimental fade levels illustrated in Figure 7b.

5.4 Limitations

One of the main limitations of the proposed simulation model is the procedure for simulating a vehicle. Currently, for every link that passes through the vehicle, a signal attenuation of 8 dB was defined. This value was based on the signal attenuation induced by a person described by Bocca et al. [3], but does not take into account factors such as object type or size that obstructs the link, effect dependent on fade level, nor the amount of link length effectively passing through the object.

Although it would have been interesting to implement the node specific path-loss model introduced by Alippi et al. [8], as it was shown to greatly improve performance, it was not possible to include it in the

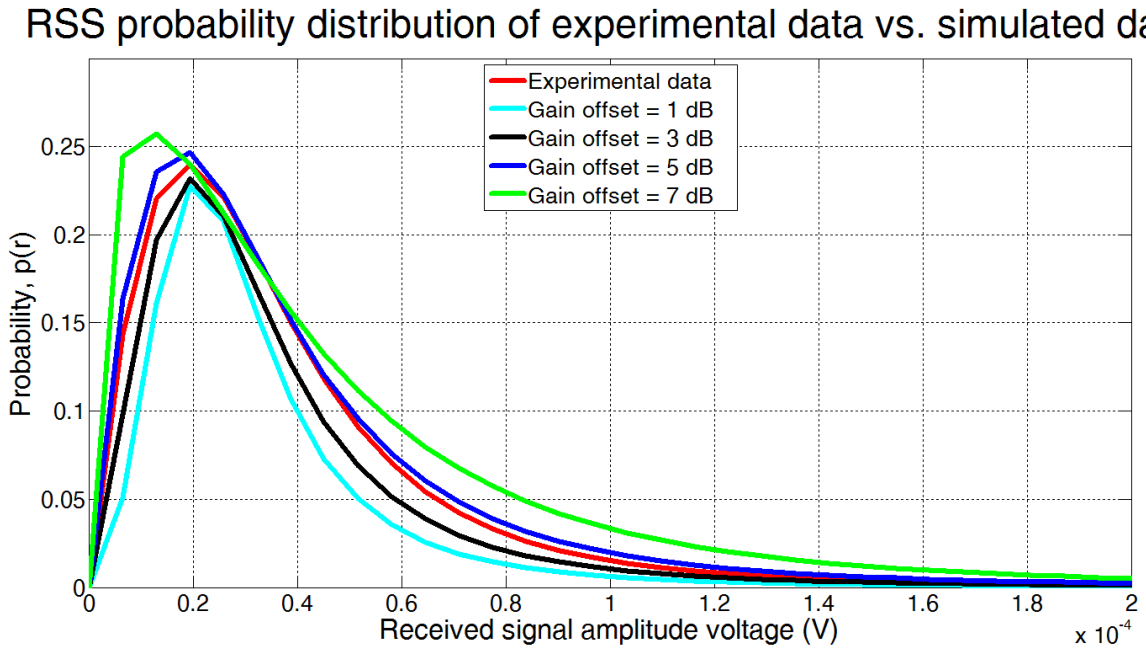

Figure 24 – Burr probability distribution approximation of histogram of experimental RSS data (red line) and averaged simulated data with gain offset = 1 dB, 3 dB, 5 dB and 7 dB, $P_0 = -50.82$ dBm and $\eta = 1.37$. The averaged simulated data was the result of the average of the burr distributions generated by 20 realizations.

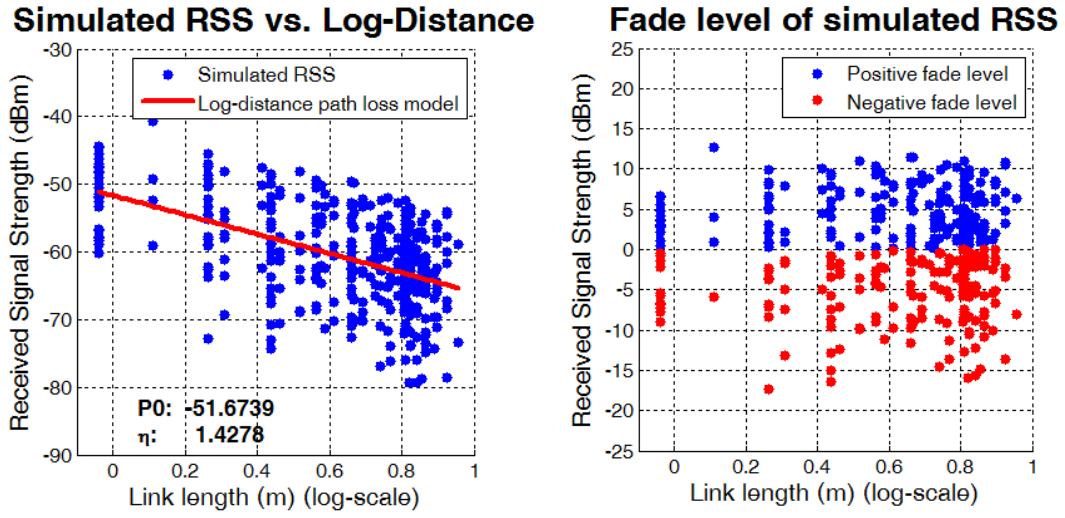

(a) (b)

Figure 25 – Figure (a) shows simulated RSS (dBm) data versus log-distance (m) and its log-distance path-loss model with corresponding parameters P_0 and η displayed in the graph. Figure (b) shows the fade level as calculated using Equation (3.8), where the blue and red data points are the positive and negative fade levels respectively, shown to more easily distinguish between the two levels.

simulations. The node specific path-loss model is a result of specific relative antenna orientation between T-R nodes and proximity of nodes to neighboring objects, which are factors that would over-complicate the

simulations if they were to be included, as they are specific to each deployment environment. Moreover, including this model would lose generalization of the simulations, which is against the goal of simulating an arbitrary RTI network.

Currently, the simulation model does not support the online calibration method, because RSS time variance has not been included since it was decided not to be an important part to demonstrate the performance of the proposed RTI system using the newly developed simulation model.

6 Results

The results presented in this chapter demonstrate the implementation of the proposed RTI network described in chapter 4 using the simulation model outlined in chapter 5. In section 6.1, the optimized result is shown for the implementation of one and two vehicles. How this result was optimized is covered in section 6.2.

6.1 Optimized result

This section shows the simulation results of one and two vehicles present inside an arbitrary sub-network in subsections 6.1.1 and 6.1.2 respectively.

6.1.1 Single vehicle

Simulation results of a single family sized car of 4 meters located on each voxel from 1 to 11 in an arbitrary sub-network is shown in Figures 26 and 27, displayed as a line plot and image respectively.

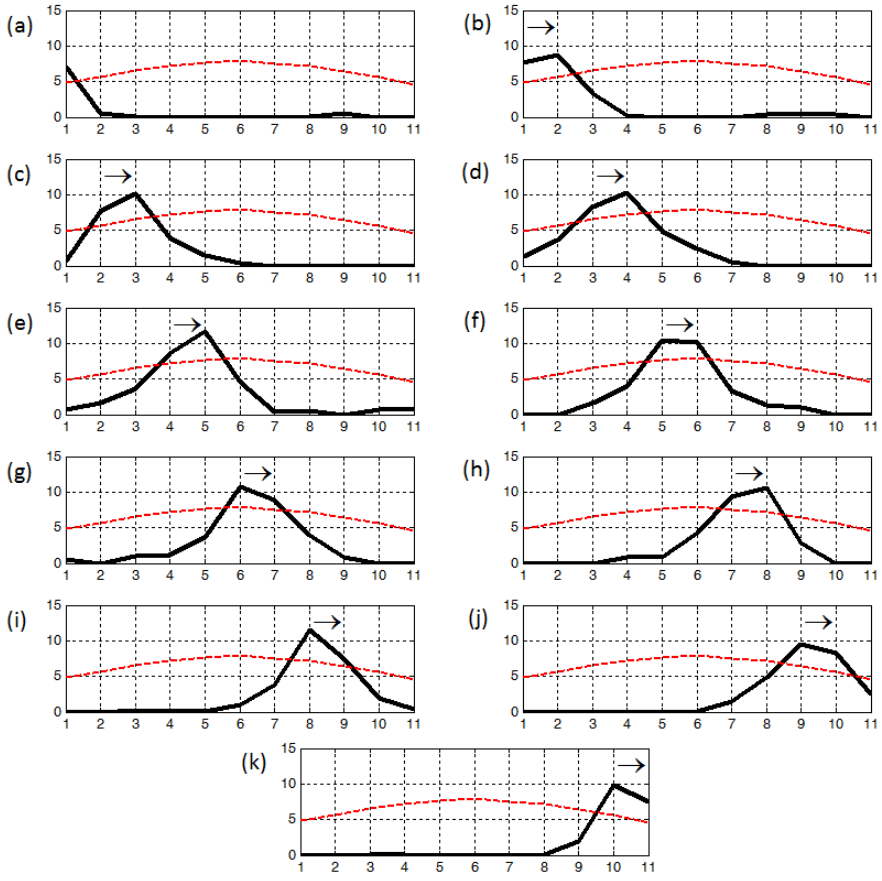

Figure 26 – Simulated car (black curve) on voxels 1 to 11 (x-axis) shown in figures (a) to (k) respectively, where the y-axis represents voxel intensity. The red dashed curve is the voxel-specific threshold and the arrow indicates the two respective voxels occupied by the car and the flow direction.

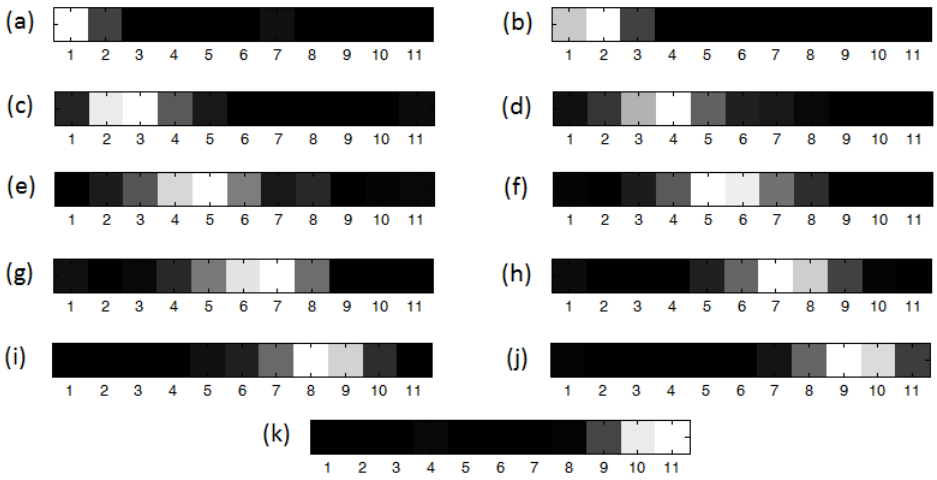

Figure 27 – Simulated car shown as the two brightest neighboring voxels in each image on voxels 1 to 11 shown in figures (a) to (k) respectively. This is the RTI image respresentation of Figure 26

As can be observed in Figure 26, using the validated simulation model, a car passing through an RTI network as a roadside surveillance application can clearly be located. A vehicle is detected on any voxel with voxel intensity higher than the threshold, which, purely by observation, is accurate in each of 11 cases. The voxel intensities of the car located on the edge of the network is roughly speaking lower than when it is located in the network's center. This is due to link density, which is lower on the edge than in the center and the threshold value is adjusted to this characteristic accordingly, showing a higher value in the middle than on the sides.

Another observation is that the image is still minimally affected by noise, due to RSS link variance and multipath effects, as seen on the voxels further away from the current vehicle location. Most of the noise has been filtered out by using the link-channel pair selection method, which is demonstrated in subsection 6.2.3. The simulation model therefore does not show an ideal case with zero noise, but rather a more realistic representation of a practical implementation where noise is minimized.

Figure 27 shows the RTI image version of Figure 26, where the two brightest neighboring voxels in each image (a) to (k) represent the location of a vehicle. This is the final output of the RTI technology. Though the vehicle detection method used in this dissertation is based on a simple threshold, digital image processing techniques can be applied to Figure 27 as an alternative, and potentially more effective technique of vehicle detection and localization. Such techniques may be blob detection or other Artificial Intelligence or Reinforcement Learning methods.

6.1.2 Two vehicles

This dissertation proposes the detection and localization of multiple vehicles using the RTI network setup described in chapter 4. The implementation of this proposal with two vehicles is simulated and presented in Figure 28.

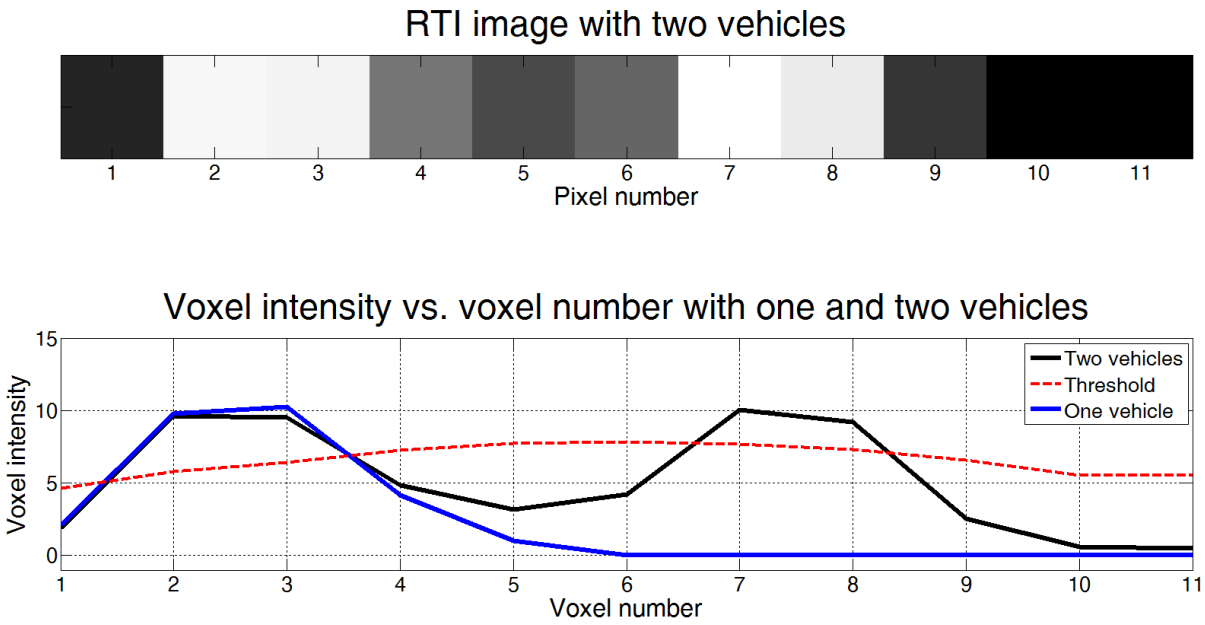

Figure 28 – Figure showing the RTI image with two vehicles located on voxels [2,3] and [7,8] respectively and its corresponding representation as a line plot (black curve). The effect of two vehicles in the network can be compared to the effect that one vehicle has by the blue curve. The red dashed curve is the threshold.

The RTI image with two vehicles clearly shows two vehicles located on voxels 2 and 3, and 7 and 8 respectively. The line plot also indicates that the highest intensities are measured on the mentioned voxels and are all higher than the threshold. This means that in theory, according to the simulation model and the assumptions made in it, the system would successfully detect the location of both vehicles in the given scenario. However, system performance is expected to be lower compared to one vehicle, because some links are blocked by two vehicles at the same time, thereby reducing the reliability of the respective links.

This phenomenon of links being blocked by two vehicles can be observed in Figure 28. The intensity on voxel 5 is higher with two vehicles than one vehicle (blue curve). This is due to the fact that the links representing this voxel pass through both vehicles, thereby experiencing more signal attenuation and hence resulting in a higher voxel intensity than if those links would pass through only one vehicle. This phenomenon in a practical situation is thus also reflected in the simulation model.

6.2 Optimizing the result

The results presented in section 6.1 are optimized with respect to a few parameters and the implementation of two newly proposed techniques and one existing technique. The parameters and techniques used for the optimized result are summarized in subsection 6.2.4.

6.2.1 New Weight Matrix Calculation and its effect

One of the newly proposed techniques is the link selection procedure for the weight matrix. The original method consists of using an ellipse that represents the area measured by one link, where the larger the ellipse width, the higher the chance that it covers more voxels (dependent on voxel size). This is a logical and effective method for 2-dimensional images with a relatively high pixel density.

For this proposal, however, a 1-dimensional image is used with relatively few voxels of a large size (2x2 m). The newly proposed link selection procedure for the weight matrix uses a circle located in the center of each voxel and selects each link that passes through the circle. Therefore, the larger the radius of the circle, the higher the chance that more links will be selected. The radius set for the simulation is 0.7 m. The reason why this method is more effective for the given situation, is that it prevents the selection of links that provide relatively little information about a given voxel. This effect is shown in Figure 29, where both methods are compared to each other. The selected links on voxels 1 and 10 are displayed by the red links, the unselected links are shown as gray lines, the voxels are shown as blue squares and the selection circle is dark green. The number of selected links is shown on top of the corresponding voxel.

As can be observed, using the original method, 4 links are selected for the first voxel and 16 for the tenth voxel. The new method selects 4 and 12 links for the first and tenth voxel respectively. The 4 extra links selected by the original method for voxel 10 are those that provide relatively little information about that voxel, as they are longer links and pass through more voxels. Reducing the ellipse width would remove those links. However, this would also remove two of the longer links of the first voxel, which is undesired, because those to-be-removed links pass almost half of their length through that voxel, meaning they are valuable links that represent that voxel. The new method thus allows the more valuable links to be chosen for the given scenario.

Vehicle detection performance between the two selection methods is presented in Figure 30. Performance was measured by calculating the average detection accuracy (%) of 50 repetitions on voxels 1 to 11. The output of the performance computation is a 1 or 0 for each repetition, where a 1 is that the location of the front half of the car (so only the rightmost voxel of two detected voxels) is correctly identified and 0 otherwise. In each repetition, the RSS vector is updated by the procedure described in subsection 5.2.4. This process is one simulation realization, which was repeated 20 times and averaged to obtain a more general result.

The performance results indicate that on most voxels, a higher accuracy of between 90% and 100% is achieved between voxels 1 and 9 using the newly proposed weight matrix calculation method (WMCM). This already demonstrates that the proposed RTI system will work near perfect according to the simulation model. Especially a higher accuracy of approximately 100% is yielded on voxels 7 and 8, which are close to the center of the network, due to invaluable links being left out. The edge of the network shows similar performance between the methods of around 65% to 70%, because in both cases only 4 links were selected.

Therefore, the newly proposed WMCM was chosen to be used to obtain the optimal result and was employed for the evaluation of the rest of the techniques described in this section.

Figure 31 shows an RTI image and corresponding line plot of a vehicle on voxels 9 and 10, which is the location that gives worst performance as observed from Figure 29. The reason for this low performance is

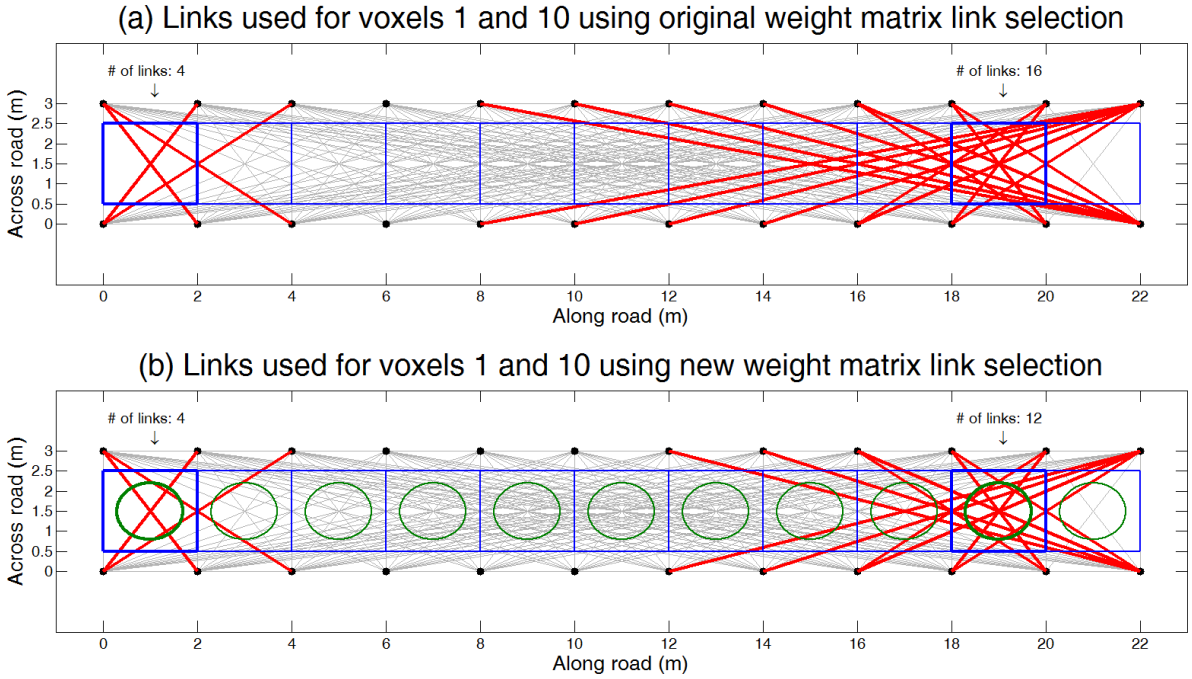

Figure 29 – Comparing which links and the amount of links are selected for voxels 1 and 10 using the (a) original and (b) newly proposed weight matrix calculation method (WMCM). The red and gray lines are the selected and unselected links respectively, the blue squares are the voxels and the selection circles with radius of 0.7 m are in green.

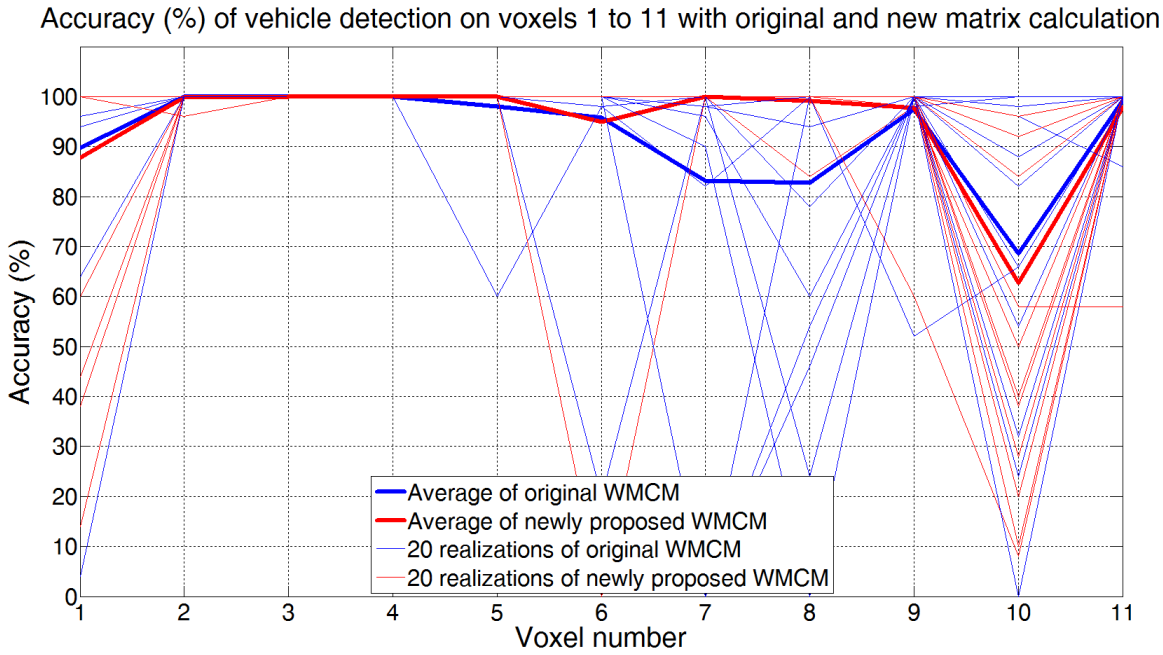

Figure 30 – Accuracy (%) of vehicle detection on voxels 1 to 11 with original and new matrix calculation. The data presented are 20 realizations of the original and newly proposed Weight Matrix Calculation Method (WMCM) and their average.

that the voxel intensity on voxel 11 is close to the threshold value. When it is higher than the threshold, the system detected the vehicle location on voxel 11 instead of voxel 10, thereby introducing a False Positive (FP).

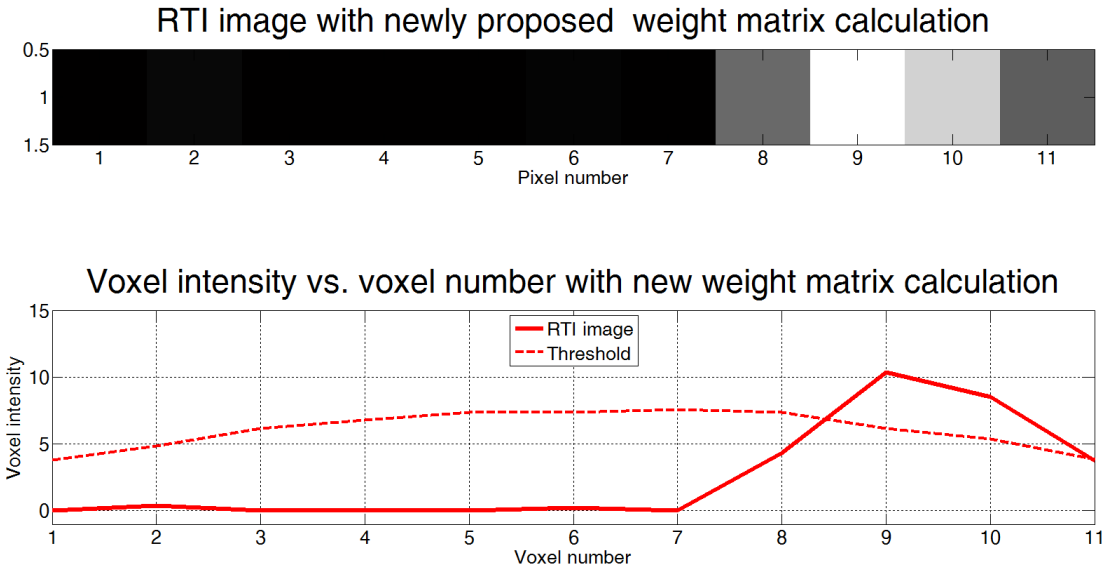

Figure 31 – RTI image with vehicle located on voxels 9 and 10 and corresponding line plot using newly proposed weight matrix calculation method.

6.2.2 Effect of node placement

The second newly proposed technique that improves system performance is the non-linear spacing between nodes to increase link density at the network edges. A higher link density in a given area means more information is available about that area, theoretically leading to improved accuracy. Since link density is significantly higher in the network center than in the edges, the proposal is to increase the spacing between middle nodes and consequently reduce spacing between edge nodes. Figure 32 illustrates the number of selected links for voxels 1 and 10 using evenly and unevenly spaced nodes.

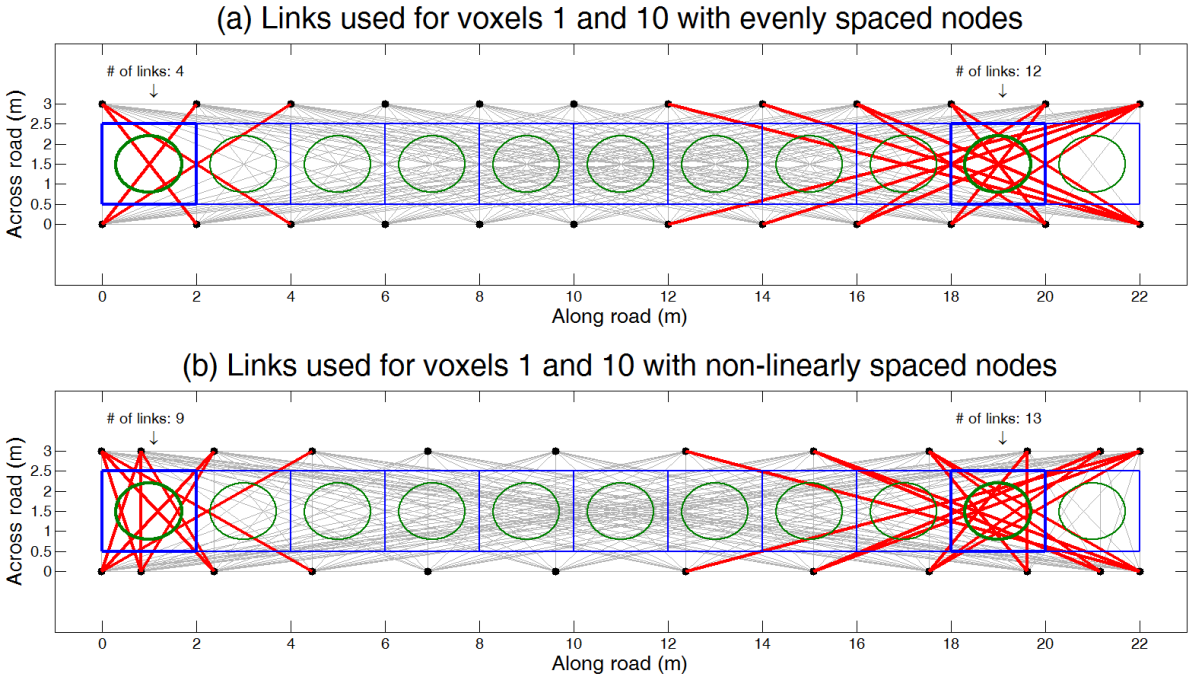

Figure 32 – Comparing which links and the amount of links are selected for voxels 1 and 10 using (a) evenly and (b) unevenly spaced nodes. The red and gray lines are the selected and unselected links respectively, the blue squares are the voxels and the selection circles with radius of 0.7 m are in green.

As shown, the number of selected links is more than doubled at the outer voxels (voxels 1 and 11, where 11 is symmetrical to 1), from 4 to 9 links. This comes at the cost of less reliable links in the center, due to increased node spacing, but should theoretically not lead to significantly reduced system performance.

The effect of node spacing on system performance is illustrated in Figure 33, which was calculated using the same performance measuring procedure as in subsection 6.2.1. As can be observed, using unevenly spaced nodes leads to higher vehicle detection accuracy, especially on the network edges. This follows exactly the theory of how link density affects performance. System accuracy now is roughly speaking the same in the edges as in the center of the network, yielding a near perfect accuracy of between 95 - 100% in the performed experiments.

Consequently, the network setup of the optimized result in section 6.1 has nodes spaced unevenly in the manner presented in this subsection. Uneven node spacing was also employed to evaluate the technique described in the next subsection.

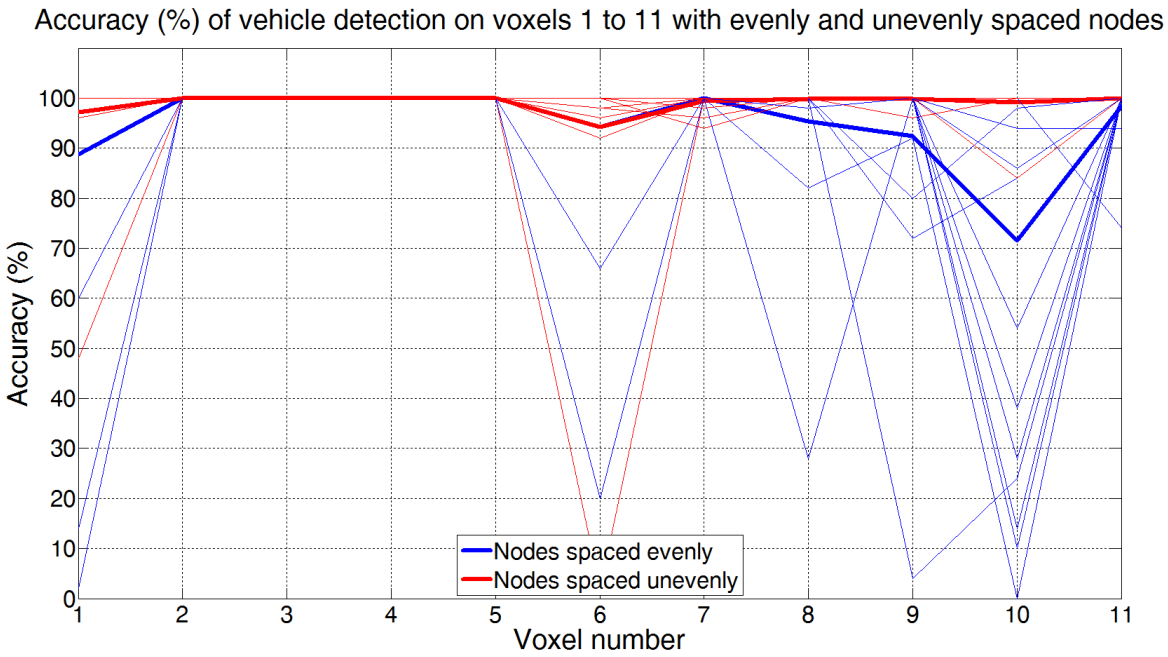

Figure 33 – Accuracy (%) of vehicle detection on voxels 1 to 11 with evenly and unevenly spaced nodes. The data presented are 20 realizations of the evenly and unevenly spaced nodes (thinner blue and red curves respectively) and their average.

6.2.3 Effect of link-channel selection method

According to literature, the more frequency channels that are employed, the higher the quality (with least RSS variance) of link-channel pairs that are selected. This effect is tested in the simulation model and the results are presented in Figure 34, which shows system performance calculated using the same procedure as outlined in subsection 6.2.1.

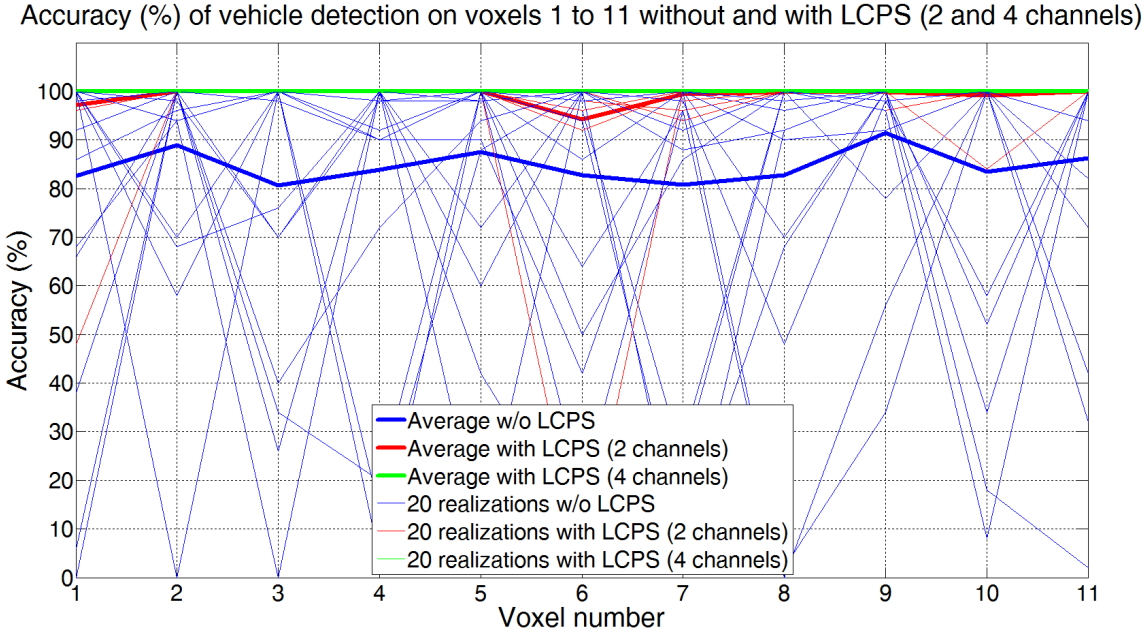

Figure 34 – Accuracy (%) of vehicle detection on voxels 1 to 11 without link-channel pair selection (LCPS) and with LCPS (2 and 4 channels). The data presented are 20 realizations of the concerning variables and their average.

In the performed simulation experiments, the RTI system demonstrates to be accurate using only one frequency channel without link-channel pair selection (LCPS), with an accuracy of between 80% and 90% for all voxels. However, adding a second channel and using the LCPS method, accuracy for all voxels is significantly improved to between 95% and 100%. A perfect performance of 100% for all voxels is achieved using four channels and the LCPS method. It is likely that using three channels would also yield perfect performance, but was not tested for this simulation comparison. The performance result seen in Figure 34 can be regarded as another type of simulation model validation, because the demonstrated performance difference between number of channels used confirms what is being described in literature.

The proposed RTI system contains the use of two frequency channels due to reasons described in section 4.1, meaning that in theory, it performs close to perfect and almost as well as using more than two channels.

Figure 35 illustrates two RTI images that compare the result of using two and four channels respectively, with their line plots displayed accordingly. The line plot also shows the result of using only one channel without LCPS. As expected, the curves with LCPS are very similar to each other due to their similar system performance, while the curve without LCPS is visibly different. Not only is the RTI curve different, but also its threshold, which is irregular and seemingly more random as opposed to the other curved and smooth thresholds. This irregular threshold is likely to have been the cause of the reduced vehicle detection accuracy. The reason for the irregular threshold is that all fade levels are included in the calculation, both positive and negative.

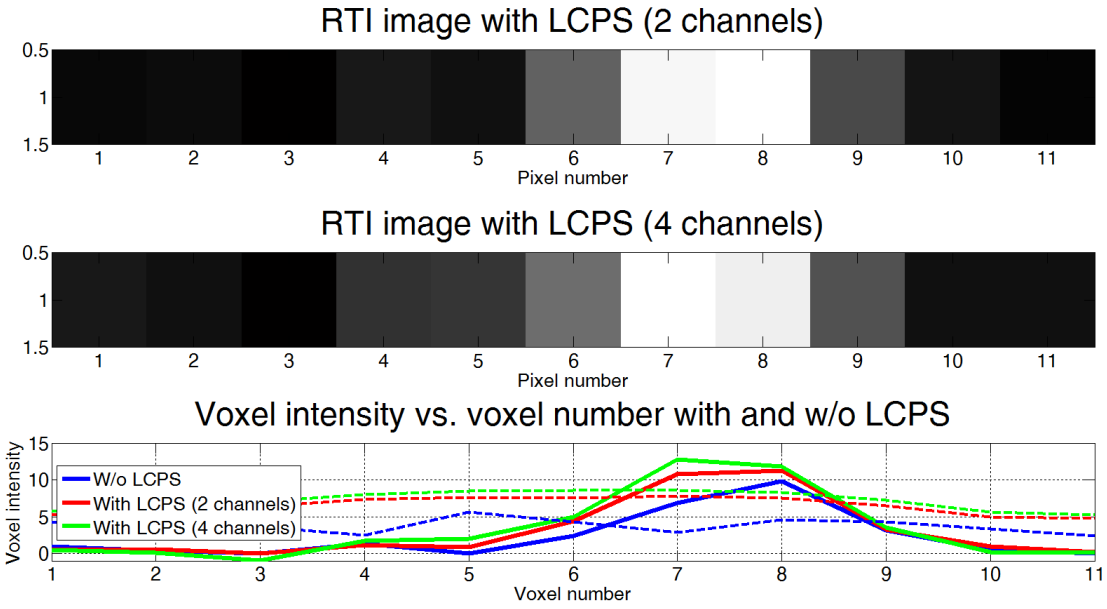

Figure 35 – RTI image with vehicle located on voxels 7 and 8 and corresponding line plot without link-channel pair selection (LCPS) and with LCPS (2 and 4 channels). The dashed curves are the thresholds with their color corresponding to the RTI image they represent.

6.2.4 Techniques and parameters used for optimized result

The parameters for the threshold ρ and n were optimized empirically, by trying out different values and observing which values yield the best vehicle detection performance. Note that the optimized values may not be the true best, but merely an approximation, as it is a cumbersome task to optimize parameters manually. A continuation of this research may employ optimization techniques that search for the optimized parameter values automatically. The values found for the concerning parameters are $\rho = 2$ and $n = 4$.

The results described in this section conclude that the following techniques are used to achieve the optimized result, as also described in chapter 4: new weight matrix calculation method that selects links based on the radius r of the circle in each voxel, unevenly spaced nodes and two channels with LCPS (which was already chosen in the proposed RTI system).

Furthermore, the algorithm for the proposed RTI system includes two other techniques: regularization type and removing negative observations in the RTI image, which were evaluated in Appendix C. As demonstrated in the respective appendix, regularization type and removing negative observations did not have a notable impact on performance. It was therefore decided to employ generalized regularization, as it only requires the optimization of one parameter instead of three. The technique to remove negative image observations was also employed, as the RTI image shows to be less affected by noise in voxels around the vehicle, thereby achieving a cleaner image. Table 2 summarizes the parameter values used to obtain the optimized result.

Table 2 – Parameters and their corresponding values and description used for the optimized result.

Parameter	Value	Description
ρ	2	Threshold weighting parameter
n	4	Threshold power parameter
r	0.7	Link selection circle radius
α	0.1	Generalized regularization parameter

7 Conclusion

This dissertation proposes the implementation of a relatively new wireless communication technology, referred to as Radio Tomographic Imaging, to a roadside surveillance environment. The desired outcome of this dissertation is the continuation of the presented research, with as end goal hoping to deploy the RTI network as a (complementary) urban vehicle traffic monitoring structure integrated into an Intelligent Transport System.

The core of this dissertation proposes a design and methodology for the estimation of occupancy and velocity of one and two vehicles on a single lane road segment traveling at speeds from 10 km/h up to 50 km/h using a Radio Tomographic Imaging network. The proposal is the first to present an RTI network that is split into multiple sub-networks to achieve a network scan frequency fast enough to prevent blurring of vehicles traveling at higher velocities.

The proposed roadside surveillance method is mainly based on two recent works by Alippi et al. [8] and Anderson et al. [20], together with three newly implemented techniques, namely a new weight matrix calculation method, a new node spacing setup and a new voxel-specific threshold calculation approach used for car detection, localization and speed estimation. Simulation results presented in chapter 6 have demonstrated that the two former newly introduced methods improved system performance considerably compared to current approaches. This is mainly due to the unique network setup used, which only has nodes positioned on two opposing sides of the network, causing low link density at the network edges and therefore reduced performance in the respective areas. The new WMCM is effective in the given scenario, as voxel size is relatively large with regard to network dimensions, and improves performance by selecting more valuable links in each voxel.

The proposed RTI system fulfills the requirements listed in the goal in section 1.4. The first requirement is that the system should be fast enough to measure real-time occupancy and velocity of multiple vehicles moving at 50 km/h, which is enabled by the combination of three sub-networks deployed in series, each 22 meters long, employing two frequency channels in the 2.4 GHz ISM band and scanning at 7 Hz. The resulting RTI image has a voxel size of 2 m. Real-time operation is possible, since Figure 18 indicates that RTI image generation takes 1.8 μs on a relatively high-performance laptop, which is a procedure that is iterated two to three times by the negative image observation removal procedure. The total computation time is hence significantly less than one scanning period of 142 ms (1/7 Hz).

The second and third requirements are that the RTI system should be robust to RSS variance of the links and to RSS time-variance. Two techniques are employed to reduce this issue, namely the link-channel pair selection method and online calibration respectively. The LCPS method obtains the highest quality link-channel pairs, which selects only the link-channels in anti-fade with least RSS variance. The node-specific path loss model allows more accurate calculation of fade level per node, making the LCPS method more reliable. Online calibration reduces the RSS time-variance issue, as it updates the reference RSS at the start of each network scan.

The simulation model presented in chapter 5 is a relatively complete model of an RTI network. It generates RSS measurements based on the ZigBee IEEE 802.15.4 protocol, which are processed using the RTI techniques covered in chapter 3. The advantage of the developed simulation model over previous models is that it implements physical layer properties by simulating a communication channel, thereby making the simulated RSS data more realistic. Moreover, it allows the specification of an RTI network from the ground

up, including node positions, network size and geometry and RSS measurement processing using any available or newly developed techniques. The model is relatively flexible in that it can be used for different types of network geometries, which consists of a square geometry as is used in previous works, as well as a front-back geometry like the one discussed in this dissertation. One of the main limitations of the simulation model is that it does not include (because it does not exist in literature) an accurate model that describes signal attenuation due to an object obstructing the communication link, according to fade level, size or type of object.

The simulation model was validated by comparing the Burr distribution approximation of the RSS histograms of the experimental data offered by Wilson et al. [2] and optimized simulated data. The simulation model was optimized by setting values of three path-loss model parameters that minimize the MSE between the simulated and reference histograms.

Chapter 6 shows the implementation of the proposed RTI system using the validated simulation model. The results of the performed simulated experiments indicate that it is possible to detect both one and two family sized cars simultaneously in the proposed RTI network setup. In subsection 6.2.3, vehicle detection performance is demonstrated to be between 95% and 100%, which is near perfect, using the new weight matrix calculation method, new node spacing setup and using two frequency channels for the link-channel selection method.

7.1 Future Work

RTI is a relatively new technology with a vast range of possibilities and opportunities that may be explored in future work. This section suggests some of the future work that may be carried out concerning the RTI system proposed in this dissertation.

One of the most significant future research that needs to be carried out is the practical implementation of the proposed roadside surveillance RTI system. This is an important research to be done to mainly investigate the technical feasibility of the proposed methodology, but also to serve as an extra reference to validate the newly developed simulation model. Following the design and methodology presented in chapter 4, it is expected that more insight will be gained into how localization accuracy is affected by vehicle velocity, as well as system performance for the tracking of multiple vehicles. Once technical feasibility has been proved for the described testing methodology, the following steps would be to create more realistic traffic scenarios, such as introducing different vehicles types, including motorcycles, as well as vehicles accelerating and decelerating inside the measurement area. The ideal future work would lead to investigating the technical feasibility of applying a roadside surveillance RTI system to public roads to determine vehicle traffic flow, which could be integrated into existing traffic monitoring systems to provide more accurate traffic estimates.

To improve the realisticness of the simulation model, a future research may be to include a more sophisticated model of signal attenuation dependent on link length, fade level and type and size of object that is located on the communication link. Such a model will need to be developed by obtaining experimental data from a practical setup.

To further enhance the simulation model, a model for RSS time variance due to random objects being placed inside the measurement area or due to weather changes may be implemented. Including RSS time variance will allow the online calibration method of Bocca et al. [3] to be included and tested.

A more advanced technique for vehicle detection may be implemented using digital image processing techniques. Such methods may employ Machine Learning, Artificial Intelligence or Reinforcement Learning,

because the proposed method of thresholding is relatively simple and may not perform as well in a practical situation as it did in the simulation model.

The proposed network setup only supports vehicle detection on one lane, so a future work would be to research the possibility of detecting vehicles on two lanes, possibly requiring to adjust the network setup.

Another future work is to research the performance of the proposed RTI system that operates in the 800/900 MHz and 5 GHz frequency bands. Such research is interesting in case the proposed RTI system may be deployed in city environments where it would otherwise interfere with other 2.4 GHz wireless networks, including public Wi-Fi hotspots.

Furthermore, to minimize the cost of a deployed RTI system, it would be interesting to investigate the minimum amount of sensors required to obtain a given system performance level. A potential customer would then be able to evaluate the trade-off between system cost and system performance and send an order accordingly.

Parameters for the simulation model were optimized manually, which most likely did not generate the best result. Therefore, it would be interesting to apply optimization techniques that search for the optimized parameter values automatically.

Other possible future works could transform the RTI network into base stations for communication with VANETs, or make the RTI network able to identify vehicles according to their size, by using the reflected signals from the vehicles to the transmitter, similar to how radar works. In the latter application, the transmitters would need to be configured to be able to receive too. This implementation may make it possible to distinguish between vehicle types, such as trucks, family cars or motorcycles. Knowing the location of the vehicles, the RTI system will also be able to determine the distance between them to generate additional traffic statistics.

7.2 Publications Related to this Dissertation

National congress

- Wilkens, J.T.; Garcia A.S, Design for Multi-Vehicle Roadside Tracking Based on Radio Tomographic Imaging; XXXIII Simpósio Brasileiro de Telecomunicações (SBrT) 2015, Juiz de Fora - MG. Anais Completo da Programação Técnica, 2015.

Bibliography

[1] Joey Wilson and Neal Patwari. Radio tomographic imaging with wireless networks. *Mobile Computing, IEEE Transactions on*, 9(5):621–632, 2010.

[2] Joey Wilson and Neal Patwari. Radio tomographic imaging data set. `http://span.ece.utah.edu/rti-data-set`, 2010.

[3] Maurizio Bocca, Ossi Kaltiokallio, and Neal Patwari. Radio tomographic imaging for ambient assisted living. In *Evaluating AAL Systems Through Competitive Benchmarking*, pages 108–130. Springer, 2013.

[4] Texas Instruments. 2.4 ghz ieee 802.15.4 / zigbee-ready rf transceiver. `http://www.ti.com/lit/ds/symlink/cc2420.pdf`, 2014.

[5] Neal Patwari and Piyush Agrawal. Effects of correlated shadowing: Connectivity, localization, and rf tomography. In *Information Processing in Sensor Networks, 2008. IPSN'08. International Conference on*, pages 82–93. IEEE, 2008.

[6] Piyush Agrawal and Neal Patwari. Correlated link shadow fading in multi-hop wireless networks. *Wireless Communications, IEEE Transactions on*, 8(8):4024–4036, 2009.

[7] NATIONAL INSTITUTE OF BIOMEDICAL IMAGING and BIOENGINEERING. Computed tomography (ct). `https://www.nibib.nih.gov/sites/default/files/CT%20Fact%20Sheet%20508.pdf`, 2013.

[8] Cesare Alippi, Maurizio Bocca, Giacomo Boracchi, Neal Patwari, and Manuel Roveri. Rti goes wild: Radio tomographic imaging for outdoor people detection and localization. *arXiv preprint arXiv:1407.8509*, 2014.

[9] Maurizio Bocca, Ossi Kaltiokallio, Neal Patwari, and Suresh Venkatasubramanian. Multiple target tracking with rf sensor networks. *Mobile Computing, IEEE Transactions on*, 13(8):1787–1800, 2014.

[10] Ossi Kaltiokallio, Maurizio Bocca, and Neal Patwari. A fade level-based spatial model for radio tomographic imaging. *Mobile Computing, IEEE Transactions on*, 13(6):1159–1172, 2014.

[11] Dustin Maas, Joey Wilson, and Neal Patwari. Toward a rapidly deployable radio tomographic imaging system for tactical operations. In *Local Computer Networks Workshops (LCN Workshops), 2013 IEEE 38th Conference on*, pages 203–210. IEEE, 2013.

[12] University of Utah. Radio tomographic imaging. `http://span.ece.utah.edu/radio-tomographic-imaging`, 3 February 2015.

[13] John Markoff. Microsoft introduces tool for avoiding traffic jams. `http://www.nytimes.com/2008/04/10/technology/10maps.html?_r=1&`, 2008.

[14] NATIONAL CABLE and TELECOMMUNICATIONS ASSOCIATION. How google tracks traffic. `https://www.ncta.com/platform/broadband-internet/how-google-tracks-traffic/`, 2013.

[15] A Pascale, M Nicoli, F Deflorio, Bruno Dalla Chiara, and U Spagnolini. Wireless sensor networks for traffic management and road safety. *IET Intelligent Transport Systems*, 6(1):67–77, 2012.

[16] Noptel Traffic Control. Traffic information. `http://www.noptel.fi/eng2/TrafficControl/index.php?doc=3_applications/5_traffic_information`, 5 February 2015.

[17] Xiling Luo, Yanxiong Wu, Yan Huang, and Jun Zhang. Vehicle flow detection in real-time airborne traffic surveillance system. *Transactions of the Institute of Measurement and Control*, page 0142331209103042, 2011.

[18] Unai Hernandez-Jayo, Aboobeker Sidhik Koyamparambil Mammu, and Idoia De-la Iglesia. Reliable communication in cooperative ad hoc networks. 2014.

[19] xandem. Introducing xandem home. `https://www.youtube.com/watch?v=dFz6Y6n-X3Y`, 2015.

[20] Christopher R Anderson, Richard K Martin, T Owens Walker, and Ryan W Thomas. Radio tomography for roadside surveillance. *Selected Topics in Signal Processing, IEEE Journal of*, 8(1):66–79, 2014.

[21] Markos Papageorgiou, Christina Diakaki, Vaya Dinopoulou, Apostolos Kotsialos, and Yibing Wang. Review of road traffic control strategies. *Proceedings of the IEEE*, 91(12):2043–2067, 2003.

[22] Yang Zhao, Neal Patwari, Jeff M Phillips, and Suresh Venkatasubramanian. Radio tomographic imaging and tracking of stationary and moving people via kernel distance. In *Proceedings of the 12th international conference on Information processing in sensor networks*, pages 229–240. ACM, 2013.

[23] Ossi Kaltiokallio, Maurizio Bocca, and Neal Patwari. Enhancing the accuracy of radio tomographic imaging using channel diversity. In *Mobile Adhoc and Sensor Systems (MASS), 2012 IEEE 9th International Conference on*, pages 254–262. IEEE, 2012.

[24] Bo Wei, Ambuj Varshney, Wen Hu, Neal Patwari, Thiemo Voigt, and Chun Tung Chou. drti: Directional radio tomographic imaging. *arXiv preprint arXiv:1402.2744*, 2014.

[25] Stephan Adler, Simon Schmitt, and Marcel Kyas. Device-free indoor localisation using radio tomography imaging in 800/900 mhz band. In *International Conference on Indoor Positioning and Indoor Navigation*, volume 27, pages 544–553. IEEE, 2014.

[26] Nehal Kassem, Ahmed E Kosba, and Moustafa Youssef. Rf-based vehicle detection and speed estimation. In *Vehicular Technology Conference (VTC Spring), 2012 IEEE 75th*, pages 1–5. IEEE, 2012.

[27] Corey D Cooke. *Attenuation field estimation using radio tomography.* PhD thesis, Virginia Polytechnic Institute and State University, 2011.

[28] Alyssa Milburn. *Algorithms and models for radio tomographic imaging.* PhD thesis, Leiden University, 2014.

[29] Yang Zhao and Neal Patwari. Robust estimators for variance-based device-free localization and tracking. 2011.

[30] Richard K Martin, Alexander Folkerts, and Tyler Heinl. Accuracy vs. resolution in radio tomography. 2014.

[31] Theodore S Rappaport et al. *Wireless communications: principles and practice*, volume 2. Prentice Hall, 2002.

[32] Braian D Ripley. Spatial statistics. 1981. *Willey, New York*, 1981.

[33] Joey Wilson, Neal Patwari, and Fernando Guevara Vasquez. Regularization methods for radio tomographic imaging. In *2009 Virginia Tech Symposium on Wireless Personal Communications*. Citeseer, 2009.

[34] Joey Wilson and Neal Patwari. A fade-level skew-laplace signal strength model for device-free localization with wireless networks. *Mobile Computing, IEEE Transactions on*, 11(6):947–958, 2012.

[35] Ossi Kaltiokallio, Maurizio Bocca, and Neal Patwari. Follow@ grandma: Long-term device-free localization for residential monitoring. In *LCN Workshops*, pages 991–998. Citeseer, 2012.

[36] UITRP Recommendation. 838-3. specific attenuation model for rain for use in prediction methods. *Intern. Telecom. Union, Geneva*, 2005.

[37] Santosh Nannuru, Yunpeng Li, Mark Coates, and Bo Yang. Multi-target device-free tracking using radio frequency tomography. In *Intelligent Sensors, Sensor Networks and Information Processing (ISSNIP), 2011 Seventh International Conference on*, pages 508–513. IEEE, 2011.

[38] Spirent Communications. Fading basics: Narrow band, wide band, and spatial channels. *Spirent*, 2011.

[39] Texas Instruments. A usb-enabled system-on-chip solution for 2.4-ghz ieee 802.15.4 and zigbee applications. `http://www.ti.com/lit/ds/symlink/cc2531.pdf`, 2010.

[40] LAN/MAN Standards Committee et al. Part 15.4: wireless medium access control (mac) and physical layer (phy) specifications for low-rate wireless personal area networks (lr-wpans). *IEEE Computer Society*, 2003.

[41] Shahin Farahani. *ZigBee wireless networks and transceivers*. newnes, 2008.

[42] National Instruments. Pulse-shape filtering in communications systems. `http://www.ni.com/white-paper/3876/en/`, 2014.

[43] MATLAB. Fading channels. `http://www.mathworks.com/help/comm/ug/fading-channels.html`, 2015.

[44] Texas Instruments. Cc253x system-on-chip solution for 2.4-ghz ieee 802.15.4 and zigbee® applications. `http://www.ni.com/white-paper/3876/en/`, 2014.

[45] Mathworks. Burr type xii distribution. `http://www.mathworks.com/help/stats/burr-type-xii-distribution.html`, 2015.

APPENDIX A – Radio Tomographic Imaging Solution Full Working

This appendix details the step-by-step procedure between equations (3.15) and (3.16) of section 3.3. Starting from equation (3.15), we have:

$$\hat{\mathbf{x}}_{MAP} = \arg\min_x \left(||\mathbf{y} - \mathbf{W}\mathbf{x}||^2 + \sigma_n^2 \mathbf{C}_x^{-1} ||\mathbf{x} - m\mathbf{1}||^2 \right) \tag{A.1}$$

$$\hat{\mathbf{x}}_{MAP} = \arg\min_x \left((\mathbf{y} - \mathbf{W}\mathbf{x})^T (\mathbf{y} - \mathbf{W}\mathbf{x}) + \sigma_n^2 \mathbf{C}_x^{-1} (\mathbf{x} - m\mathbf{1})^T (\mathbf{x} - m\mathbf{1}) \right) \tag{A.2}$$

$$\begin{aligned} \hat{\mathbf{x}}_{MAP} = \arg\min_x \Big(& \mathbf{y}^T\mathbf{y} - \mathbf{y}^T\mathbf{W}\mathbf{x} - \mathbf{x}^T\mathbf{W}^T\mathbf{y} + \mathbf{x}^T\mathbf{W}^T\mathbf{W}\mathbf{x} \\ & + \sigma_n^2 \mathbf{C}_x^{-1} (\mathbf{x}^T\mathbf{x} - \mathbf{x}^T m\mathbf{1} - m\mathbf{1}^T\mathbf{x} + m^2\mathbf{1}^T\mathbf{1}) \Big) \end{aligned} \tag{A.3}$$

To find an estimate for the RTI image $\mathbf{x}$, the argument in (A.3) needs to be minimized with respect to x. A least-squares solution is found by taking the derivative of the argument in (A.3), let us call this function $f(\mathbf{x})$, and setting the result to zero:

$$\frac{\delta f(\mathbf{x})}{\delta \mathbf{x}} = -\mathbf{y}^T\mathbf{W} - \mathbf{W}^T\mathbf{y} + \mathbf{x}^T\mathbf{W}^T\mathbf{W} + \mathbf{W}^T\mathbf{W}\mathbf{x} + \sigma_n^2 \mathbf{C}_x^{-1} (\mathbf{x} + \mathbf{x} - m\mathbf{1} - m\mathbf{1}^T) = 0 \tag{A.4}$$

$$\frac{\delta f(\mathbf{x})}{\delta \mathbf{x}} = -(\mathbf{y}^T\mathbf{W})^T - \mathbf{W}^T\mathbf{y} + (\mathbf{x}^T\mathbf{W}^T\mathbf{W})^T + \mathbf{W}^T\mathbf{W}\mathbf{x} + \sigma_n^2 \mathbf{C}_x^{-1} (\mathbf{x} + \mathbf{x} - m\mathbf{1} - (m\mathbf{1}^T)^T) = 0 \tag{A.5}$$

$$\frac{\delta f(\mathbf{x})}{\delta \mathbf{x}} = 2\mathbf{W}^T\mathbf{W}\mathbf{x} - 2\mathbf{W}^T\mathbf{y} + \sigma_n^2 \mathbf{C}_x^{-1} (2\mathbf{x} - 2m\mathbf{1}) = 0 \tag{A.6}$$

$$\frac{\delta f(\mathbf{x})}{\delta \mathbf{x}} = 2(\mathbf{W}^T\mathbf{W} + \sigma_n^2 \mathbf{C}_x^{-1})\mathbf{x} - 2\mathbf{W}^T\mathbf{y} - 2m\sigma_n^2 \mathbf{C}_x^{-1}\mathbf{1} = 0 \tag{A.7}$$

Solving for $\mathbf{x}$ gives the solution in (3.16):

$$2(\mathbf{W}^T\mathbf{W} + \sigma_n^2 \mathbf{C}_x^{-1})\mathbf{x} = 2(\mathbf{W}^T\mathbf{y} + m\sigma_n^2 \mathbf{C}_x^{-1}\mathbf{1}) \tag{A.8}$$

$$\mathbf{x} = (\mathbf{W}^T\mathbf{W} + \sigma_n^2 \mathbf{C}_x^{-1})^{-1} (\mathbf{W}^T\mathbf{y} + m\sigma_n^2 \mathbf{C}_x^{-1}\mathbf{1}) \tag{A.9}$$

APPENDIX B – Initialization of Simulation Model

The initialization of the simulation model consists of setting the node and voxel locations and calculating the weight and regularization matrices.

Node locations are dependent on the chosen network geometry. Currently, the simulation model supports a square and front-back geometry, where a square network geometry contains nodes on all four sides of a square-shaped network and a front-back network contains nodes only on two sides of a rectangular-shaped network. The input of the function that returns node locations consists of the network geometry type (square or front-back), the number of nodes in the network and the spacing between nodes along and across the network. The network of Wilson et al. [1] is a square network that contains 28 nodes with a node spacing of 3 ft. as shown in Figure (1). The node location matrix that is returned contains x- and y-coordinates in the first and second columns respectively, where the row number refers to the node number (or ID).

The initialization procedure also obtains a vector that assigns a link number to each two communicating radios. This vector and the node location matrix are used to calculate a link length vector containing the distances between the nodes.

The function that returns voxel locations needs to know voxel size, number of network nodes and the spacing between nodes along and across the network. The network of Wilson et al. [1] contains 42 x 42 voxels, which corresponds to a voxel width of 0.5 ft. The matrix that it returns contains four columns: the first and second columns refer to voxel number in the x- and y-coordinates respectively, whereas the third and fourth columns contain the geographical location of the voxels in the x- and y-directions respectively. The row number refers to the specific voxel number.

The weight matrix as described in subsection 3.2.2, which relates the importance of a link to a particular voxel, needs to know all the previously computed vectors and matrices, as well as the ellipse width parameter λ. This parameter is typically set to relatively low. Wilson et al. [1] set $\lambda = 0.01$ ft.

The regularization matrix used for the simulation model depends on whether the user wants a more generalized or more specific result. For a more generalized solution, Tikhonov regularization as in (3.20) is used, whereas for a more specific result that requires empirically determined parameters, regularization with a covariance matrix is employed as in (3.19). In Tikhonov regularization, the regularization matrix requires the previously calculated weight matrix, the Tikhonov matrix and a regularization parameter α, which is set to $\alpha = 5$ by Wilson et al. [1]. Wilson et al. demonstrate the effect of smooothing parameter on localization error [1]. To obtain the Tikhonov matrix, only the number of voxels is needed for the simulation algorithm to return the $\mathbf{D}_X$ and $\mathbf{D}_Y$ matrices, which are shown as an example by Cooke [27]. Regularization with the covariance matrix as in (3.19) requires the knowledge of voxel locations to calculate Euclidian distance between voxels, regularization parameter (or noise variance) σ_n^2, voxel intensity variance σ_x^2 and voxels' correlation parameter δ_c. Researchers that used the covariance matrix did not explicitly detail how they determined the parameters, so it is assumed they were found empirically. Alippi et al. [8] sets the following parameters: $\sigma_n^2 = 0.1$, $\sigma_x^2 = 0.001$ and $\delta_c = 1$.

APPENDIX C – Results Continued

This appendix describes the effect of regularization and removal of negative observations on system performance, serving as a continuation of the results described in chapter 6.

C.1 Effect of regularization

Regularization has been described as being general or specific, where the former uses a Tikhonov matrix and the latter a Covariance matrix. General regularization only requires one parameter and is therefore a simpler method, whereas specific regularization needs three parameter to be optimized, but can be adjusted to be more specific.

Figure 36 illustrates vehicle detection performance of both methods, which was calculated using the same procedure as outlined in subsection 6.2.1. Table 3 lists the parameters used for the performance evaluation, which were optimized manually, meaning they may not be the true best values since manual optimization is a cumbersome task.

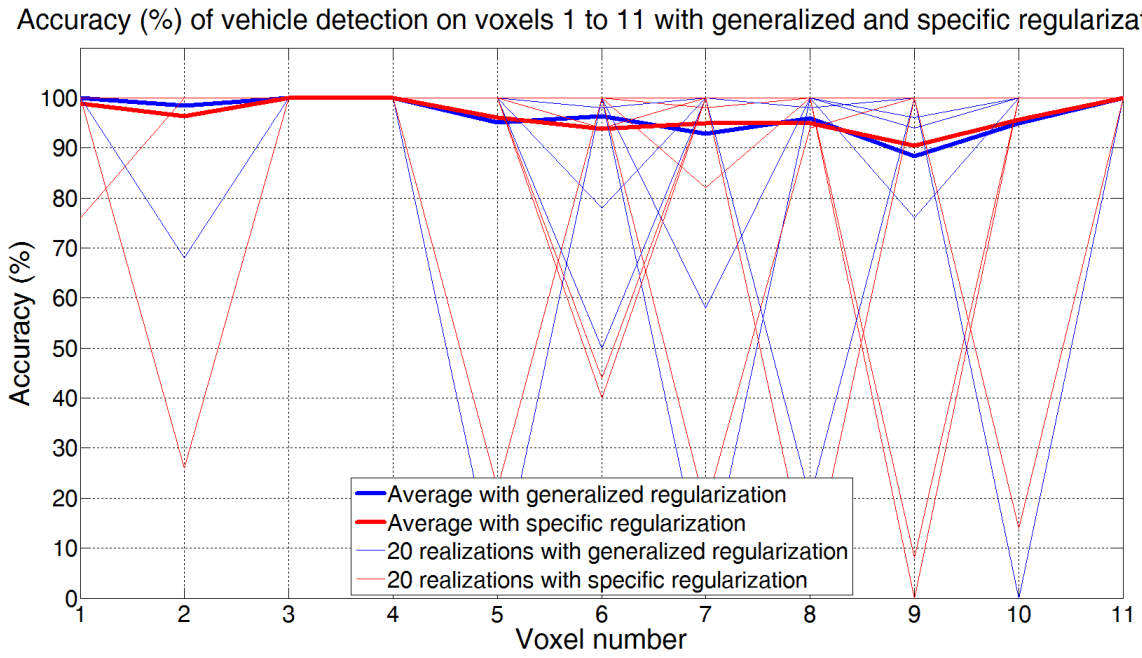

Figure 36 – Accuracy (%) of vehicle detection on voxels 1 to 11 with generalized and specific regularization. The data presented are 20 realizations of the generalized and specific regularization and their average.

As can be observed, there is no notable difference in performance between generalized or specific regularization. They both achieve a vehicle detection accuracy of between 90% and 100% and perform similarly in each voxel. Because the generalized regularization is simpler as it requires only one parameter to be optimized, it is chosen as the generalization method for the optimized result.

Table 3 – Parameters and their corresponding values and description used for the comparing regularization type.

Parameter	Value	Description
α	0.1	Generalized regularization parameter
σ_x^2	0.1	Voxels' intensity variance [dBm]
δ_c	3	Voxels' correlation parameter
σ_n^2	0.1	Noise variance [dBm]

Figure 37 shows the difference between generalized and specific regularization as an RTI image and line plot for a vehicle located on voxels 8 and 9. The RTI image with generalized regularization shows to be cleaner than specific regularization, because neighboring voxels have lower intensity values.

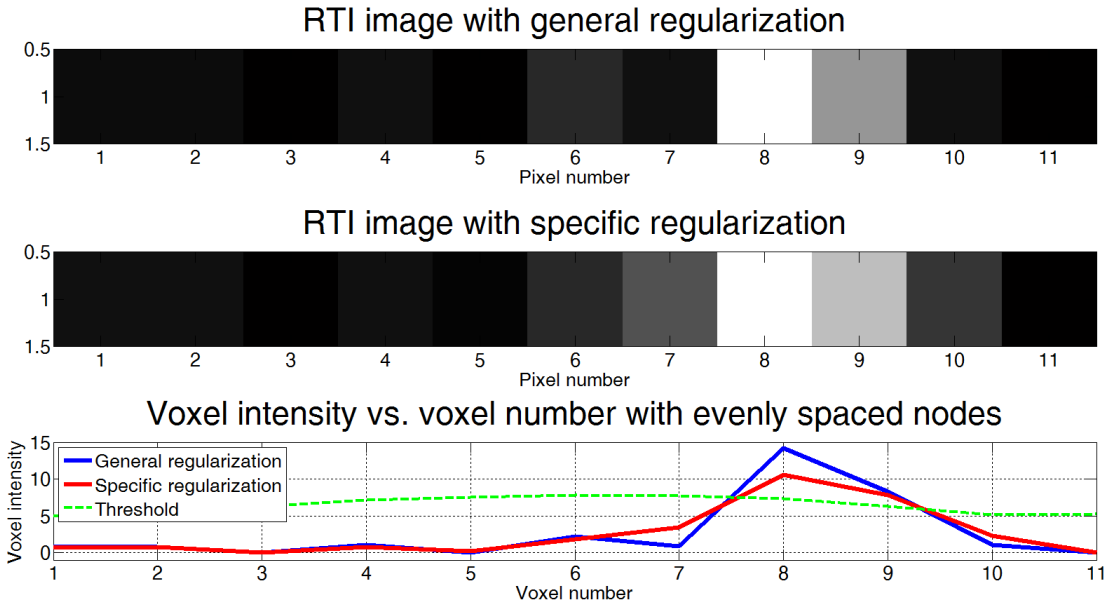

Figure 37 – RTI image with vehicle located on voxels 8 and 9 and corresponding line plot with generalized and specific regularization. The dashed curves are the thresholds with their color corresponding to the RTI image they represent.

C.2 Effect of removing negative observations

Removing negative observations from the RTI image has been shown by Anderson et al. [20] to improve system performance in their specific RTI system. Figure 38 compares vehicle detection accuracy without and with negative element removal (NER). As can be observed, for the proposed RTI system, there is zero difference in system performance.

Figure 39 shows the RTI image and corresponding line plot of the result with and without negative element removal. The NER RTI image solution obtains a cleaner image with less noise around the vehicle. Therefore, it was chosen to employ the NER method for the optimized result.

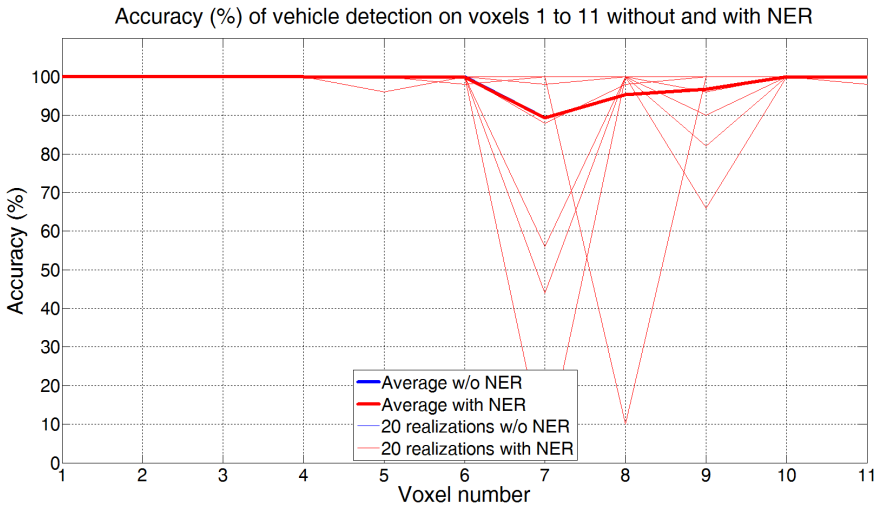

Figure 38 – Accuracy (%) of vehicle detection on voxels 1 to 11 without and with negative element removal (NER). The data presented are 20 realizations of without and with negative element removal (NER) and their average.

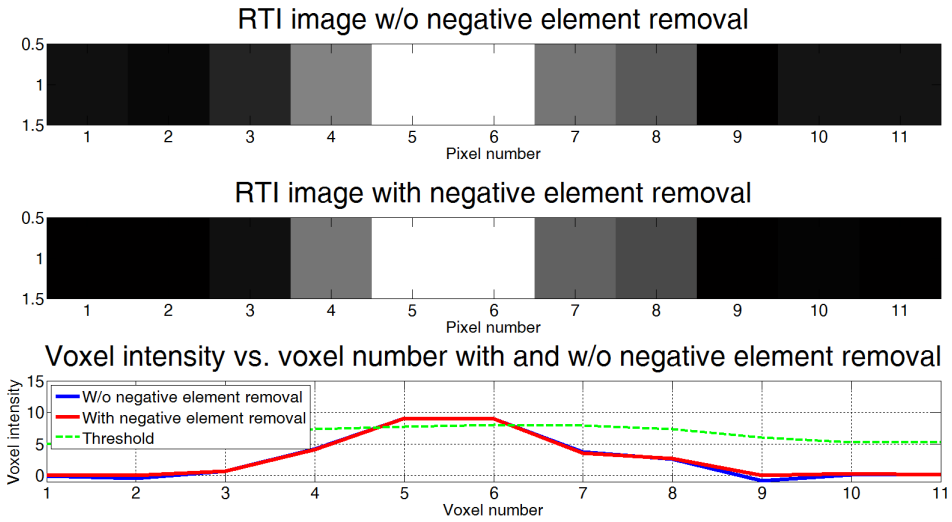

Figure 39 – RTI image with vehicle located on voxels 5 and 6 and corresponding line plot without and with negative element removal (NER). The dashed curves are the thresholds with their color corresponding to the RTI image they represent.